NASA Contractor Report 3948

Computer Simulation of a Wind Tunnel Test Section With Discrete Finite-Length Wall Slots

William B. Kemp, Jr.

COOPERATIVE AGREEMENT NCC1-69
APRIL 1986

NASA Contractor Report 3948

Computer Simulation of a Wind Tunnel Test Section With Discrete Finite-Length Wall Slots

William B. Kemp, Jr.
The College of William and Mary
Williamsburg, Virginia

Prepared for
Langley Research Center
under Cooperative Agreement NCC1-69

National Aeronautics
and Space Administration

**Scientific and Technical
Information Branch**

1986

TABLE OF CONTENTS

SUMMARY

A computer simulation of a slotted wind tunnel test section which includes a discrete, finite-length wall slot representation with plenum chamber constraints and accounts for the nonlinear effects of the dynamic pressure of the slot outflow jet and of the low energy of slot inflow air has been developed. The simulation features were selected to be those appropriate for the intended subsequent use of the simulation in a wall interference assessment procedure using sparsely located wall pressure measurements. Simulation results demonstrate that accounting for slot discreteness is important in interpreting wall pressure measured between slots, and that accounting for nonlinear slot flow effects produces significant changes in tunnel-induced velocity distributions and, in particular, produces a longitudinal component of tunnel-induced velocity due to model lift. A characteristic mode of tunnel flow interaction with constraints imposed by the plenum chamber and diffuser entrance is apparent in simulation results and is derived analytically through a simplified analysis.

INTRODUCTION

The development of methods which make use of measured wall pressures in the assessment of and correction for wall interference in wind tunnel tests has been the subject of a significant amount of recent effort (ref. 1). Such methods for application to two-dimensional airfoil tests have reached a relatively mature state (ref. 2) and data handling procedures for production use have been developed (ref. 3). The excellent survey of ref. 4 clarifies the role of such methods within the broad scope of theoretical approaches to the problem of two-dimensional wind tunnel wall interference. For three-dimensional applications, however, satisfactory interference assessment methods are not yet available. One reason is that a very large amount of experimental data is required to define the boundary surface distributions needed for three-dimensional assessment computations. In ref. 5, Mokry simplified this problem by representing the test model as a point disturbance and using an azimuthal harmonic description of the outer boundary. Wall pressures measured in four longitudinal rows were used to define the lowest order harmonics, and higher harmonics were ignored. Rizk, et al (refs. 6 and 7) used a more realistic representation of the test model based on the known model geometry and measured forces and moments but assumed that the measured data available were sufficient to define fully an outer computational boundary near the tunnel walls.

The results to be described in this paper were obtained in a study undertaken to develop a new outer boundary treatment which offers the promise of a high level of accuracy while requiring measurement of wall pressures at a practical number of points. In concept, the outer computational boundary is provided by a numerical model of the tunnel test section capable of simulating geometric details having a small size relative to the characteristic tunnel dimensions, and formulated in terms of boundary condition parameters which can

be controlled to reproduce the pressure distributions measured along several longitudinal rows in the tunnel. For this purpose the numerical model should provide a realistic representation of all test section features capable of affecting significantly the pressure at the measurement locations. A numerical test section model has been developed in an attempt to satisfy this requirement. It is applicable to test sections having open (unbaffled) wall slots and is limited at present to subcritical wall flows. In keeping with the practice developed for two-dimensional interference assessment, viscosity effects at the wall are not modeled overtly but are assumed to be accounted for by adjusting the parameters of inviscid form boundary conditions as necessary to match measured pressures. Confidence in the validity of this approach is strengthened by the results of Sedin and Sorensen (ref. 8) which show that, for the axisymmetric case studied, adjustment of such parameters in a theoretical inviscid slot boundary condition yielded good agreement with measured model pressures at the tunnel center line.

The numerical model has been developed within the context of a wind tunnel flow simulator, that is, all boundary conditions are specified without recourse to data measured in an actual tunnel. The simulation is a system of linear equations largely based on high order panel method technology as implemented by Thomas (ref. 9). Slotted wind tunnel walls are represented either as equivalent homogeneous walls or with discrete slots and are of finite length with recognition of the flow constraint imposed by a plenum chamber. The discrete slot simulation includes the nonlinear effects arising from the dynamic pressure in the outflow jets issuing from the slots into the plenum and from the low energy of inflow air from the plenum. A computationally efficient algorithm is used for iterative update of the solution when the nonlinear features are included. Some results from use of the simulation are presented in ref. 10 and a user's guide to the computer program which performs the simulation is provided by ref. 11.

The present paper presents a comprehensive description of each feature of the simulation along with simulation results to illustrate the characteristics of the feature and, where possible, to compare the simulation results with known criteria or to compare alternative formulations. In the case of linear simulation of discrete slots, the crossflow characteristics are examined in detail and are related to the theoretical slot flow models of refs. 12 and 13. Results from the complete simulation are compared with wall pressures measured in two different experiments. Finally, a characteristic mode of interaction between the tunnel flow and plenum constraints, observable only with finite length slots, is derived from simplified first principles to clarify a pattern of tunnel pressure distributions apparent in many of the simulation results.

SYMBOLS

a	slot width
C	cross section area of test section
C_D	drag coefficient
C_L	lift coefficient
C_p	pressure coefficient
c	reentry flap chord, also local wing chord
c_1, c_2	constants of integration
d	slot spacing
F_r	attenuation factor, defined by eqn. (13)
f	fraction of reentry flap chord
h	tunnel half height
K	dimensionless coefficient in equivalent homogeneous slotted wall boundary condition
$\tilde{K}$	coefficient in discrete slot boundary condition
$\Delta K'$	increment in $\tilde{K}$ due to distance from slot
M	Mach number
n	number of slots
P	slotted wall parameter, $1/(1+Kd/h)$
R	coefficient in porous wall boundary condition
r	radial distance from source line representing slot
r_b	radius of slot inflow bubble
S	line source strength, also test model reference area
U_∞	far field reference velocity, represented herein as unity
u,v,w	velocity perturbations in x, y, and z directions respectively normalized by tunnel far field velocity
u_f	reentry flap boundary condition parameter

V	test model volume
x,y,z	cartesian coordinates
Δ	prefix denoting increment
β	$\sqrt{1 - M^2}$
δ	lift interference parameter at model location, $\Delta_I w^L$
ε	slot control point recession distance
θ	body azimuth angle
λ	slotted tunnel characteristic langth, defined by eqn. (20)
σ	panel source sheet strength
ϕ	perturbation potential
ϕ	perturbation potential outside the boundary of tunnel flow domain

Subscripts

d	pertaining to slot discretizing perturbation
h	pertaining to equivalent homogeneous slotted wall
I	arising from tunnel interference
n	normal to wall
o	condition at slot origin
p	plenum chamber condition
r	condition at distance r from line source
ε	condition at distance ε from line source

Superscripts

D	point doublet model disturbance, results have been multiplied by $\beta^3 h^3/V$
S	point source model disturbance, results have been multiplied by $\beta^2 C/C_D S$
L	point lift model disturbance, results have been multiplied by $C/C_L S$

DESCRIPTION AND EVALUATION OF SIMULATION

General Panel Method

The computer program which performs the wind-tunnel flow simulation was developed by starting with a general purpose panel method program for solving subsonic aerodynamic flow problems and adding those features required to solve the slotted test section flow problem. The panel method program selected for this purpose is a vectorized program written at NASA Langley Research Center by J. L. Thomas for use in the panel method technology study reported in ref. 9. The program provides for multiple networks of panels. Within any network the singularity distribution over each panel may be specified as a null, constant, or bilinear source distribution and a null, constant, bilinear, or biquadratic doublet distribution. For the higher order distributions, continuity of the singularity strength across panel edges within a network is enforced in a least square sense. Boundary conditions are imposed at control points which are located, in general, at the panel centers. Additional control points are provided at the corners and edges of biquadratic doublet networks to allow achievement of a high degree of doublet strength continuity across edges of abutting networks.

The program provides a flexible tool for applying panel method technology at a level comparable to those methods described in more detail in refs. 14 and 15 to obtain incompressible aerodynamic flow solutions to problems with steady state Neumann boundary conditions. Both a direct and an indirect method of imposing the Neumann condition are provided. The direct method requires the solution to satisfy the prescribed velocity component normal to the panel v_n at control points. In the indirect method, the panel source strength is set a priori to the specified normal velocity less the normal component of the far field (reference) velocity; and the solution is required to produce zero perturbation potential in the flow behind the panels ($\phi = 0$) at the control point locations. Even with direct application of the Neumann boundary condition, the panel source strengths may be prescribed as in the indirect method so that the flow behind the panels remains essentially unperturbed. Previous experience with panel methods (c.f. refs. 14 and 15) has shown that although the indirect form need not satisfy the prescribed Neumann condition exactly at control points, it generally produces a more accurate overall solution than the direct form.

During the present study, the basic panel method procedure was modified to account for subsonic compressibility by means of the Goethert rule and to calculate pressure coefficients from the local velocity magnitude by use of the exact compressible relationship. The procedure for storing and handling the panel aerodynamic influence coefficients was modified as described in Appendix A to reduce computational resource requirements.

Fundamentals of the Test Section Simulation

The slotted test section simulation is an aerodynamic flow prediction problem to be solved using panel method technology. The problem can be characterized in terms of the boundary geometry of the computational domain,

the type and order of known and unknown singularity distributions on the boundary, the form and location of boundary conditions, and the form of singularities used to represent sources of flow disturbance. Many of these characterizing elements could be chosen from the options available in the general panel method already described. Provisions to accept other elements were developed and incorporated into the panel method program in the course of the present study. Notable examples of the newly developed features include the singularities and boundary conditions used in the slotted-wall regions of the tunnel and the prescribed singularities used to represent the wind-tunnel test model and its support sting and sting support sector.

A baseline characterization of the test section simulation is illustrated in fig. 1. Most of the results presented herein to illustrate the program development were obtained using the baseline problem characterization except for specifically noted departures. The baseline wind-tunnel test section is presumed to have a square cross section with half-height h and have solid side walls and six slots in each of the top and bottom walls with openness ratio a/d of 0.06. Only one half of the tunnel is modeled; the other half is represented by symmetric reflection across the x,z plane of symmetry. The solution domain is the interior of a rectangular parallelepiped having a cross section identical to that of the test section throat.

The top, side and bottom boundaries are each paneled with a network of biquadric doublet panels with unknown strength and a boundary condition requiring $\overline{\phi} = 0$ at control points. For this interior flow problem, $\overline{\phi}$ is the perturbation potential in the exterior flow and a basic aim of the simulation is to keep the exterior flow essentially unperturbed so that the normal velocity at the interior flow boundary is equal to the local source panel strength. Thus, an a priori specification of source panel strength (or the absence of source panels) completes the imposition of a Neumann boundary condition on the interior flow by the indirect method of the general panel program. At control points lying on network edges at the plane of symmetry, a special condition is imposed requiring that the panel doublet gradient be continuous across the plane of symmetry. In the slotted wall regions of the test section, the boundary condition on the interior flow is not a Neumann condition; therefore, the source strength is considered to be unknown and is solved simultaneously with the doublet strengths to satisfy the boundary conditions on both the interior and exterior flows. The source distributions and boundary conditions for both homogeneous wall and discrete slot simulations of the slotted wall are developed in the following section. The source lines shown on fig. 1 are used in the discrete slot simulation.

The cross section of the upper right hand tunnel quadrant shown in fig. 1b illustrates the location of panel boundaries as well as the line sources at slot locations in the discrete slot simulation. In the longitudinal direction, panel lengths varied from a minimum of $0.3h$ near $x = 0$ to a maximum of about $4h$ at the ends of the tunnel domain.

The downstream end of the tunnel flow domain is closed by a combined source and doublet constant strength panel. A boundary condition requiring $\overline{\phi} = 0$ is imposed at the panel center thus allowing the closing doublet panel to absorb whatever perturbation potential has developed in the interior flow.

The source strength is also considered unknown and is linked by a special provision in the simulation program to a free control point for which both the location and boundary condition are selected by the user. In the baseline simulation, this free point is used to impose the $\bar{\Phi} = 0$ condition at the upstream end of the interior domain where the absence of a doublet panel results in continuity of potential between the exterior and interior domains.

The unperturbed flow has by definition a velocity of unit magnitude in the positive x direction. The axial velocity entering the interior flow, therefore, would be essentially unity if the entrance is located far from any perturbing influences. In the baseline simulation, more positive control of the entering axial velocity is achieved by using a source panel at the upstream end with a direct Neumann boundary condition at the panel center. Alternatively, the free control point feature can be used with the upstream source panel to specify the axial velocity at some other reference location in the interior flow.

The wind tunnel test model is represented in the baseline simulation by any of the three elemental singularities which have become traditional for basic studies of wall interference, the point doublet, point source, and point lifting system (semi-infinite line doublet) to yield solid blockage, wake blockage and lift interference, respectively. The point singularities are generally located on the tunnel axis at $x = 0$. The simulation program also provides for much more realistic representation of a wing-body-tail test model and its support system which are discussed in a subsequent section of the paper. In the simulation program output, the flow properties given at a point include the potential and velocity component perturbations due to tunnel interference as well as the total velocity components and total perturbation potential. For this purpose, the interference perturbation is defined as the summation of perturbations from all singularities except those representing the test model. These results are calculated not only at all panel centers and slot control points but also at points along arbitrarily located survey lines. All results presented herein of simulations using point disturbance representations of the test model are given in the normalized form defined for the superscripts D, S and L.

Simulation results for the simple case of a square solid wall tunnel with each of the three point singularity model representations are shown in fig. 2 for both the direct ($v_n = 0$) and indirect ($\bar{\Phi} = 0$) forms of the Neumann boundary condition. Data at control points are shown by point symbols and data along survey rows are shown by line symbols in straight line segments connecting the individual points in the survey row. The longitudinal spacing of survey points is a uniform distance of 0.25h.

The longitudinal velocity distribution at or near the top wall center line is shown in Fig. 2a and the wall interference velocity distribution on the tunnel axis is shown in fig. 2b. The two forms of the solid wall boundary condition yield somewhat different results. Values of interference velocity at the point model location $x = 0$ are compared with theoretical predictions from the formulations of ref. 16 in the following table.

Point Model	Wall boundary condition $v_n = 0$	$\overline{\phi} = 0$	Theory
Doublet	.0851	.0893	.0896
Source	.2444	.2499	.2500
Lift	.1361	.1367	.1368

The interference velocities obtained with the $\overline{\phi} = 0$ boundary condition show excellent agreement with theoretical values while some significant discrepancies result from use of the $v_n = 0$ condition.

The added mass flow from the point source disturbance should result in a normalized axial velocity perturbation far downstream equal to 0.5. The top wall velocities shown on fig. 2a for the point source reached values of .4889 and .4998 for the $v_n = 0$ and $\overline{\phi} = 0$ boundary conditions respectively. Thus, for the $v_n = 0$ condition, 2.2 percent of the added mass "leaked" out through the walls in the vicinity of the point disturbance. The $\overline{\phi} = 0$ condition reduced the leakage to 0.04 percent.

The nature of this leakage is illustrated in fig. 2c which shows the longitudinal distribution of the normal velocity component on the side wall at or near $z = 0$. Considering first the $v_n = 0$ boundary condition, the normal velocity is shown to be exactly zero at the panel center control points. The survey line at $z = 0.1h$, which passes through the control points, shows some non-zero values between panel centers but the survey resolution is not fine enough to define the shape of the distribution over each panel. The survey at $z = 0$, however, coincides with a line of panel boundaries as shown on fig. 1b. The normal velocities shown at $z = 0$ for the doublet and source disturbances are in general in the same direction as the wall-normal component of the disturbance-induced velocity, indicating an overall incomplete cancellation of normal velocity by the simulated solid wall. With the $\overline{\phi} = 0$ boundary condition, the normal velocity at control points is no longer zero, in general, but is displaced so as to compensate for the nonuniformity over the panels. Thus it may be stated that the $v_n = 0$ condition causes the local surface streamline to be tangent to the boundary at each control point, but the $\overline{\phi} = 0$ condition acts essentially as though the bounding stream surface passes through all control points.

The top wall normal velocity distributions given on fig. 2d show that the normal velocities at control points are distributed similarly to those on the sidewall but the survey along panel boundaries at $y = 0$ shows a distribution which is more like the sidewall survey through control points than like that on the $z = 0$ panel boundaries. This is because the $y = 0$ plane is treated in the simulation program as a plane of symmetry and the special boundary condition imposed at the network edge control points at $y = 0$, together with symmetry considerations, enforce doublet gradient (vorticity) continuity across the plane of symmetry. As a result, each panel intersecting the plane of symmetry behaves as half of a larger panel bisected by the plane of symmetry and the flow anomolies which can occur at typical panel boundaries

are suppressed at $y = 0$. This feature is of particular value in the discrete slot simulation to be discussed in the next section.

Linear Slotted Wall Simulation

Singularities and Boundary Conditions.- The flow near a wall with discrete slots is simulated by a procedure which makes use of two concepts used by Berndt in ref. 17. The first is the use of the perturbation field from a line source singularity as the outer expansion of a discrete slot perturbation, valid where the slot width is small relative to distance from the slot. The second is the formulation of discrete slot effects in a slender body context whereby the three-dimensional flow solution with slotted walls is formulated as a three-dimensional solution satisfying a homogeneous wall boundary condition, plus the difference between two two-dimensional crossflow potentials, both of which satisfy the crossflow properties far from the wall of the homogeneous-wall 3D flow, and each of which satisfies crossflow properties at the wall appropriate to the discrete slot or homogeneous wall conditions respectively. By this means, the discrete slot simulation can benefit from any refinements in the homogeneous slotted wall condition which result from slotted wall research.

Consider first the homogeneous wall solution. The linearized homogeneous slotted wall boundary condition may be written

$$u - u_p + Kd\frac{\partial v_n}{\partial x} = 0 \tag{1}$$

where v_n is the outward normal velocity. This wall is modeled by superimposing a network of bilinear source panels over the doublet panels in the slotted wall region and imposing the homogeneous wall condition at the panel centers. Because the basic $\overline{\Phi} = 0$ condition is also imposed at these points, the substitution $v_n = -\sigma_h$ is valid and both the source and doublet panel strengths are treated as unknowns to be determined during the solution. With this substitution, eqn (1) is integrated assuming a constant u_p to obtain

$$\phi - \phi_o - u_p(x-x_o) - Kd\sigma_h = 0 \tag{2}$$

which is the boundary condition actually used in the homogeneous wall simulation. Special constraints on the bilinear source distribution for the homogeneous wall simulation are discussed in Appendix B.

The model of the discretely slotted wall is developed using the homogeneous wall as a starting point, and superposing additional singularities on the slotted wall boundary to collect the wall flux into discrete lines. The discretizing singularity is defined as a source distribution so that its influence on the interior flow wall flux is local and directly quantifiable. No attempt is made to suppress the corresponding influence on the computationally defined exterior flow. Instead, the unperturbed exterior flow

corresponding to the homogeneous wall solution is retained as an identifiable part of the total solution by explicitly excluding the influence of the discretizing singularities from the exterior flow potential constrained by the $\overline{\Phi} = 0$ boundary condition. The discretizing singularity, therefore, is quantified as the combination of a source sheet of strength

$$\sigma_d = 2v_n \tag{3}$$

to cancel the smoothly distributed wall flux in the homogeneous wall interior flow and a set of source (or sink) lines at the slot locations of strength

$$S = -\int_{-d/2}^{d/2} \sigma_d dy \tag{4}$$

to replace the distributed wall flux with a concentrated flux of the same magnitude. In any crossflow plane, the perturbation in the interior flow induced by the discretizing singularities on the boundary is equivalent to the difference between the two crossflow potentials used in the slender body representation of the discrete slots. The discretizing singularities directly produce the required flow difference at the outer boundary and eqn (4) promotes the rapid decay of the discretizing perturbation with distance from the wall by ensuring that the net source strength is zero in boundary segments the size of the slot spacing.

To implement this concept in the numerical model, the line sources as well as the longitudinal edges of the source and doublet panels are placed at the slot locations. The line source strength S is quantified at the panel corners, varies linearly on the intervening segments, and has a value of zero at the upstream and downstream ends of each slot. The total source strength on the panels is obtained by combining the homogeneous wall and discretizing sheet strengths, and its value at each panel edge midpoint adjacent to a slot is linked to the local value of S so as to assure that eqn (4) is satisfied. Details of the discrete slot source network are described more fully in Appendix B and calculation of the aerodynamic influence of the line source elements is described in Appendix C.

The relations given previously may be combined to specify the total source sheet strength σ in terms of S as

$$\sigma = \sigma_h + \sigma_d = \frac{1}{2}\sigma_d = -\frac{S}{2d} \tag{5}$$

Using eqns. (2), (3) and (5) the discrete slot boundary condition is written

$$\phi - \phi_o - u_p(x-x_o) - \frac{1}{2}\hat{K}S = 0 \tag{6}$$

which is enforced as a boundary condition at slot control points located nominally at the line source quantifying points (at panel corners) but recessed a small distance ε into the interior flow from the line sources

representing the slots. This recession distance can be related approximately to the slot width by assuming that the radial velocity across a semicircle of radius ε centered on the line source should be equal to the transverse velocity through a slot of width a in the wall being modeled. Accordingly,

$$\varepsilon = a/\pi \tag{7}$$

The panel doublet strengths and line source strengths are both treated as unknowns constrained by boundary conditions at the panel centers and slot control points.

Evaluation of the Linear Discrete Slot Simulation.- To examine the crossflow properties of this discrete slot representation, the simulation program was used to solve the flow in a long duct with full length discrete slots on the top wall and an upward transpiration introduced over the entire bottom wall by means of a uniform strength source sheet. The solution showed that at a sufficient distance from the upstream end, an equilibrium condition was reached in which the flux absorbed by the line sinks on the top wall just matched that introduced uniformly over the bottom wall and all longitudinal velocity gradients vanished. The equilibrium level of the longitudinal perturbation velocity was set to zero by appropriate control of the source panel strength at the upstream end of the duct. The resulting flow in the equilibrium region is a two dimensional flow in the duct cross section planes.

From this solution, the potential distributions along two vertical lines were determined and are shown in a normalized form in fig. 3a. The distribution labeled $y = 0$ is aligned with one of the top wall slots and shows the increasing vertical gradient of potential as the sink line is approached. The distribution at $y = \pm.5d$ shows the potential gradient vanishing at the stagnation point halfway between slots. At a distance from the wall of less than one slot spacing the two distributions have become essentially coincident with a gradient of unity. The distribution corresponding to an equivalent homogeneous wall representation is obtained by extrapolating this interior flow to the wall with a constant gradient. The homogeneous slot parameter K is found, by rearranging eqn. (2), to represent the jump in potential (normalized relative to $v_n d$) between the boundary value in the tunnel flow and a reference value in the plenum and is so indicated on Fig. 3a.

For the discrete slot representation, the normalized potential curve at $y = \pm.5d$ reaches the wall with a vanishing normal gradient indicating stagnation of the transverse flow halfway between slots. The potential value at this point differed from the homogeneous wall boundary value by about .22 which agrees with the incremental value derived by Berndt and Sorensen (ref. 13).

The normalized potential curve labeled $y = 0$ on Fig. 3a can be interpreted as the locus of combinations of ε and $\tilde{K}$ required to produce the same flow in the tunnel far from the wall as the homogeneous wall model, if K and $\tilde{K}$ are measured from the same plenum reference value. It is clear

that with the discrete slot model, the acceleration of tunnel interior flow toward the slot provides in the discrete slot solution some of the potential growth which must be supplied entirely by the boundary condition in the homogeneous wall model. This discretization increment in normalized potential is shown in Fig. 3b as a function of slot openness ratio a/d by using the simple assumption of eqn. (7) to relate a to ε. Fig. 3b shows that this variation is a close approximation to the classical log cosecant form of the homogeneous wall slot parameter K as given by Davis and Moore (ref. 21). This result suggests that instead of eqn. (7), an improved relationship between a and ε should be sought such that the data of fig. 3a can be interpreted under the assumption that

$$K - \tilde{K} = \frac{1}{\pi} \ell n \csc\left(\frac{\pi}{2}\frac{a}{d}\right) - \frac{\varepsilon}{d} \tag{8}$$

so that the boundary condition parameter $\tilde{K}$ supplies just those streamline curvature effects which occur within the slot and in any extension of the slot flow into the plenum chamber while those occurring in the tunnel interior flow are explicitly modeled by the simulation solution. It was found that the function

$$\frac{d}{\varepsilon} = 4.072\frac{d}{a} - 2.859 \tag{9}$$

satisfies this requirement almost exactly for values of a/d between 0 and 0.3 with a gradually increasing discrepancy for more open slots.

The Barnwell slot parameter correlation reported in ref. 18 gives a homogeneous wall slot parameter $K = 3$ for the value of $a/d = .06$ assumed for the baseline simulation of this paper. From eqn (8), the discrete slot effects in the tunnel interior should account for an increment of .752 leaving $\tilde{K} = 2.248$ to be used in the discrete slot boundary condition, eqn (6). The slot control points are located by eqn (9) at $\varepsilon/d = .01538$ or $\varepsilon/h = .005128$ for the baseline slot spacing $d = h/3$.

To illustrate some basic properties of the discrete slot representation, the baseline simulation with each point disturbance model was run with the top and bottom walls slotted for the entire length of the tunnel domain to approximate the infinite length slotted test section for which wall interference predictions exist in the literature (c.f. ref. 16). The equivalent homogeneous wall simulation with $K = 3$ were run for comparison. The resulting distributions at the walls of the w, v, and u velocity components are shown in figs. 4, 5, and 6 respectively, and the interference velocity distributions on the tunnel axis are given in fig. 7.

In fig. 4a, the longitudinal distributions of vertical velocity at and near the top wall center line are shown. Figs. 4b and 4c show selected cross plots at constant longitudinal locations of the vertical velocity distribution across the top wall from $y = 0$ to the corner at $y = z = h$ and down the side wall to $z = 0$. In the discrete slot cases, the circle symbol local line source strength converted to an equivalent homogeneous normal velocity, $-S/2d$. These values are seen to be in excellent agreement with the

distributions shown for the homogeneous wall simulations. At y locations between slots, the discrete slot results closely approximate the desired solid wall condition of zero vertical velocity. In fact, the results shown on fig. 4a at the discrete slot panel centers are so similar to those given in fig. 2d for the solid wall tunnel (which were intentionally plotted at the same scale) that a zero leakage condition over the panels between slots is implied.

It should be noted that, with one exception to be stated later, the results indicated as survey results at the wall were actually obtained from rows of points spaced into the tunnel a distance of $hx10^{-5}$ from the wall panels. In longitudinal surveys at the wall, such as the $y = 0$ surveys in fig. 4a, only those survey points at $x/2\beta h = 1.625$ coincided with the longitudinal locations of panel boundaries. The normal velocity anomolies shown at these points probably are very localized and result from doublet gradient discontinuities across the local panel boundaries.

The vertical velocity distributions in the vicinity of the tunnel corner shown in figs. 4b and 4c are reasonably smooth in the homogeneous wall simulation. In the discrete slot simulations, the wall survey points were very closely spaced in the vicinity of the corner. The behavior of vertical velocity near the corner is reasonably realistic. The top wall survey shows essentially zero vertical velocity for all points out to and including the next to last point at $y = .994h$. Only the last point, at $y = .99999h$ shows an unrealistically high vertical velocity. The behavior of the lateral velocity component in close proximity to the corner, however, is far from realistic in the discrete slot simulation. Fig. 5 shows distributions of lateral velocity across the top wall and down the sidewall for a case typical of those with large outflow through the top wall slots. The distribution from the discrete slot simulation shows the expected variation between singularities at the top wall slots and the intended near-zero normal velocity on the solid sidewall. At the corner, however, an undesired singularity is apparent. This anomoly results from the abrupt termination at the corner of the finite strength source sheet which forms part of the top wall flux discretizing singularity. This improper feature of the discrete slot simulation has not been corrected as of this writing because it is believed to have an insignificant effect on the simulation except in the immediate vicinity of the tunnel corner near regions of large slot flux. Specifically, its effect is excluded from the $\bar{\phi} = 0$ boundary condition and it does not introduce any erroneous source strength.

Longitudinal velocity perturbations at the walls are shown in fig. 6 in the form of longitudinal distributions in fig. 6a and lateral and vertical distributions in crossflow planes, selected where the longitudinal gradient of wall flux is large, in fig. 6b. In fig. 6b, the survey across the top wall in the discrete slot simulation was spaced inward from the top wall a distance equal to the slot control point recession distance ε. The survey taken very close to the wall and used for the w and v distributions of figs. 4 and 5, showed longitudinal velocity perturbations essentially identical to those of fig. 6b except in the immediate vicinity of the slots. The magnitude of the cyclic variation in u across the discrete slots can be related to the homogeneous wall case by considerations already discussed. Under the slender

body context, the flux through a slot in any crossflow plane was required to equal the total homogeneous wall flux over one slot spacing in the same crossflow plane. The resulting equality of the longitudinal distribution of wall flux (and, therefore, its gradient) is demonstrated by fig. 4a. The slotted wall condition expressed as eqn. (1) shows that the perturbation $u-u_p$ is proportional to the coefficient K if the flux gradient $\partial v_n d/\partial x$ is constant. By using fig. 3a to relate this coefficient for the discrete slot case to that for the homogeneous wall case, it is concluded that the perturbation $u-u_p$ must vary cyclically between $\tilde{K}/K$ times the homogeneous wall value at the slot control points to $(K+.22)/K$ times the homogeneous wall value midway between slots. Although the role of the plenum pressure, expressed herein as the equivalent velocity perturbation u_p, is discussed in a subsequent section, it is sufficient to state here that the value of u_p is essentially zero in all of the simulations with full length slotted walls. The longitudinal velocity perturbation distributions across the top wall shown in fig. 6c include the homogeneous wall distribution adjusted by the factors given above and illustrate that these adjustments do indeed define reasonable approximations to the upper and lower bounds of the cyclic distributions obtained in the discrete slot simulation. The longitudinal distributions given in fig. 6a verify that the magnitude of u at the top wall centerline is everywhere larger in the discrete slot simulation than in the homogeneous wall case, and that at the discrete slot control points is everywhere smaller than the homogeneous wall values. Velocity distributions at the sidewall center line are included in fig. 6a for comparison. With the point doublet and point source model disturbances (those with axisymmetric model-induced perturbations) the solid sidewall velocities show the not surprising tendency to depart more freely from the open-wall condition ($u = 0$) than do the velocities anywhere on the slotted wall.

The wall-induced velocity perturbations along the tunnel axis from the homogeneous and discrete slot simulations are compared in fig. 7. The agreement shown is excellent although not exact. It should be noted that although the effects of small changes in $\tilde{K}$ were examined, the baseline value of 2.263 used herein yeilded the best overall agreement with the homogeneous wall interference velocity distributions. When compared with the interference velocity magnitudes for the solid wall tunnel shown in fig. 2b, the discrepancies shown in fig. 7 justifiably can be called insignificant.

To check for limitations, the discrete slot simulation was used for lift interference prediction over the full range of slot widths from open to closed. Lift interference was chosen so that comparisons could be made with a different discrete slot simulation, the WALINT code of Steinle and Pejack (ref. 19), which is capable of lift interference prediction for infinite length slots.

Equations (8) and (9) show that in the present simulation, the slot width ratio a/d for discrete slots may be changed by varying either the boundary condition parameter $\tilde{K}$ or the control point recession ε. The equivalence of this simulation to the homogeneous wall representation was checked for the case of a point lift disturbance in a tunnel of infinite length having a

square cross section with solid side walls and six slots in each of the top and bottom walls. The results are given in fig. 8 which shows the lift interference parameter δ at the model location as a function of the slotted wall parameter P of the top and bottom walls. The homogeneous wall case, calculated using the Fourier transform series solution given in reference 16 for this tunnel geometry, is shown for comparison. The present discrete slot simulation with ε fixed at a small distance and $\tilde{K}$ varying showed excellent agreement with the homogeneous wall theory over the entire range of P from zero (solid wall, approximated by $\tilde{K} = 10000$) to 1.0 (open wall, requiring $\tilde{K} < 0$). With $\tilde{K}$ set at zero and ε varying, excellent agreement was obtained for values of P from 0.5 to 0.8. For $P > 0.9$ (corresponding to a/d above 0.22), ε becomes a significant fraction of the tunnel half height and the flow at the slot control points no longer represents the flow at the wall location. For $P < 0.48$ (a/d less than 3×10^{-5}) the calculated value of δ becomes that for the solid wall because ε diminishes into an arbitrarily dimensioned domain where the influence of the adjacent line source is calculated by a limiting form appropriate for $\varepsilon = 0$.

Results calculated by the WALINT method of Steinle and Pejack (ref. 19) are also shown on fig. 8. In this method, the tunnel walls are built up of infinite length panels. A boundary condition representing either a solid or a porous surface is imposed along the center line of each panel. For the results shown on fig. 8, each slot was represented by a panel with a width equal to the slot width and a very high porosity coefficient ($R = 10000$) in the boundary condition. Fair agreement with the homogeneous wall lift interference was obtained for $P > 0.6$ but significant error is apparent for lower values of P. For both discrete slot methods, control of the simulated slot width by controlling a geometric feature of the numerical representation (panel width in the WALINT method and control point recession in the present method) is applicable only in a limited range of slot widths. Control of the simulated slot width through the boundary coefficient $\tilde{K}$ in the present method appears to be free of such limitations. The present simulation of the homogeneous wall case predicted a lift interference at $P = .5$ which, although not shown on fig. 8, was indistinguishable from the theoretical result.

Alternative Slot Boundary Condition.- The slot boundary condition used in the baseline simulation, given by eqn (6), relates the local slot flux to the potential growth from the slot origin. An alternative condition relating the longitudinal gradient of slot flux to the local perturbation of longitudinal velocity is obtained by differentiating eqn (6) with respect to x. Because the line source strength is distributed in linearly varying segments, the flux gradient is expressed in finite difference form. The resulting slot condition is

$$u - u_p - \frac{1}{2}\tilde{K}\frac{\Delta S}{\Delta x} = 0 \qquad (10)$$

which is imposed at control points at the midpoint of each source line segment. The relationship between $\tilde{K}$ and the control point recession ε derived previously is assumed to be appropriate with this condition.

Distributions of vertical velocity at the walls obtained with this difference form of the slot boundary condition are illustrated in fig.9a for the point source disturbance along with the corresponding homogeneous wall results, and the wall-induced velocities on the tunnel axis are compared for all three point disturbances in fig.9b. It is apparent that the normal velocity at the solid-wall parts of the discrete slot wall reached much larger magnitudes than those for the integral slot condition case shown in fig. 4, but are distributed across the slotted wall in such a way that the net wall "leakage" at a given crossflow plane is still small. As a result, the distributions of the wall-induced solid-blockage and wake-blockage velocities agree reasonably well with the homogeneous wall results. In the lifting case, however, any errors in wall flux are of opposite sign on the top and bottom walls allowing errors in wall-induced upwash to accumulate with distance downstream without causing corrective feedback through the $\bar{\phi} = 0$ boundary condition.

Although sensitivity of simulation results to the longitudinal location of slot control points relative to the source line segments is not illustrated herein, such sensitivity was found to be significant when the difference form of the slot condition, eqn (10), was used but was essentially zero with the integral form of the slot condition, eqn (6).

Finite Slot Length Considerations.- Some illustrative results of simulations with slotted walls of finite length are compared in figs. 10 and 11 with those representing infinite length slotted and solid walls. The finite length slots were assumed to extend over the range of $x/2\beta h$ values from -1.58 upstream to 1.46 downstream of the location of the point disturbance representing the model. These locations are pointed out on the figures with the notations SO for slot origin and SE for slot end. Note that the simulated slot length expressed in units of h decreases with increasing Mach number. For the results shown, the solid-wall duct downstream of the slotted region was assumed to have an effective inviscid cross section area equal to that upstream of the slots.

Consider first the top wall longitudinal velocity perturbations shown on fig. 10 for the point doublet disturbance. In the solid wall case, the duct flow conservation enforced by the walls gives a velocity distribution with upstream to downstream symmetry. With infinite length slotted walls, this symmetry is retained with a plenum pressure parameter u_p of zero indicating that the outflow through the slots upstream of the point doublet is exactly balanced by the inflow occurring downstream. With the finite length slots, however, this balance is upset (for $u_p = 0$) and the total flow quantity sucked in through the slots becomes of the same order as that in the upstream duct so that the velocity in the downstream duct is approximately doubled. This sensitivity to slot length is a result of the slotted wall boundary condition (see eqn. (1) or eqn. (10)) which establishes the longitudinal gradient of slot flux as the local value of $u-u_p$, combined with the conservative governing equation which causes the value of u to respond to the accumulated slot flux, that is, the second integral of the of the slot flux gradient, from far upstream to the local station. Thus, any change in an

initial condition (at point SO for the finite length slots) is amplified with increasing distance downstream. This phenomenon is examined in detail in a subsequent section of the paper.

For more realistic simulations, the present program provides for constraining the total slot flux to a specified value which may be given as zero to represent a sealed plenum chamber around the test section, or as a nonzero value to simulate plenum bleed or pumping. The plenum pressure parameter u_p is treated as an unknown constant in the boundary condition at all slot control points. The sealed plenum condition was specified for the final curve on Fig. 10 which shows that a nearly symmetric distribution of u over the finite length slotted wall was achieved with a value of u_p^D of 0.015. These results are plotted on a larger scale in Fig. 11a along with the wall-induced solid-blockage velocity distribution on the tunnel axis. The effect of finite slot length is seen to be a shift in both distributions, the magnitude of which approximates the change in u_p^D over most of the finite slotted region.

Similar comparisons for the point source disturbance are shown in Fig. 11b. The source strength corresponds to the flow quantity displaced by the wake of a model with viscous drag. With finite length slots and a sealed plenum ($u_p^S = .025$), the added flow quantity in the downstream solid-wall region results in a positive perturbation of both top wall velocity and wall-induced (wake blockage) velocity. At the model location, both the magnitude and gradient of the wake blockage velocity lie roughly half way between the solid-wall and infinite-length slotted-wall results. As an alternative, the displaced flow quantity was removed by plenum suction ($u_p^S = .033$) resulting in near zero velocity perturbation in the downstream solid-wall region. For this case, the interference velocity at the model location was shifted from the infinite-length slotted-wall value by nearly the value of u_p^S.

Results with the point lift disturbance are given in fig. 11c. With this disturbance the distributions of u^L on the bottom wall (not shown) are equal and opposite to those shown for the top wall and the wall-induced velocity on the tunnel axis is directed vertically. With finite-length slots, the wall-induced upwash must become large enough to cancel the downwash induced by the test model and turn the flow back to the direction of the tunnel axis. This turning is associated with a velocity peak at the downstream end of the top wall slots and a corresponding velocity depression on the bottom wall (not shown). Without special treatment, the turning probably is too abrupt to be realistic for those slotted-wall tunnels which utilize a reentry flap to promote smooth flow at the downstream end of the slots. In such tunnels, the pressure in the confined region between a slot and its reentry flap must depart from the plenum pressure in such a way that the slot flux is reduced smoothly to zero at the slot end.

To simulate such a reentry flap in the numerical model, the slot boundary condition is altered for those control points lying between the flap leading edge and the slot end to include an increment in u_p which varies linearly from zero at the flap leading edge to an unknown value u_f at each slot end while the value of S at each slot end is set to zero. In the differential form of eqn. (10) the altered slot boundary condition may be written

$$u - (u_p + f u_f) - \frac{1}{2} \hat{\gamma} \hat{K} \frac{\Delta S}{\Delta x} = 0 \tag{11}$$

whereas the integral form becomes

$$\phi - \phi_0 - u_p(x - x_0) - \frac{1}{2} f^2 c u_f - \frac{1}{2} \hat{\gamma} \hat{K} S = 0 \tag{12}$$

where f is set to zero for all slot control points lying upstream of the flap leading edge. The effectiveness of this reentry flap model in smoothing the flow at at the downstream end of a top wall slot in the finite length solutions of fig. 11c is illustrated in fig. 12 where values of longitudinal velocity perturbation and slot flux at the slot control points are shown. The location of the reentry flap leading edge is indicated by the notation RF. The lift interference results shown on fig. 11c indicate that although the reentry flap causes the downstream slot end effects to be felt somewhat farther upstream, all finite length effects for the case illustrated are confined to the region downstream of the point lift disturbance. It should be noted that the same reentry flap illustrated in fig. 11c was included in the finite slot length illustrations of figs. 11a and 11b but its effect was not very pronounced with the doublet and source disturbances.

Nonlinear Slot Flow Characteristics

Perhaps the most technically advanced understanding at present of the nature of slotted wind tunnel wall flows is embodied in a flow model which was defined initially in the study reported in ref. 13 and is described more graphically in ref. 17 which also describes a general inviscid theory for its application. Ref. 8 describes the incorporation of simplified viscous effects into this theory and its subsequent implementation for the case of transonic axisymmetric (and therefore nonlifting) flows. Two important nonlinear features are embodied in the slot flow model of ref. 17. The first is the accounting for the dynamic pressure of transverse flow in the slots as part of the pressure difference across the slotted wall. The second is the provision that ingestion of low-energy plenum air into the tunnel allows the plenum pressure to be felt on a boundary inside the tunnel. These two features have been incorporated in a somewhat simplified form as options in the present simulation program. The simplification includes the assumption that all slot flux in the inward direction represents ingestion of low-energy air. It follows that the transverse dynamic pressure accounting should be included only for slot outflow, and then only after all plenum air previously ingested through the same slot has been ejected.

In the present numerical model, the outflow dynamic pressure effect is accounted for by a quadratic term in the slot boundary condition. In the form of eqn. (1), this term would be written in the right hand side as $-v_n^2 d^2/2a^2$. Using the substitution $S = -2dv_n$ leads to the discrete slot form $-S^2/8a^2$. In ref. 20, Wood multipies this term by $[(\pi+2)/\pi]^2$ to represent the contraction of a Helmholz jet separating from the slot edges. The treatment in ref. 13 on the other hand, simply recognizes that viscous accounting might call for an equivalent inviscid slot width smaller than a. In the present simulation, the value of a used in the quadratic term is an input quantity independent of $\tilde{K}$. For the illustrations in this paper, the inviscid value corresponding to $a/d = .06$ was used.

The nonlinear effect of slot inflow is modeled under the assumption that all fluid entering the tunnel through each slot has low velocity and accumulates in a tubular bubble which is semicircular in cross section and centered on the slot. The cross section area of the bubble is the longitudinal integral of half the line source strength starting at the origin of inflow. Under the assumption that the air in the bubble is essentially quiescent, the plenum pressure should be felt at the boundary of the bubble. Conceptually, this boundary condition on the tunnel flow could be implemented by setting $\tilde{K} = 0$ in the slot boundary condition equation (6) and imposing the resulting condition at control points recessed into the tunnel by the radius r_b of the bubble. The computational work for this procedure would be very large because of the need to recalculate the influence coefficients of all singularities on the relocated control points and solve a new matrix equation at each iteration step.

In the procedure actually used, the slot control points are held at the fixed recession distance ε and the $y = 0$ curve of Fig. 2 is used to approximate the value of $\tilde{K}$ at $z = \varepsilon$ which would result in $\tilde{K} = 0$ at $z = r$ where r is related to r_b through an arbitrary attenuation factor F_r defined as

$$F_r = \frac{r - \varepsilon}{r_b - \varepsilon} \tag{13}$$

For this purpose, the $y = 0$ curve of Fig. 2 is represented analytically as

$$\Delta K'_r = \frac{r}{d} - \frac{1}{\pi} \ln \csc\left(\frac{\pi}{2}\frac{a}{d}\right) \tag{14}$$

where a/d is expressed as a function of r/d by use of equation (9). The nonlinear slot boundary condition now may be written

$$u - (u_p + f u_f) - \frac{1}{2}\hat{\gamma}\tilde{K}\frac{\Delta S}{\Delta x} = \begin{cases} \dfrac{-S^2}{8a^2} & , S<0 \text{ and } r_b = 0 \\ \dfrac{1}{2}\Delta\hat{K}\dfrac{\Delta S}{\Delta x} & , S \geq 0 \text{ or } r_b > 0 \end{cases} \tag{15}$$

where

$$\Delta\hat{K} = -\hat{K} + \Delta K'_{\varepsilon} - \Delta K'_{r} \tag{16}$$

Note that if an outflow region occurs downstream of an inflow region, the outflow is used first to reduce the bubble radius to zero before the outflow dynamic pressure term is invoked. In the preferred integral form, the nonlinear slot boundary condition is written

$$\phi - \phi_o - u_p(x-x_o) - \tfrac{1}{2}f^2 c u_f - \tfrac{1}{2}\hat{K}S = \begin{cases} \int_{x_o}^{x} -\frac{S^2}{8a^2}dx_1, & S<0 \text{ and } r_b=0 \\ \tfrac{1}{2}\Delta\hat{K}S, & S\geq 0 \text{ or } r_b>0 \end{cases} \tag{17}$$

where the integral along the slot is evaluated with recognition that S is discretized into linearly varying segments and can change sign within a segment.

To solve the system of equations, the nonlinear terms, which are included in the right hand side of the system of otherwise linear equations, are ignored in a first trial solution and then evaluated iteratively for subsequent solutions. The Gaussian elimination procedure used to solve the system invokes a triangular factorization of the left hand side coefficient matrix followed by back substitution of the right hand side. By saving the factored matrix from the first iteration, the computer time required for 100 subsequent iterations was about the same as that used for the first trial solution. Solution convergence to a maximum residual of 10^{-6} of the largest nonlinear term required between 20 and 200 iterations for the cases illustrated in this paper. A typical solution did not benefit from underrelaxation but a small amount of smoothing was required in the distribution of S along each slot to stabilize a slowly divergent mode which was observed as a spacial oscillation in regions of large slot inflow.

In view of the approximate nature of the slot inflow modeling procedure, the slot inflow regions of several solutions using eqn. (17) for the slot boundary condition have been examined in detail to determine how closely the pressure at the inflow bubble boundary matched the plenum pressure. Some of the results are illustrated in fig. 13 which shows longitudinal velocity perturbations in the vicinity of the top wall slot nearest the centerline from four solutions with the point lift disturbance. For the first solution, the only nonlinear term included in the slot boundary condition was the outflow dynamic pressure term. Because all significant flux through this top wall slot was in the inflow direction, the results shown for this case can be interpreted in terms of the linear slot condition expressed by eqn. (11). The perturbation u at the slot control points is shown on fig. 13 by the square symbols and the plenum condition $(u_p + fu_f)$ is shown by the solid line. The difference between these two is indicative of the local pressure difference across the slot which is resisted, according to eqn. (11), by the slot streamline curvature.

The remaining three solutions shown on fig. 13 satisfied the complete slot boundary condition given as eqn. (17) but different values of F_r were used to evaluate $\Delta\tilde{K}$. Eqn. (13) shows that values of F_r less than unity attenuate the boundary condition shift from the actual control point at $r = \varepsilon$ toward a virtual control point at $r = r_b$. With $F_r = 0$, no shift takes place and eqn. (16) reduces to $\Delta\tilde{K} = -\tilde{K}$ thereby canceling the slot streamline curvature effect. The $F_r = 0$ plot on fig. 13 verifies that the plenum and reentry flap pressures were well reproduced at the slot control points. These solutions were surveyed along lines extending inward from the slot control points to determine the u perturbation at the inflow bubble boundary, shown on fig. 13 by the circle symbols. For all three solutions, the values of bubble radius at $x/2\beta h = .08$ fell in the range $r_b/h = .026 \pm .001$ and at the slot end, in the range $.10 \pm .01$. With $F_r = 0$, the u perturbation at the bubble boundary departed significantly from the target plenum distribution at longitudinal locations near the lift disturbance at $x = 0$ and in the reentry flap region. The solution with $F_r = 1$ shows that the unattenuated boundary condition shift to the bubble boundary caused an excessive reduction in u in the vicinity of the lift disturbance. The intermediate value of $F_r = .3$ is seen to yield a more balanced overall agreement between the u perturbation on the bubble boundary and the plenum and reentry flap distribution and was, therefore, chosen as the appropriate value of F_r for subsequent simulations.

The effects of the two nonlinear slot flow phenomena on simulated tunnel flow and wall interference properties are illustrated in fig. 14 for the point lift disturbance and in fig. 15 for point doublet and point source disturbances. With a nonlinear boundary condition, the normalized form in which the results are presented no longer renders them independent of disturbance magnitude. The disturbance strengths selected represent a model size somewhat larger than that usually tested in a slotted test section and correspond to a lift of $C_L S/C = .04$, a point doublet giving solid blockage of $V/h^3 = .025$, and a point source corresponding to $C_D S/C = .02$.

For the lifting case, the flux distributions on the top wall and bottom wall slots are shown in figs. 14a and 14b respectively. The effect of the outflow nonlinearity is to reduce the outflow peaks occurring on the bottom wall slots downstream of the model and to distribute the outflow more uniformly across the three bottom wall slots. To compensate for outflow reduction in this region, the positive value of u_p (shown in fig. 13) caused increased outflow through the upstream part of the bottom wall slots and an overall decrease in the top wall slot inflow. The addition of the nonlinear condition on inflow tended to concentrate the top wall inflow into a region downstream of the model and near the wall center line. The associated further increase in u_p caused an outflow condition over the upstream portion of the top wall slots and a general increase in outflow through the bottom wall slots. The u perturbation surveys at the top and bottom wall center lines given on fig. 14c show that the slot nonlinearities cause a significant

redistribution of the perturbation peak magnitudes and imply that proper accounting for the slot flow nonlinearities will be important in matching a simulated slotted tunnel flow to measured wall pressures. The wall interference velocities at the tunnel axis (fig. 14d) show that the effect of each type of slot nonlinearity on the wall-induced upwash is significant but the two effects tend to cancel each other. The most important effect of the nonlinearities is to cause a wall-induced decrement in longitudinal velocity as part of the lift interference. This form of wall interference, which does not exist with a linear slot boundary condition, results from the previously discussed effects of the nonlinearities on the slot flux distributions which produce a net outflow upstream of the lift disturbance and a net inflow downstream.

The effects of slot flow nonlinearity on simulations with point doublet and point source disturbances are illustrated in figs. 15a and 15b respectively. Although the nonlinear effects are less dramatic in these cases than in the lifting case, it is observed that with all three model disturbance types, the effect of either nonlinearity is to drive the wall-induced longitudinal velocity perturbations in the negative direction. This results from a phenomenon common to all disturbances which balances the nonlinear term action to restrict outflow or enhance inflow over the downstream portion of the slots against the reduced plenum pressure which acts over the entire slot length to promote outflow.

Mach Effects

All of the simulation results presented in the preceding sections of this paper were obtained from simulations with Mach number specified as zero. The results are presented in a normalized form which renders them applicable at all subsonic Mach numbers for which linearized compressibility accounting is suitable. In the case of finite slot length, however, it was noted previously that the test section geometry corresponding to the normalized results varies with the assumed Mach number. Mach number effects on wall interference in a fixed geometry test section are illustrated in fig. 16 for simulations with both linear and nonlinear slot boundary conditions. Results with point doublet, source and lift disturbances are shown in figs. 16a, 16b and 16c respectively.

In the normalized form used, the effect of increasing Mach number is identical to the effect of stretching the test section geometry in the longitudinal direction by the factor $1/\beta$. Fig. 16 shows that with the linear slot boundary condition, the resulting wall-induced velocities at the disturbance location are closer to the infinite slot length predictions at high Mach number than at Mach number zero. Inclusion of the nonlinear terms in the slot boundary condition, on the other hand, apparently has more effect at high Mach number than at Mach number zero. This is particularly true in the lifting case for which the magnitude of the wall-induced longitudinal velocity decrement increases with Mach number by approximately the same factor $(1/\beta)$ as the effective incompressible slot length.

Model and Sting Simulation

The present simulation program provides for representing the wind-tunnel test model either by the point doublet, source and lift disturbances used in the simulations discussed in the preceding sections or by a system of distributed singularities capable of a much more realistic simulation of the perturbations felt at the tunnel walls from a wing-body-tail test model. It should be emphasized that the requirements for the distributed singularity representation are based on use of the test section flow simulation as an element of an interference assessment procedure. These requirements include matching total forces and moments to prescribed values and accurate predictions of model-induced perturbations at the tunnel walls. Desired features include modest computational resource requirements and convenient application to "quick look" situations where load distributions are not available in detail. Note that accurate flow simulation at the model surface is not a requirement.

The model representation in the present program was evolved from that used by Rizk and Smithmeyer (ref. 6). The body representation was extended to include crossflow effects for arbitrary body camber and angle of attack and to include the displacement effects of a separated wake. Details of the body modeling and the similar modeling used for the model support sting are given in Appendix D. The wing and tail modeling are nearly the same as those of ref. 6 but the present formulation allows a finite thickness wake to be shed from the trailing edge. Appendix E describes the wing and tail representation in more detail. The model representation can be characterized simply as a set of singularities located on easily described lines in the model interior with strengths calculated from local geometric properties of the model. No model surface boundary conditions are imposed. The far field properties of the model-induced flow are those appropriate to the model volume, wake displacement and lift. Figs. 17 and 18 are presented to illustrate that the near field flow is represented with only modest discrepancies.

Fig. 17 illustrates some capabilities of the body and sting modeling. The flow modeled is that around an isolated body of revolution (not in a wind tunnel) consisting of a cylindrical center portion and ogive nose and tail portions. In arbitrary length units, the body extends from station -5 to +5 and the portion between stations -4 and +4 is cylindrical with a radius of 0.4 units. The flow properties shown are perturbation velocity components on straight survey lines displaced one body radius from the axis in the direction of one or two values of the azimuth angle, θ. Thus, within the cylindrical region, the velocities shown are those at the location of the simulated body surface. Results for body angles of attack of 0°, -90° and -45° are shown in figs. 17a, 17b and 17c respectively. At the non-zero angles of attack, the windward attachment line is at $\theta = 0$ where the solid cylinder surface condition would be satisfied by $u = -1$ at -90° angle of attack and by $u-w = -1$ at -45° angle of attack. At the body shoulder ($\theta = 90^{\circ}$) the solid cylinder surface condition would require $v = 0$ at all angles of attack. The results given on fig. 17 show that the body representation approximated these surface conditions very well over most of the cylinder length but discrepancies existed near the cylinder-ogive junctures. The maximum velocity

error was less than 8 percent of U_∞.

The part of the body at negative body stations was identified to the simulation program as the test model and the part at positive stations is identified as the sting. Interference perturbations are defined in the simulation program as the perturbations arising from all singularities except those representing the test model. Thus the values of $\Delta_I u$ and $\Delta_I w$ shown on figs. 17b and 17c are velocity perturbations due to the sting. Interference velocities are not plotted on fig. 17a because at zero angle of attack they are practically indistinguishable from the total perturbations over the sting and from the zero axis upstream of the sting. The absence of an interference peak at the model-sting juncture shows that the simulation properly recognized that the sting origin at body station zero is shielded from the onset axial flow by the blunt base of the model. This shielding does not apply to crossflow, however, so the interference velocities at non-zero angle of attack show rapid variation in the vicinity of the model-sting juncture.

It should be noted that in a typical wind tunnel test simulation, the juncture of the model and its support is the only place where interference perturbations are felt on the model within the near field of the interfering element. Results from such a simulation with the present program should be used with caution not only because of the near field shortcomings of sting simulation discussed above but also because the present inviscid simulation does not account for viscous coupling between model and sting.

As indicated in Appendix E, the perturbation fields induced by the thickness and lift distributions over a wing or tail are approximated by expressing the influence of the chordwise distribution at each spanwise station as the first four terms of a series derived from binomial expansion about the 50 percent chord line. The far field asymptotes of the significant properties of the wing-induced flow are produced by the first term of the lift series and the first two terms of the thickness series and therefore are not affected by truncating the series to four terms. The numerical integration used in the spanwise direction is simply a summation of the influences of singularities concentrated at discrete spanwise stations which yields a low order approximation to the influence of a continuous spanwise distribution of singularities. Again, the far field accuracy of the flow properties is not compromised by this approximation.

The near field effects of these approximate representations have been examined for the case of an isolated rectangular wing of aspect ratio 6. For the thickness problem, the airfoil section at all spanwise stations was the polygon whose corners are defined by the standard coordinate table for the NACA 0012 airfoil section. A full continuous surface representation of this thickness distribution was set up within the present simulation program as a network of source panels having strengths specified as the chordwise thickness gradient of each segment of the polygonal airfoil representation. The four thickness series coefficients were determined by chordwise integration of this same source distribution. Pressure coefficient distributions in each solution were calculated along the nine longitudinal survey lines located relative to the wing as indicated in Table I. The distributions along the line one chord

length above the wing midspan are shown in fig. 18. The term by term buildup of the series solution is compared with the source panel solution indicated as the series limit on fig. 18. The maximum discrepancy between the four term series solution and the limit solution is less than 6 percent of the maximum C_p magnitude and occurs near $x/c = 0$ where the x origin is at the airfoil 50 percent chord location. Similar comparisons on all nine survey lines are summarized in Table I.

For the lift series evaluation, the flow field used as the series limit was obtained from a vortex lattice solution for the same rectangular aspect ratio 6 wing at unit lift coefficient. The spanwise stations for the series representation were located at the vortex lattice boundaries and the series coefficients at each station were evaluated by averaging the two adjacent chordwise summations of the discrete vortex strengths and their appropriate moments. The C_p distributions on the survey line one chord length above the wing midspan shown for the lift series in fig. 18 again indicate that the maximum difference between the four term series and the series limit solutions occurs in the wing near field and is, in this case, less than 3 percent of the maximum C_p magnitude. The summary given in Table I shows that larger relative discrepancies occur, for the lift case, on those survey lines located near the wing tip. It is believed that in this region, the error resulting from the low order of spanwise lift distribution associated with the present representation is more important than that resulting from chordwise series truncation.

COMPARISON WITH EXPERIMENTS

The DFA Wall Pressure Experiment

Ref. 21 describes an experiment that consisted of static-pressure measurements on the walls of a slotted transonic tunnel test section during force tests of two sting-supported models. One of the test points of that experiment has been the subject of several simulation runs using the present program. Presented herein are a brief description of the simulated case, a comparison of the simulated and measured wall pressures, and illustrations of the effects of changing several simulation parameters both on wall pressures and on tunnel interference.

The experiment was conducted in the Diffuser Flow Apparatus (DFA) which is described in ref. 22. For the particular case simulated, the larger of the two models used in the experiment was installed at an angle of attack of 3.23° and tested at a Mach number (based on empty tunnel calibration) of 0.5873. For these conditions, the model is characterized by $V/\beta^3 h^3 = .060$, $C_D S/\beta^2 C = .011$, and $C_L S/C = .016$. A sketch of the test section and model installation are shown in fig. 19. Note that the model is inverted in the tunnel and is located slightly below the tunnel axis. The slot open area ratio a/d increased from zero at the slot origin to a maximum of 0.0915, decreased to a minimum of 0.0351, then increased to a value of 0.06, the

constant value in the vicinity of the test model. These variations in slot width were specified in the basic DFA simulation along with corresponding variations in $\tilde{K}$ which was given as 2.263 in the vicinity of the model and held constant over the reentry flap. The increasing slot width over the reentry flap was specified for use in the nonlinear outflow term. It was assumed for simulation that the divergent slopes of the upper and lower walls indicated on fig. 19 were just sufficient to compensate for boundary layer growth on all four walls. The step increase of about 7 percent in tunnel height at the downstream end of the slots provides a region for mixing with low energy flow to form, in effect, a thick boundary layer in the entrance to the solid-wall diffuser. For the basic DFA simulation, it was assumed that the displacement thickness of this layer just filled the step in tunnel height. In some variant simulations, however, a 5 percent increase in the effective inviscid tunnel height at this point was simulated by turning the streamlines outward in the reentry flap region by means of a negative strength source panel superimposed over the reentry flaps.

The effects of some of the geometric features of the DFA simulation on longitudinal velocity distribution through the tunnel are shown in fig. 20 which gives the u-perturbation on a survey line located between the tunnel axis and sidewall close to the model wing plane. The effect of simulating a 5 percent step in effective tunnel height at the slot end is shown as are the effects of removing the model and the sting. With the model and sting removed, the test section flow is essentially unperturbed upstream of $x/h = 6.1$ where the sidewall shaping begins. Addition of the sting produced a velocity decrement in the test section due to the upstream influence of the sting flare, followed by a marked velocity increase where the duct area blocked by the sting was significant. The change in perturbation velocity due to the further addition of the test model is characteristic of the effects of the model volume and is much smaller in peak magnitude than that due to the sting.

Pressure coefficients from the DFA experiment in three rows on each of the top and bottom walls and five rows on the sidewall are compared with those at the same row locations from the DFA simulation in fig. 21. As noted in ref. 21, the wall pressure coefficients measured in runs with the model and sting removed showed variations of significant magnitude relative to those measured with the model and sting installed. For this reason, the experimental values shown in fig. 21 are in the form of the "adjusted C_p" of ref. 21, i.e. the empty tunnel value at each orifice has been subtracted out. The simulation results on fig. 21 were obtained in a run identical to the basic DFA simulation except that the entering velocity was set by the requirement that the sidewall C_p value at $x = .36h$ and $z = 0$ should match the experimental value. On the top and bottom walls, simulation results were not obtained at $y = 0$. Instead, C_p values at the simulation control points at $y = .083h$ are compared with the experimental row at $y = 0$.

The simulation results generally exhibit the same characteristic features that are apparent in the experimental C_p distributions although the magnitude and location of the features might differ. For example, on the bottom wall,

the suction peak associated with the suction surface of the inverted lifting model is clearly apparent in both the experimental and simulated results, the magnitudes of the negative C_p peaks and the gradients upstream and downstream of the peaks are similar but the experimental suction peaks are located farther downstream than those from the simulation. On the side wall, the experimental and simulated results agree reasonably well and both show a pronounced vertical gradient of C_p in the region opposite the model wing ($x/h \cong 3.5$). The downstream end of all of the simulated distributions show the beginning of the transition of the sting flare influence from positive pressures upstream to negative pressures downstream which was pointed out relative to fig. 20. A similar trend toward negative C_p downstream is found in all of the experimental distributions that extend to $x/h = 4.5$. The most serious discrepancy betwen the experimental and simulated wall pressures occurs on the top wall where the positive pressure peak at $x/h \cong 3.7$ which is apparent in the simulated results is almost nonexistent in the experimental data. No reason for this discrepancy is offered herein.

As stated previously, one of the reasons for developing the present simulation program was to use it in a tunnel interference assessment procedure. In such use, certain parameters of the simulation would be made responsive to measured wall pressures. As initially envisioned, $\tilde{K}(x)$ on each slotted wall or even on each slot was the primary candidate for the set of adjustable parameters. The effects of arbitrary and gross changes in $\tilde{K}$ along the entire length of all slots on top and bottom wall pressures and on interference velocity components near the tunnel axis are shown on fig. 22. The maximum change in wall pressure resulting from the global change in $\tilde{K}$ illustrated on fig. 22 is observed to be about twice the magnitude of the maximum difference between the experimental and simulated wall pressures on fig. 21. This observation leads to doubt that local changes in $\tilde{K}(x)$ would be capable of matching the simulated wall pressures to the distributions measured in this experiment.

In seeking other simulation parameters which might be adjusted to improve agreement with measured wall pressures, particular attention should be paid to areas where the validity of modeling assumptions might be questioned. One such area is the vicinity of the downstream end of the slots where the change in effective inviscid tunnel height is not well defined. Also, in view of the previously demonstrated sensitivity of the tunnel flow to plenum pressure, the assumption of a perfectly sealed plenum could be questioned. The effects on top and bottom wall pressures and on tunnel interference velocities of the 5 percent change in effective tunnel height at the slot end introduced in fig. 20 and of removal or addition of 5 percent of the tunnel flow through the plenum are shown on fig. 23. These simulation parameters do not provide much help in making localized changes in wall pressure but their effect on the general level and gradient of wall C_p is large enough to suggest that they should be considered for inclusion in the total set of adjustable parameters. It is unfortunate that wall pressures were not measured downstream of $x/h = 4.5$ in the DFA experiment. The velocity distributions of fig. 20 suggest that the addition of wall pressure measurements just downstream of the slot ends would be of great value in determining the proper magnitude of the

slot end step representation.

The values of the plenum pressure parameter u_p and of the maximum radius of the low energy inflow bubble at the downstream slot end for each of the simulations shown on figs. 22 and 23 are listed in the accompanying table. Low energy inflow occurred through the bottom wall slots starting at x/h near 3.2 for all cases except the 5 percent plenum suction case which eliminated all slot inflow. Because inflow allows the plenum pressure to be felt inside the tunnel, the bottom wall pressures of fig. 23 (except for plenum suction) are essentially insensitive to the simulation changes and those of fig. 22 are related closely to the change in u_p with $\tilde{K}$.

Case	u_p	$r_{b,max}/d$
Basic DFA	.00044	.276
5% step	.00057	.264
5% suction	.00146	0
5% injection + step	.00035	.441
$\tilde{K}$ = 10	.00529	.196
$\tilde{K}$ = 0	-.00023	.328

The interference velocities shown in figs. 22b and 23b are those on a survey line passing longitudinally along the model wing at y/h = .2. This line lies in close proximity to the sting, the influence of which dominates the interference perturbations downstream of the model base at x/h = 4.1. The interference distributions demonstrate that the interference at the model predicted by the simulation is responsive to the simulation parameters which might be adjusted to match the simulation to measured wall pressures.

Simulation of Rapid Slow-Down

One of the structural design conditions for a transonic wind-tunnel test section is the dynamic condition following a sudden loss of tunnel drive power. In steady operation at a transonic Mach number, the plenum chamber is a large volume reservoir in which the density is much less than that in most of the remaining tunnel volume. During a reduction in Mach number, a density readjustment takes place requiring a transfer of mass from the tunnel to the plenum chamber at a rate dependent on the plenum volume and the rate of Mach number decrease. The pressure difference between tunnel and plenum required to produce the mass transfer must be resisted by the wall structure. If it is assumed that all of the mass is transferred through the wall slots of a slotted test section, the present simulation program can be used to provide a quasi-steady simulation of the instantaneous flow in the test section at some instant in the dynamic process.

Experiments have been made in the National Transonic Facility (NTF) at NASA Langley Research Center in which dynamic instrumentation was used to measure the time history of pressure difference across the test section sidewall at four longitudinal locations on the wall centerline during

maximum-rate slowdowns from an initial steady state at Mach number of unity. Simultaneous time histories of other quantities including plenum pressure were measured. Data from one such run at the instant of peak sidewall pressure difference have been used to establish the conditions for a quasi-steady simulation. At this instant, the Mach number entering the test section was found to be .86 and the total outflow quantity through the slots was calculated to be .0715 of the flow rate entering the test section. This calculation was based on the instantaneous rate of increase of plenum pressure, the known plenum volume and the assumption that plenum temperature was equal to the static temperature in the tunnel at M = .86. For the simulation, the slotted-wall geometry was the same as that shown in fig. 19 for the DFA experiment except that in the reentry flap region, $\tilde{K}$ was set to 1000 to represent the opinion that for this large amount of slot outflow, the reentry flaps would act essentially as a solid wall. No model, sting, sting support sector nor expanding diffuser were represented in the simulation.

Compressibility effects are represented in the simulation in a linearized form valid for small perturbations from the specified Mach number. Isentropic relations for one-dimensional flow indicate that removing .0715 of the mass flow rate of a Mach .86 flow results in a Mach number of .70 in the same duct area. Simulation runs were made with Mach number specified as each of these two values. The total slot outflow of .0715 of the entering flow was specified for both simulations. The resulting pressure coefficient distributions on the sidewall center line are compared in fig. 24 with measured values at the four longitudinal locations. The effect of Mach number on the experimental values simply reflects the effect of changing the reference Mach number used for reducing the dimensional measured pressures to coefficient form. If it is reasoned that the comparison between experimental and simulated results should be made using the M = .86 results as a limit for the upstream end of the slots, and the M = .70 results as a limit for the downstream end, the agreement could be called good. The possibility should be recognized that dynamic effects not represented in the quasi-steady simulation might be significant. One such effect is the apparent pressure gradient associated with the finite propagation rate of the pressure change across the tunnel fan. The upstream traveling compression ramp might produce a particularly significant contribution because it is steepened by the downstream flow velocity in the test section.

CHARACTERISTIC MODE OF TUNNEL/PLENUM INTERACTION

Many of the simulation results involving finite length slots discussed in the foregoing sections exhibit the effects of a common pattern of interaction relating the plenum mass flow constraint, plenum pressure, slot boundary condition and effective capture area at the downstream slot end to the longitudinal distribution of tunnel flow pressure or longitudinal velocity perturbation. The results shown on fig. 10 which were used to introduce the effects of finite slot length demonstrate clearly that the velocity distribution through the slotted tunnel is highly sensitive to small changes in plenum pressure.

In an attempt to clarify the role played by plenum pressure in these interactions, an analysis has been performed in which the tunnel flow is simplified to the one-dimensional flow in a constant area duct with transpiration through the duct walls governed by the slotted wall boundary condition. A similar analysis for the case of perforated walls is described if ref. 23.

With compressibility effects expressed by the Goethert rule, flow continuity requires that the duct velocity be related to the wall transpiration by

$$ndv_n dx = -\beta^2 C du \tag{18}$$

where the product of number of slots and slot spacing expresses the slotted wall perimeter. The homogeneous slotted wall boundary condition expressed as in eqn. (1) is the appropriate form for this simplified analysis because in the homogeneous wall form, the longitudinal velocity perturbation u is more representative of an average tunnel value than that localized to the slot vicinity used in the discrete slot condition. Differentiating eqn. (18) leads to

$$\frac{dv_n}{dx} = -\frac{\beta^2 C}{nd}\frac{d^2u}{dx^2}$$

which is substituted into eqn. (1) to give

$$u - u_p - \frac{\beta^2 CKd}{nd}\frac{d^2u}{dx^2} = 0 \tag{19}$$

Let λ be defined as

$$\lambda = \sqrt{\frac{\beta^2 CK}{n}} \tag{20}$$

which has units of length and is characteristic of the slotted tunnel geometry and Mach number. Eqn. (19) may now be rearranged as

$$\frac{d^2u}{dx^2} - \frac{1}{\lambda^2}u = -\frac{1}{\lambda^2}u_p$$

which is satisfied by the solution

$$u = u_p + c_1 e^{x/\lambda} + c_2 e^{-x/\lambda}$$

At the slot origin, identified as $x = 0$, the flow should be unperturbed, that is,

$$\left.\begin{aligned} u &= 0 \\ \frac{du}{dx} &= 0 \end{aligned}\right\} \quad x = 0$$

Note that eqn. (18) shows that the second constraint is equivalent to $v_n = 0$. These two constraints are satisfied by setting the constants of integration to

$$c_1 = c_2 = \frac{1}{2}u_p$$

The solution then becomes

$$u = u_p\left[1 - \frac{1}{2}(e^{x/\lambda} + e^{-x/\lambda})\right] \tag{21}$$

This solution may be interpreted as the shape of a characteristic mode of $u(x)$ within a slotted test section. At locations where x/λ is greater than $O(1)$ this mode is dominated by the exponential $e^{x/\lambda}$. The magnitude of the mode can be established by specifying either u_p or the value of u at the downstream end of the slotted section. Because eqn. (19) is linear, the $u(x)$ defined by this solution can be superimposed on the distributions arising from other disturbances if the boundary conditions satisfied are linear.

Figs. 10 and 11b both illustrate the effects of a change in the specified level of plenum flow rate for two different model disturbances. These cases are characterized by values of $K = 3$, $n = 12$, and $C = 4h^2$ from which the characteristic length is found to be $\lambda = \beta h$. For both disturbances, the change in downstream velocity relative to the change in plenum pressure is $\Delta u/\Delta u_p = -68.4$ which satisfies eqn. (21) with a slot length of $4.93\beta h$. The presence of a reentry flap in both simulations introduces uncertainty as to the effective slot length in the context of eqn. (21). The actual slot length in the simulation is $4.88\beta h$ to the reentry flap leading edge or $6.09\beta h$ to the slot end.

In the rapid slow-down simulations of fig. 24, the specified flow rate from tunnel to plenum is the only disturbance driving the simulation. In this case, the active slot length is well established at $4.92h$ because of the large value of $\tilde{K}$ specified over the reentry flaps. The nonuniform slot width (and $\tilde{K}$), however, as well as the use of the nonlinear slot boundary condition prevent a direct quantitative comparison with eqn. (21). The accompanying table shows that the reduced slot length x/λ predicted by eqn. (21) using u/u_p from the simulation is 25- to 35-percent low if λ is assumed to be βh. The discrepancy could be reduced by assuming an increase in K which would increase the resistance to slot flux thereby acting in the same direction as the slot outflow nonlinearity.

Mach number	.70	.86
slot length/βh	6.88	9.68
downstream u/u_p	-40.4	-701.6
x/λ from eqn. (21)	4.41	7.25

Although the simplifying assumptions used in the derivation of eqn. (21) must introduce some inaccuracy, the agreement with simulation results is good enough to justify the use of eqn. (21) as an aid to the conceptual understanding of the flow phenomena in finite-length slotted test sections. An important observation is that for slot lengths greater than about 5.5 times the characteristic length λ, the difference between plenum pressure and tunnel static pressure at the slot origin is at least two orders smaller than the pressure perturbation in the tunnel at the downstream end of the slots. This finding has a bearing on the suitability of plenum pressure as a calibration reference for tunnel static pressure. With regard to wind tunnel dynamics, the response to a change in the pressure difference between the upstream and downstream ends of the slotted region should be characterized by a rapid adjustment of the magnitude of the pressure distribution expressed by eqn. (21) at a rate governed by the pressure propagation time along the plenum and across the test section. The change in slot flux should be similarly rapid. The plenum pressure, however, should change at a much slower rate governed by the time constant of the first order dynamic process governing the filling of the plenum chamber volume. Eqn. (21) shows that with sufficiently long slots, the tunnel static pressure at the slot origin is essentially locked to the plenum pressure and, therefore, must lag behind the pressure change at the downstream end of the slots.

CONCLUDING REMARKS

The computer program described herein provides for simulation of the subsonic flow in slotted-wall wind tunnel test sections with recognition of several important features usually omitted from prediction of slotted tunnel wall interference. These features include discrete, finite-length wall slots with reentry flaps at the downstream ends, subject to the slot flow rate constraints imposed by a plenum chamber with or without plenum pumping, and nonlinear accounting for dynamic pressure effects of slot outflow and ingestion of low energy air in regions of slot inflow. Observations made during development and limited application of the simulation have led to the following summary remarks regarding (1) simulation accuracy, (2) clarific@ of phenomena, and (3) recommendations for use of the simulation.

1. Checks of simulation performance against the principle of mass conservation and predictions from classical slotted-wall theory showed that both solid wall and slot flux boundary conditions formulated in terms of velocity potential are clearly superior to those formulated in terms of a velocity component.

2a. Simulating the slotted wall with discrete slots allows the slot perturbations in the tunnel interior flow to be separated quantitatively from

those flow phenomena occurring within each slot and its extension into the plenum chamber. The log cosecant function of the slot width-to-spacing ratio which appears explicitly in most of the theoretically derived expressions of the equivalent homogeneous slotted wall boundary condition expresses only the tunnel interior flow perturbation effect.

2b. Representation of the finite length of tunnel wall slots invokes a characteristic mode of tunnel flow, the magnitude of which is suppressed to zero for infinite length slots. This mode provides an exponential distribution between unequal static pressure at the upstream and downstream ends of the slotted region and requires that the plenum pressure be very close to the upstream static pressure unless the slots are very short.

2c. Inclusion in the simulation of two nonlinear features of slot flow behavior alters the distribution of wall-induced longitudinal velocity due to model blockage and introduces a significant longitudinal component of the wall-induced velocity due to model lift.

3a. The limited range of parametric variations illustrated herein should be extended to a broad parametric study including simple forms of variable geometry coupled with monitoring of wall pressure near the downstream end of the slots to improve the design and/or use of slotted test sections.

3b. In incorporating the present simulation into a procedure for interference assessment, local values of the slot boundary condition parameter probably do not constitute an effective primary set of variables for matching measured wall pressures. Furthermore, both the set of variable parameters and the set of measured pressure locations should include members appropriate for establishing both the tunnel/plenum interaction mode and the effective capture area at the downstream slot end.

ACKNOWLEDGEMENT

The author is grateful to the NASA Langley Research Center for its support under Cooperative Agreement NCC1-69 for the work reported herein.

APPENDIX A
IMPROVED STORAGE OF AERODYNAMIC INFLUENCE COEFFICIENTS

The high order panel method program used as the basis for the present simulation provides for singularity distributions in each panel with orders as high as biquadratic for doublet singularities and bilinear for source singularities. Six singularity distribution coefficients are required to quantify the biquadratic distributions and three coefficients for bilinear distributions. For a panel with combined high order source and doublet loading, the elemental aerodynamic influence coefficients relating the panel to a single control point consist of the potential and three components of velocity induced at the control point by each of the nine singularity distribution modes, a total of 36 influence coefficients. The total number of such influence coefficients in a problem sized for a system of 600 linear equations could reach the order of 10^7 in the most complex case. In the panel method program, the array of influence coefficients is first calculated (by the procedures of ref. 14) and stored, then is accessed to build up the matrix of boundary condition coefficients, and is accessed again to interpret the solution. The CDC CYBER 203 computer used during development of the present simulation had a core memory size available to the user of less than 10^6. The computer resources required, therefore, for storing and accessing this one array were significant.

A procedure for more efficient handling of the influence coefficients was developed during the present study. The basic panel method procedure involves expressing each singularity distribution coefficient on a panel as a linear combination of the singularity strengths at singularity points on a cluster of neighboring panels within a common network of panels. The combining coefficients are calculated by a weighted least squares fitting process which is dependent only on the geometry of panels and singularity points within each panel network. (For biquadratic doublet panels, the fitting process used is the minimized doublet discontinuity approach of ref. 15.) Boundary conditions are imposed at control points located identically with the simgularity points so that the boundary condition coefficients form a square matrix relating the set of boundary conditions to the set of unknown singularity strengths at the singularity points. Each element of the square matrix is then the accumulation of the products of elemental aerodynamic influence coefficients with singularity fit coefficients summed over all panels whose singularity distribution is linked in the fitting process to the local singularity strength. Singularity points (and control points) are located in general at the panel centers. In networks of panels with biquadratic doublet distributions, additional points are located along the network edges and corners.

In the improved procedure, the elemental aerodynamic influence coefficients are calculated for each panel and immediately combined with the set of singularity fit coefficients for that panel and the products distributed over the appropriate storage locations so that when the process is completed, the combined influence coefficients relating one singularity point to a single control point consist of the four aerodynamic quantities induced

by each of the two singularity types, source and doublet. Thus, a maximum of eight storage locations are required for each singularity point-control point pair. It should be noted that in the typical tunnel test section simulation as discussed in this paper, almost all simgularity points are in networks with either source or doublet singularities but not both. For each such singularity point, only four storage locations per control point are required.

The following table shows a comparison of the array size required for influence coefficient storage in the original elemental form and the new combined form for problems having 600 unknowns distributed over four equal size networks having source only, doublet only, and combined source and doublet singularities in all networks.

Singularity type	Elemental influence coefficients	Combined influence coefficients
Source only	4.32×10^6	1.44×10^6
Doublet only	5.99×10^6	1.44×10^6
Source and doublet	8.99×10^6	2.88×10^6

The combined influence coefficients are stored as a sequence of vectors in a one-dimensional array using a vector length equal to the total number of control points plus slot origin points. Thus, the length of that portion of the array actually used is minimized regardless of the problem size.

In addition to the benefits of reduced array size, further reduction in computer resource requirements was achieved by calculating, combining, and accumulating in storage the influence coefficients for one network, and then retreiving these coefficients to fill the portion of the boundary condition coefficient matrix associated with that network before proceeding to the next network. If the portion of the influence coefficient storage array associated with that network is small enough to reside completely in central memory along with the other data needed to perform the above operations, then the number of times that that portion of the array is passed through central memory is reduced from three to two.

APPENDIX B
PANEL SOURCE DISTRIBUTION IN SLOTTED WALL NETWORKS

Homogeneous Wall

A bilinear source panel network with some special properties is used in conjunction with a biquadratic doublet network to model the homogeneous slotted wall. The homogeneous wall boundary condition to be imposed at all panel centers is given by eqn. (2). The imposition of the unperturbed outer flow condition at coincident doublet panel control points leads to the equivalence between normal velocity at the wall and local source strength. Eqn. (2) implies that the source strength should be zero at the upstream edge of the slotted region. At the downstream edge, the reentry flap modeling requires a row of control points to be placed along the network edge at panel boundary midpoints. The reentry flap boundary condition imposed at these points presumes but does not enforce zero source strength at the downstream edge.

The bilinear singularity fit procedure (see Appendix A) was modified for all panels adjacent to the upstream and downstream network edges by including a phantom singularity point at the midpoint of the panel boundary on the network edge. Although the singularity fit coefficients directly indexed to this point have no subsequent use, the presence of this point in the weighted least squares process alters the other singularity fit coefficients such as to reduce the magnitude of source strength at the network edge. It was found that assigning a weight of 10 to this phantom point (compared with standard weights of 10^6 for the local panel center and unity for all neighboring panel center points) produced a reasonable compromise between zero source strength at the network edge and source continuity at the opposite panel edge.

Discretely Slotted Wall

The special source network used to model a tunnel wall with discrete slots is a flat rectangular network of rectangular panels. Source lines representing the discrete slots are placed coincident with the interior longitudinal panel boundaries. The line source strength is quantified at all interior panel corners and these strengths are members of the set of singularity unknowns for the network. One unknown reentry flap parameter for each slot completes the set of unknowns for the network. The line source strength is zero at the upstream and downstream network edges and varies linearly along each panel boundary. A control point is located on each line source segment at a uniform fraction of the segment length. The optimal value of the fraction is either one half or unity depending on whether the slot boundary condition is expressed in the difference form of eqn. (10) or the integral form of eqn. (6) respectively.

A bilinear source distribution is attributed to each panel. For all panels lying between line sources, a target value of the source sheet strength at each panel corner is related to the line source strength at that corner by

(see eqn. (5))

$$\sigma = -S/2d \tag{B1}$$

Although a bilinear distribution cannot be fitted in general to four corner values, it can be fitted to four values at the panel edge midpoints. The target values at the panel corners, therefore, are averaged in pairs to form the panel edge midpoint values used to express the three bilinear source distribution coefficients as a linear combination of the four line source strengths at the panel corners. The combining coefficients are used subsequently as the singularity fit coefficients described in Appendix A.

For panels lying between a streamwise network edge and the first or last source line, only two target values of panel corner source strength can be determined by eqn. (B1). If the problem is defined on only one side of a plane of symmetry, and one edge of the discrete slot network lies on the plane of symmetry, then the target source strength at each panel corner on the plane of symmetry is set equal to that at the corner adjacent to a line source at the same longitudinal station. Target source strengths at panel corners on the opposite network edge are chosen to satisfy

$$-2\int_0^{\eta_{max}} \sigma d\eta = \Sigma S \tag{B2}$$

where η is the network coordinate normal to the source lines and the integral and summation are performed at a constant longitudinal station across the entire network width. If symmetry is not utilized, the target source strength values at panel corners on the network edges are required to satisfy both eqn. (B2) and

$$-2\int_0^{\eta_{max}} \sigma\eta d\eta = \Sigma S\eta_S \tag{B3}$$

where the values of η_S are η values at the source lines.

APPENDIX C
AERODYNAMIC INFLUENCE OF SOURCE LINE SEGMENTS

Consider a source line segment as shown in the accompanying sketch

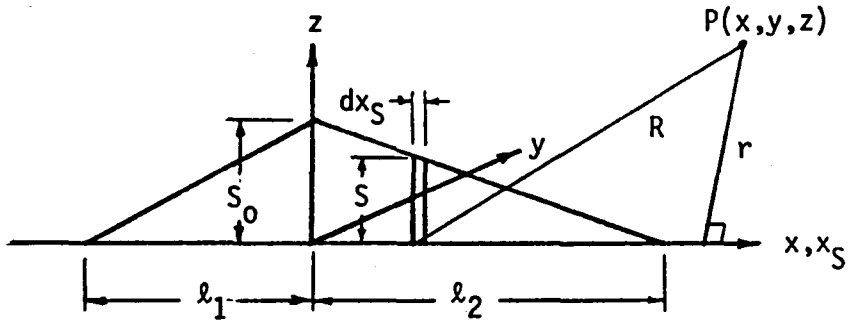

with a source strength distribution given by

$$S(x_S) = \begin{cases} \frac{S_o}{\ell_1}(x_S + \ell_1), & -\ell_1 \le x_S \le 0 \\ \frac{S_o}{\ell_2}(\ell_2 - x_S), & 0 \le x_S \le \ell_2 \end{cases}$$

The potential at the field point $P(x,y,z)$ induced by the elemental source at $x_S,0,0$ is

$$d\phi(x,y,z;x_S) = \frac{-S(x_S)\, dx_S}{4\pi\sqrt{(x-x_S)^2+\beta^2(y^2+z^2)}}$$

Let

$$r = \sqrt{y^2+ z^2}$$

$$R_o = \sqrt{x^2+ \beta^2 r^2}$$

$$R_1 = \sqrt{(x+\ell_1)^2+ \beta^2 r^2}$$

$$R_2 = \sqrt{(x-\ell_2)^2+ \beta^2 r^2}$$

Then

$$\phi = \frac{-S_0}{4\pi}\left[\frac{1}{\ell_1}\int_{-\ell_1}^{0}\frac{(x_s+\ell_1)\,dx_s}{\sqrt{(x-x_s)^2+\beta^2r^2}} + \frac{1}{\ell_2}\int_{0}^{\ell_2}\frac{(\ell_2-x_s)\,dx_s}{\sqrt{(x-x_s)^2+\beta^2r^2}}\right]$$

The result of integration over x_s may be written

$$\phi = \frac{S_0}{4\pi}\left\{\frac{R_1-R_0}{\ell_1} + \frac{R_2-R_0}{\ell_2} + \left(\frac{x+\ell_1}{\ell_1}\right)\ell n\left[R_1-(x+\ell_1)\right] - \left(\frac{x+\ell_1}{\ell_1}+\frac{x-\ell_2}{\ell_2}\right)\ell n(R_0-x) + \frac{x-\ell_2}{\ell_2}\,\ell n\left[R_2-(x-\ell_2)\right]\right\}$$

Differentiating with respect to x or r gives

$$\phi_x = \frac{S_0}{4\pi}\left\{\frac{1}{\ell_1}\ell n\left[R_1-(x+\ell_1)\right] - \left(\frac{1}{\ell_1}+\frac{1}{\ell_2}\right)\ell n(R_0-x) + \frac{1}{\ell_2}\ell n\left[R_2-(x-\ell_2)\right]\right\}$$

$$\phi_r = \frac{S_0\beta r}{4\pi}\left\{\frac{1}{\ell_1\left[R_1-(x+\ell_1)\right]} - \left(\frac{1}{\ell_1}+\frac{1}{\ell_2}\right)\left(\frac{1}{R_0-x}\right) + \frac{1}{\ell_2\left[R_2-(x-\ell_2)\right]}\right\}$$

Note that as $r\to 0$, $R_0\to|x|$, $R_1\to|x+\ell_1|$, $R_2\to|x-\ell_2|$ and the quantities in square brackets in the expressions for ϕ, ϕ_x, and ϕ_r approach zero for all values of x greater than that of the corresponding singular point ($-\ell_1$, 0, or ℓ_2). Thus, the expressions for ϕ, ϕ_x, and ϕ_r are singular at $r = 0$ in the entire range $-\ell_1 \le x < \infty$ but are well behaved at $r = 0$ and $x < -\ell_1$. Although some singularities can be eliminated by evaluating limits as $r\to 0$ for use where $r \ll (\ell_1+\ell_2)$, the above expressions are sensitive to rounding errors even for larger r if $x \gg (\ell_1+\ell_2)$.

The singular behavior at $r = 0$ and $x > \ell_2$ is an artifice of the mathematical formulation because there is no physical reason for the flow around this line source segment to be less well behaved at large positive x than at large negative x. The following formulation avoids this troublesome behavior by using the above expressions only for $x < 0$ and reversing the x-axis sign convention if $x > 0$.

$$k = -\text{sign}(x)$$

$$\phi = \frac{S_o}{4\pi}\left\{\frac{1}{\ell_1}\left[R_1 - R_o + k(x+\ell_1)\ell n\left(\frac{R_1 - k(x+\ell_1)}{R_o - kx}\right)\right]\right.$$

$$\left. + \frac{1}{\ell_2}\left[R_2 - R_o + k(x-\ell_2)\ell n\left(\frac{R_2 - k(x-\ell_2)}{R_o - kx}\right)\right]\right\}$$

$$\phi_x = \frac{S_o k}{4\pi}\left\{\frac{1}{\ell_1}\ell n\left[\frac{R_1 - k(x+\ell_1)}{R_o - kx}\right] + \frac{1}{\ell_2}\ell n\left[\frac{R_2 - k(x-\ell_2)}{R_o - kx}\right]\right\}$$

$$\phi_r = \frac{S_o \beta r}{4\pi}\left\{\frac{1}{\ell_1}\left[\frac{1}{R_1 - k(x+\ell_1)} - \frac{1}{R_o - kx}\right] + \frac{1}{\ell_2}\left[\frac{1}{R_2 - k(x-\ell_2)} - \frac{1}{R_o - kx}\right]\right\}$$

$$\phi_y = \frac{y}{r}\phi_r, \qquad \phi_z = \frac{z}{r}\phi_r$$

Computational singularities are avoided by specifying a small number

$$\varepsilon = (\ell_1 + \ell_2)x10^{-6}$$

and identifying those field points $P(x,y,z)$ for which $r^2 < \varepsilon^2$, setting $\phi_r = 0$ for those points and setting $r^2 = \varepsilon^2$ before evaluating ϕ and ϕ_x.

APPENDIX D
SLENDER BODY REPRESENTATION OF STING AND MODEL BODY

In the method of ref. 6 the model body is represented as a slender body of revolution at zero angle of attack. The perturbation potential at a field point $P(x,y,z)$ is that of a line source having a strength distribution on the body axis at y_b,z_b defined according to slender body principles as equal to the distribution of the gradient A' of the body cross section area A. This potential is given in ref. 6 as

$$\phi^b(x,y,z;y_b,z_b)= \frac{-1}{4\pi} \int_{body} \frac{A'dx_1}{R_b} \qquad (D1)$$

where

$$R_b = \sqrt{(x-x_1)^2+ \beta^2 (y-y_b)^2+ (z-z_b)^2}$$

For numerical computation, the integral in eqn. (D1) was approximated by a Simpson's rule summation of weighted influences of a series of point sources. The equivalent body, therefore, has a stepwise distribution of cross section area.

The present simulation retains the low order singularity distribution equivalent to a stepwise area distribution but provides for both a sting and a model body, both lying in the wind tunnel $y = 0$ plane with otherwise arbitrary inclination and camber. Displacement effects arising from slender body axial flow and crossflow and from a separated wake are represented. In accordance with the concepts of ref. 24, the perturbations due to the axial and crossflow components of the onset flow are assumed to be those arising from source and doublet singularities, respectively. The order of distribution equivalent to a stepwise distribution of cross section area is the series of discrete point sources and of piecewise constant strength line doublets. Unlike the procedure of ref. 24, however, the point source and line doublet strengths are equated to the local increment and magnitude, respectively of body cross section area.

To define the body, an ordered sequence of body station x and z coordinates is specified. Each straight line segment connecting adjacent body stations is taken as the axis of a body element. The element volume and separated flow wake width are specified for each element. In the following discussion, the perturbation potential at the i-th field point P_i due to the j-th line doublet element is first expressed for incompressible flow in terms of the cylindrical coordinate system shown in the accompanying sketch and then subjected to a combined accounting for compressibility by the Goethert rule and transformation to the tunnel cartesian coordinate system. Barred quantities refer to the incompressible domain.

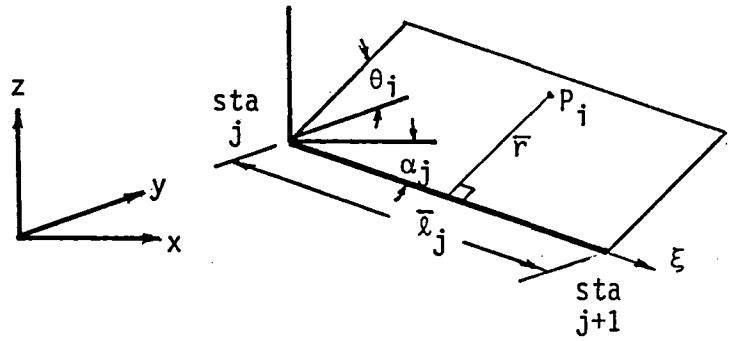

The potential induced by the crossflow doublet line with constant strength $\bar{\mu}_j$ is obtained by integrating eqn. (2.42) of ref. 23 over the length $\bar{\ell}$.

$$\bar{\Phi}^D_{ij} = \frac{\bar{\mu}_j \sin\bar{\theta}_i}{4\pi\bar{r}_i}\left(\frac{\bar{\xi}_i - \bar{\ell}_j}{\sqrt{(\bar{\xi}_i-\bar{\ell}_j)^2+\bar{r}_i^2}} - \frac{\bar{\xi}_i}{\sqrt{\bar{\xi}_i^2+\bar{r}_i^2}}\right) \qquad (D2)$$

In the wind tunnel compressible flow, the j-th body station lies at $(x_j, 0, z_j)$ and the j-th doublet line extends from station j to station $j+1$.

$$\bar{\ell}_j = \sqrt{(x_{j+1}-x_j)^2+\beta^2(z_{j+1}-z_j)^2}$$

$$\sin\bar{\alpha}_j = \frac{-\beta(z_{j+1}-z_j)}{\bar{\ell}_j} \qquad \cos\bar{\alpha}_j = \frac{x_{j+1}-x_j}{\bar{\ell}_j}$$

At $P(x_i, y_i, z_i)$,

$$\bar{\xi}_i = (x_i-x_j)\cos\bar{\alpha}_j - \beta(z_i-z_j)\sin\bar{\alpha}_j$$

$$\bar{\xi}_i-\bar{\ell}_j = (x_i-x_{j+1})\cos\bar{\alpha}_j - \beta(z_i-z_{j+1})\sin\bar{\alpha}_j$$

$$\bar{r}_i^2 = (x_i-x_j)^2\sin^2\bar{\alpha}_j + 2\beta(x_i-x_j)(z_i-z_j)\sin\bar{\alpha}_j\cos\bar{\alpha}_j + \beta^2[y_i^2+(z_i-z_j)^2\cos^2\bar{\alpha}_j]$$

$$\sin\bar{\theta}_i = [(x_i-x_j)\sin\bar{\alpha}_j + \beta(z_i-z_j)\cos\bar{\alpha}_j]/\bar{r}_i$$

Now, express the cross section area in terms of the element volume V as

$$\bar{A}_j = \frac{\beta^2 V_j}{\bar{\ell}_j}$$

then,

$$\bar{\mu}_j = \frac{2\beta^2 V_j \sin \bar{\alpha}_j}{\bar{\ell}_j} \tag{D3}$$

and the source strength at station j is

$$\bar{S}_j = \bar{A}_j \cos \bar{\alpha}_j - \bar{A}_{j-1} \cos \bar{\alpha}_{j-1} + \beta^2 w_j (z_j - z_{j-1}) \tag{D4}$$

where w_j is the separated wake width prescribed for element j. Then

$$\phi_i = \sum_{j=1}^{NS} \phi_{ij}^S + \sum_{j=1}^{NS-1} \phi_{ij}^D \tag{D5}$$

where

$$\phi_{ij}^D = \frac{1}{\beta^2} \bar{\phi}_{ij}^D$$

$$\phi_{ij}^S = \frac{1}{4\pi\beta^2} \frac{\bar{S}_j}{\sqrt{(x_i - x_j)^2 + \beta^2 [y_i^2 + (z_i - z_j)^2]}} \tag{D6}$$

and NS is the number of body stations.
The source series $\bar{S}_j$ requires special treatment at the end points. At $j=1$, the $\bar{A}_{j-1} \cos \bar{\alpha}_{j-1}$ must be omitted. At $j=NS$, $\bar{A}_j \cos \bar{\alpha}_j$ must be omitted to simulate an unseparated body base flow. Alternatively, provision is made to simulate a blunt base wake by omitting both of the $\bar{A}\cos\bar{\alpha}$ terms from $\bar{S}_{NS}$. The three velocity components at point P are formulated by differentiating eqn. (D5) with respect to x_i, y_i, or z_i.

The sting is simulated by a formulation identical to that of the body except that provision is made to omit the source at the initial sting station $\bar{S}_1$ to represent a sting emerging from a blunt body base.

APPENDIX E
WING THICKNESS AND LIFT REPRESENTATION

The procedure used in this simulation to determine the perturbation at a field point $P(x,y,z)$ due to the distribution of wing thickness over the wing planform is essentially the same as that described in ref. 6 except that the present procedure does not require the wing thickness to go to zero at the trailing edge. Instead, a finite trailing edge thickness is permitted so that the wake blockage associated with a wing wake springing from the trailing edge along the entire span may be simulated. In the case of lift distribution, the procedure used herein is identical with that described of ref. 6 but the formulation will be repeated herein for completeness.

Using the small perturbation representation of the longitudinal gradient of wing thickness as a local source sheet strength, the perturbation potential due to thickness is

$$\phi^t(x,y,z;x_1,y_1,z_w) = \frac{-1}{4\pi}\int_{-b/2}^{b/2}\int_{x_{LE}}^{x_{TE}} \frac{t_x(x_1,y_1)}{R_w}\,dx_1\,dy_1 \qquad \text{(E1)}$$

where

$$R_w = \sqrt{(x-x_1)^2+\beta^2[(y-y_1)^2+(z-z_w)^2]}$$

and t_x is the local source strength within the wing planform lying in the $z = z_w$ plane. Now, let $x_w(y_1)$ be the locus of wing mid-chord points, and

$$X = x - x_w(y_1)$$

$$X_1 = x_1 - x_w(y_1)$$

$$R = \sqrt{X^2+\beta^2[(y-y_1)^2+(z-z_w)^2]} = R(x,y,z;y_1,z_w)$$

The chordwise integration of eqn. (E1) is simplified by expanding $1/R_w$ in terms of the binomial series

$$\frac{1}{R_w} = \frac{1}{R}\left(1 - \frac{1}{2}\mu + \frac{3}{8}\mu^2 - \frac{5}{16}\mu^3 + \ldots.\right) \qquad \text{(E2)}$$

where

$$\mu = \frac{X_1^2 - 2XX_1}{R^2}$$

In the far field, $\mu \ll 1$ and the first few terms of the series provide a

good approximation to R_w. By using eqn. (E2) and performing the chordwise integration of eqn. (E1)

$$\phi^t = \frac{-1}{4\pi}\int_{-b/2}^{b/2}\left\{\frac{\Lambda_0}{R}+\frac{\Lambda_1}{R^2}\left(\frac{X}{R}\right)+\tfrac{1}{2}\frac{\Lambda_2}{R^3}\left[3\left(\frac{X}{R}\right)^2-1\right]+\tfrac{1}{2}\frac{\Lambda_3}{R^4}\left(\frac{X}{R}\right)\left[5\left(\frac{X}{R}\right)^2-3\right]+O(\varepsilon^5)\right\}dy_1 \tag{E3}$$

where

$$\varepsilon = |X_1/R|_{max}$$

and

$$\Lambda_n(y_1) = \int_{x_{LE}}^{x_{TE}} t_x(x_1 - x_w)^n dx_1 \tag{E4}$$

To relate this formulation to that of ref. 6, eqn. (E4) is integrated by parts for $n = 0,1,2,3$ yielding

$$\Lambda_0 = t_{TE}$$

$$\Lambda_1 = t_{TE}\left(\frac{c}{2}\right) - \int_{x_{LE}}^{x_{TE}} t\,dx_1$$

$$\Lambda_2 = t_{TE}\left(\frac{c}{2}\right)^2 - 2\int_{x_{LE}}^{x_{TE}} t(x_1 - x_w)dx_1$$

$$\Lambda_3 = t_{TE}\left(\frac{c}{2}\right)^3 - 3\int_{x_{LE}}^{x_{TE}} t(x_1 - x_w)^2 dx_1$$

where c is the local chord $(x_{TE}-x_{LE})$. The integrals $\int_{x_{LE}}^{x_{TE}} t(x_1-x_w)^n dx_1$ may be recognized as the T_n of ref. 6.

The potential due to the wing lift distribution is given in ref. 6 as

$$\phi^L(x,y,z;x_1,y_1,z_w) = \frac{1}{4\pi}\int_{-b/2}^{b/2}\int_{x_{LE}}^{x_{TE}} \frac{(z-z_w)\gamma}{(y-y_1)^2+(z-z_w)^2}\left(1+\frac{x-x_1}{R_w}\right)dx_1 dy_1 \tag{E5}$$

where γ is the local bound vorticity. By using the binomial expansion

$$\phi^L = \frac{\beta^2}{4\pi}\int_{-b/2}^{b/2} \frac{(z-z_w)}{R}\left\{\frac{\Gamma_o}{R}\left(\frac{1}{1-(X/R)}\right) - \frac{\Gamma_1}{R^2} - \frac{3}{2}\frac{\Gamma_2}{R^3}\left(\frac{X}{R}\right) - \frac{1}{2}\frac{\Gamma_3}{R^4}\left[5\left(\frac{X}{R}\right)^2 - 1\right] + O(\varepsilon^5)\right\} dy_1 \qquad \text{(E6)}$$

where

$$\Gamma_n(y_1) = \int_{x_{LE}}^{x_{TE}} \gamma(x_1 - x_w)^n dx_1$$

Equations for the velocity components are found by differentiating eqns. (E3) and (E6) with respect to x, y, or z. Similar formulations are used to determine the perturbation due to tail thickness and tail lift.

In practice, the Λ_n and Γ_n are established at a discrete set of wing spanwise stations and the integrations with respect to y_1 are performed numerically. In the program implementing the method of ref. 6, the integration made use of Simpson's rule and required, therefore, that the wing stations be uniformly spaced. In the present simulation, this restriction is avoided by using the trapezoidal rule for numerical integration.

REFERENCES

1. Wind-Tunnel Wall-Interference Assessment/Correction-1983. NASA CP-2319, 1984.

2. Kemp, W. B., Jr.; and Adcock, J. B.: Combined Four-Wall Interference Assessment in Two-Dimensional Airfoil Tests. AIAA Jour., vol. 21, no. 10, 1983, pp. 1353-1359.

3. Gumbert, C. R.: User Manual for 0.3-m TCT Wall-Interference Assessment/Correction Procedure: 8- by 24-Inch Airfoil Test Section. NASA TM-87582, 1985.

4. Mokry, M.; Chan, Y. Y.; and Jones D. S.: Two-Dimensional Wind Tunnel Wall Interference. AGARDograph no. 281, Nov. 1983.

5. Mokry, M.: Subsonic Wall Interference Corrections for Finite-Length Test Sections using Boundary Pressure Measurements. AGARD Conference Proceedings no. 335, Paper no. 10, May 1982.

6. Rizk, M. H.; and Smithmeyer, M. G.: Wind Tunnel Wall Interference Corrections for Three-Dimensional Flows. J. Airc., vol. 19, no. 6, 1982, pp. 465-472.

7. Rizk, M. H.; and Murman, E. M.: Wind Tunnel Wall Interference Corrections for Aircraft Models in the Transonic Regime. J. Airc., vol. 21, no. 1, 1984, pp. 54-61.

8. Sedin, Y. C-J.; and Sorensen, H.: Computed and Measured Wall Interference in a Slotted Transonic Test Section. AIAA Paper no. 84-0243, Jan. 1984.

9. Thomas, J. L.; Luckring, J. M.; and Sellers, W. L., III: Evaluation of Factors Determining the Accuracy of Linearized Subsonic Panel Methods. AIAA Paper no. 83-1826, July 1983.

10. Kemp, William B. Jr.: A Slotted Test Section Numerical Model for Interference Assessment. J. Airc., vol. 22, no. 3, 1985, pp. 216-222.

11. Kemp, William B., Jr.: User's Guide to STIPPAN: A Panel Method Program for Slotted Tunnel Interference Prediction. NASA CR-178003, 1986.

12. Davis, D. D., Jr.; and Moore, D.: Analytical Studies of Blockage- and Lift-Interference Corrections for Slotted Tunnels Obtained by the Substitution of an Equivalent Homogeneous Boundary for the Discrete Slots. NACA RM-L53E07b, June 1953.

13. Berndt, S. B.; and Sorensen, H.: Flow Properties of Slotted Walls for Transonic Test Sections. AGARD Conference Proceedings no. 174, Paper no. 17, Oct. 1975.

14. Johnson, Forrester T.: A General Panel Method for the Analysis and Design of Arbitrary Configurations in Incompressible Flows. NASA CR-3079, 1980.

15. Bristow, D. R.; and Grose, G. G.: Modification of the Douglas Neumann Program to Improve the Efficiency of Predicting Component Interference and High Lift Characteristics. NASA CR-3020, 1978.

16. Pindzola, M.; and Lo, C. F.: Boundary Interference at Subsonic Speeds in Wind Tunnels With Ventilated Walls. AEDC TR-69-47, U. S. Air Force, May 1969.

17. Berndt, S. B.: Inviscid Theory of Wall Interference in Slotted Test Sections. AIAA Jour., vol. 15, no.9, 1977, pp. 1278-1287.

18. Barnwell, R. W.: Design and Performance Evaluation of Slotted Walls for Two-Dimensional Wind Tunnels. NASA TM X-78648, Feb. 1978.

19. Steinle, F. W., Jr.; and Pejack, E. R.: Toward an Improved Transonic Wind-Tunnel-Wall Geometry - A Numerical Study. AIAA Paper no. 80-0442, March 1980.

20. Wood, W. W.: Tunnel Interference from Slotted Walls. Quarterly Journal of Mechanics and Applied Mathematics, vol. 17, no. 5, 1964, pp. 126-140.

21. Sewall, William G.: Wall Pressure Measurements for Three-Dimensional Transonic Tests. AIAA Paper no. 84-0599, 1984.

22. Gentry, Garl L., Jr.; Igoe, William B.; and Fuller, Dennis E.: Description of 0.186-Scale Model of High-Speed Duct of National Transonic Facility. NASA TM-81949, 1981.

23. Goethert, Bernhard H.: Transonic Wind Tunnel Testing. Pergamon Press, 1961, pp. 287-292.

24. Shu, Jin-Yea; and Kuhlman, John M.: Calculation of Potential Flow Past Non-Lifting Bodies at Angle of Attack Using Axial and Surface Singularity Methods. NASA CR-166058, 1983.

TABLE I.- NEAR FIELD ACCURACY OF WING THICKNESS AND LIFT SERIES

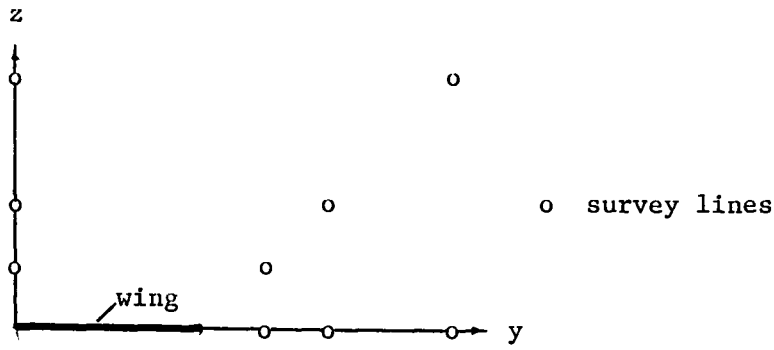

		Thickness series			Lift series		
y/c	z/c	$\lvert C_p \rvert_{max}$	$\lvert \Delta C_p \rvert_{max}$	Relative error	$\lvert C_p \rvert_{max}$	$\lvert \Delta C_p \rvert_{max}$	Relative error
0	1	.020896	.001187	.0568	.166718	.004669	.0280
0	2	.005071	.000065	.0128	.071940	.000769	.0107
0	4	.000947	.000009	.0095	.024802	.000316	.0127
4	0	.005597	.000259	.0463	.002662	.000352	.1322
5	0	.001450	.000009	.0062	.000596	.000043	.0721
7	0	.000333	.000002	.0060	.000109	,000005	.0459
4	1	.003395	.000031	.0091	.019518	.001319	.0676
5	2	.000827	.000005	.0060	.009792	.000332	.0329
7	4	.000176	.000002	.0114	.004299	.000091	.0212

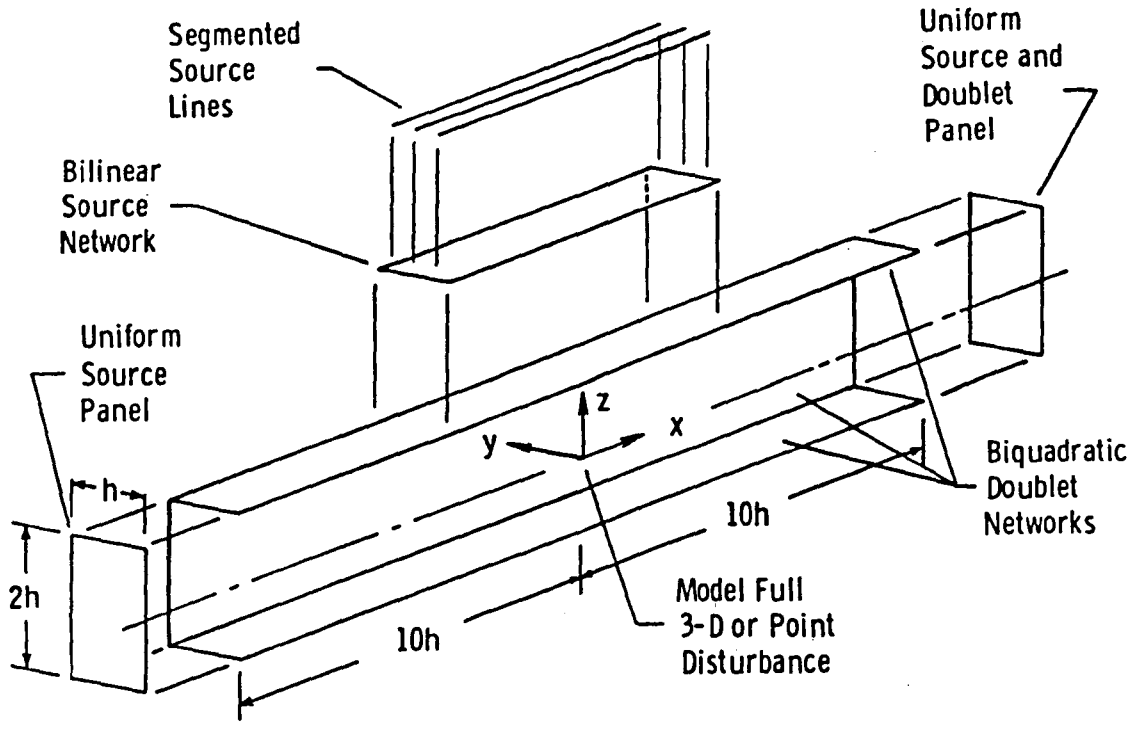

(a) Basic singularities.

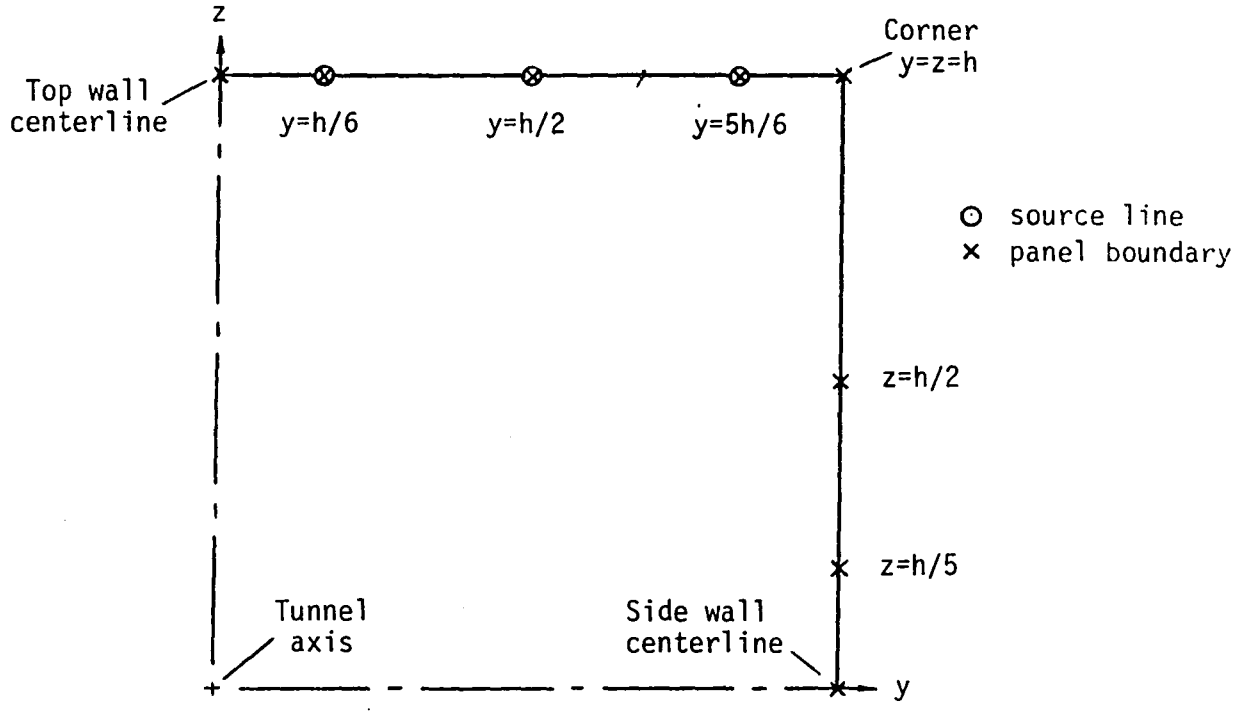

(b) Cross section of upper right quadrant.

Figure 1. - Major features of baseline tunnel simulation.

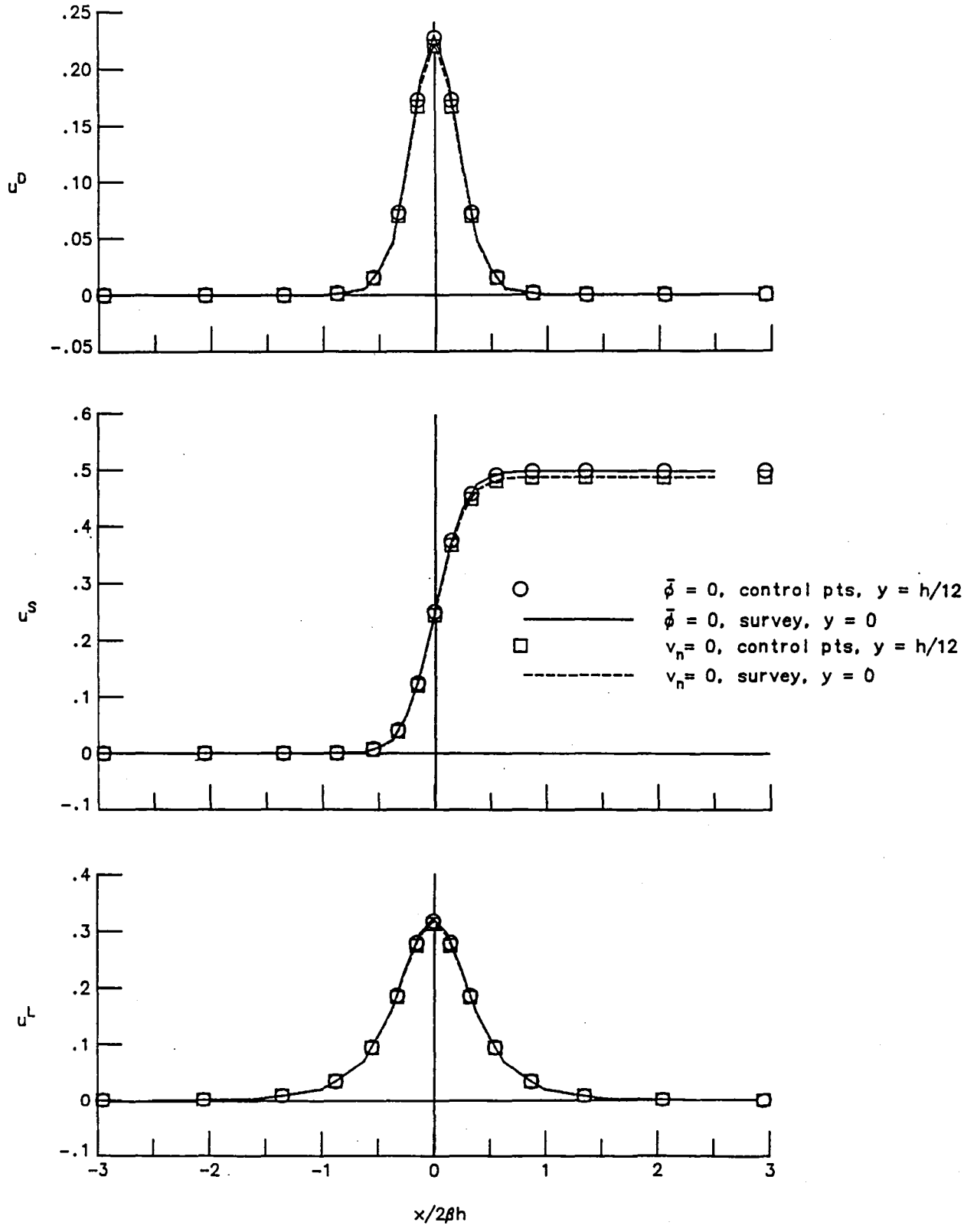

(a) Longitudinal velocity at top wall.

Figure 2. - Simulated flow in a solid wall duct with indirect and direct forms of Neumann boundary condition.

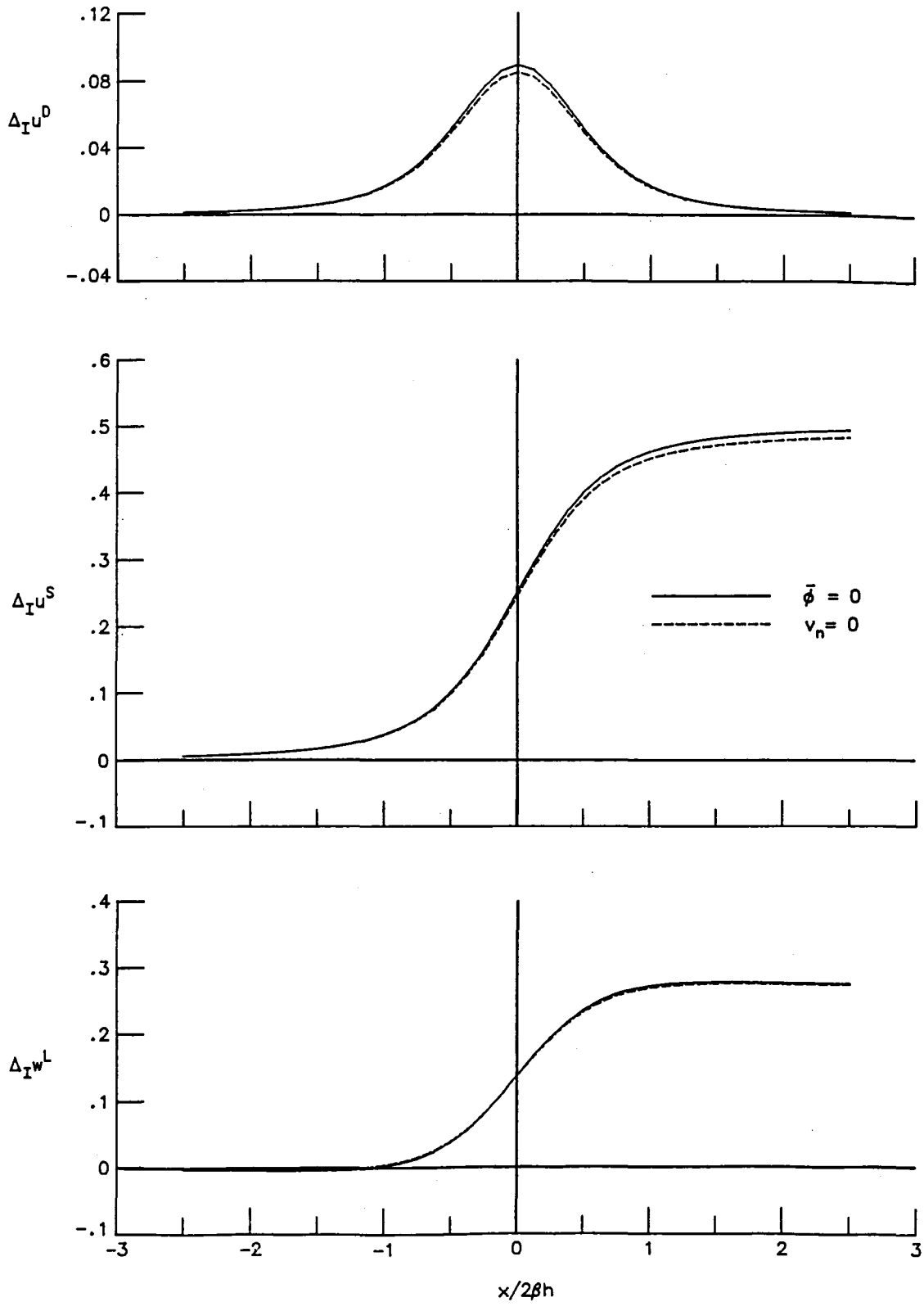

(b) Wall interference velocity on tunnel axis.

Figure 2. - Continued.

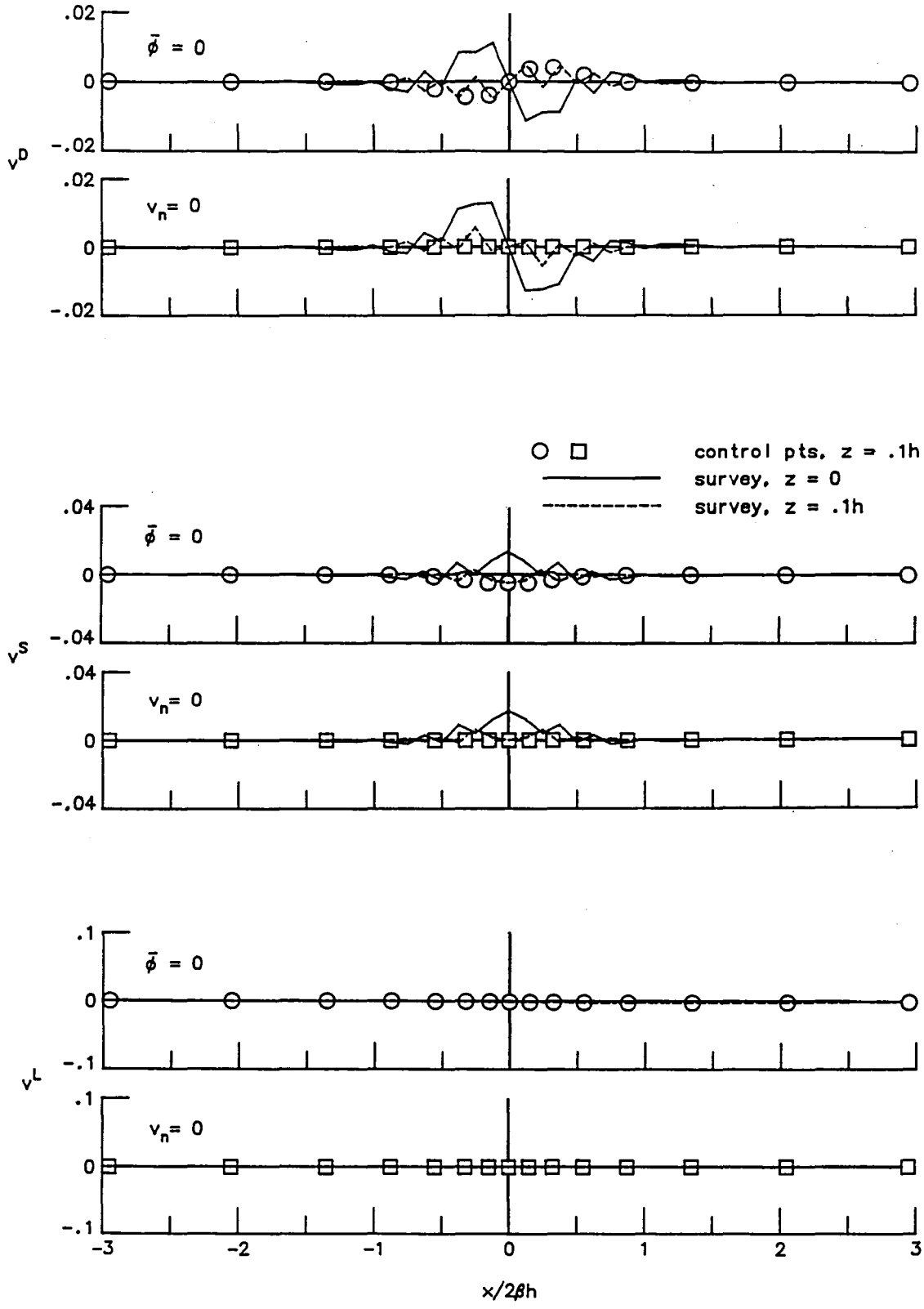

(c) Normal velocity at side wall.

Figure 2. - Continued.

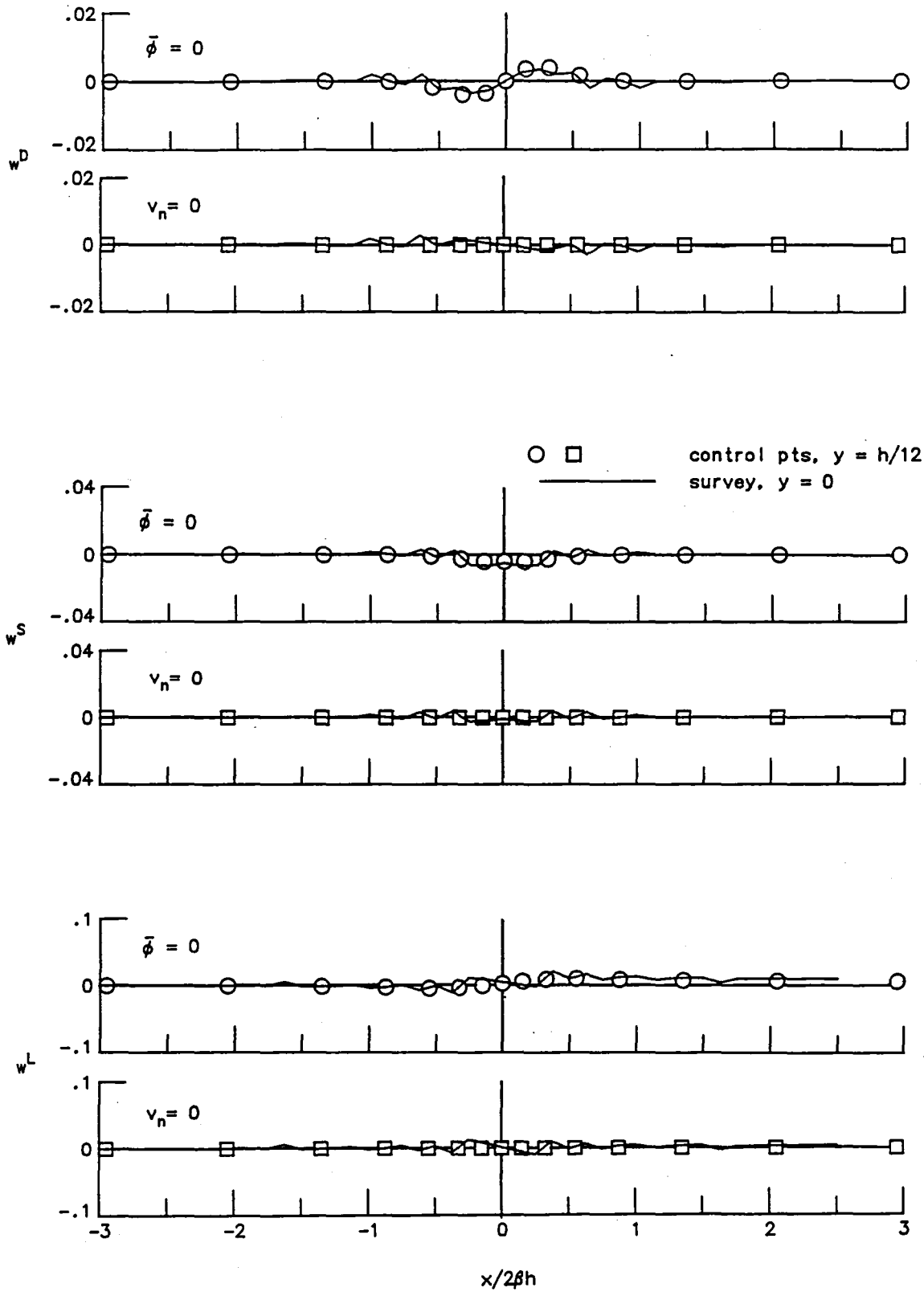

(d) Normal velocity at top wall.

Figure 2. - Concluded.

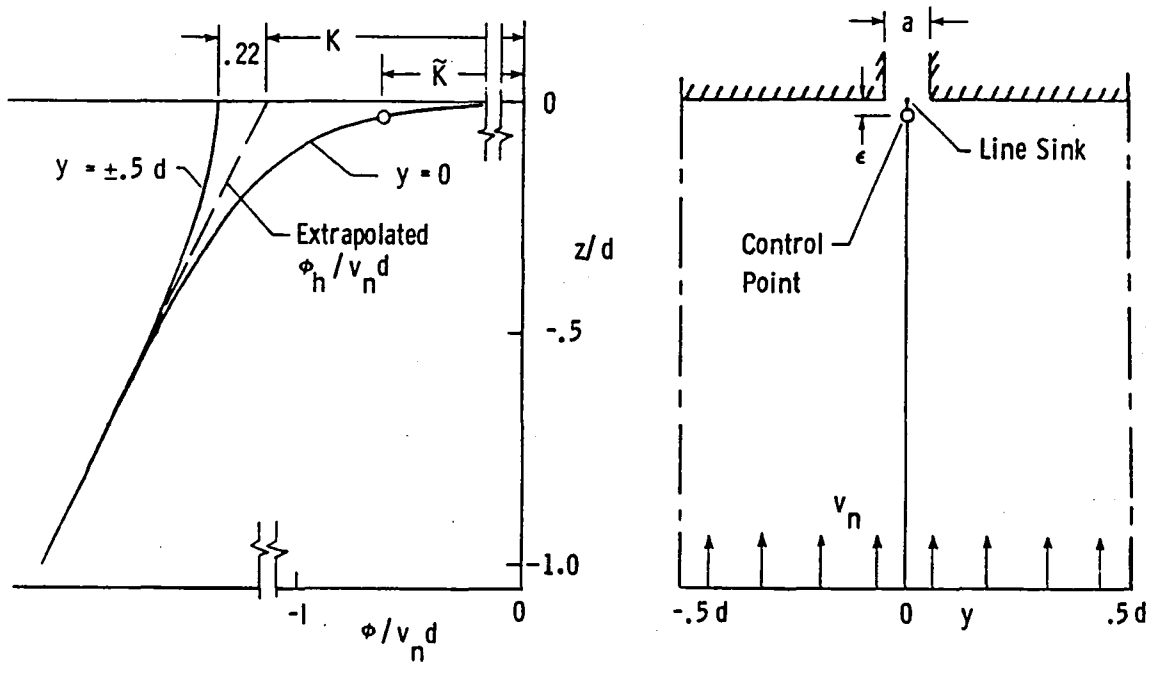

(a) Perturbation potential distribution.

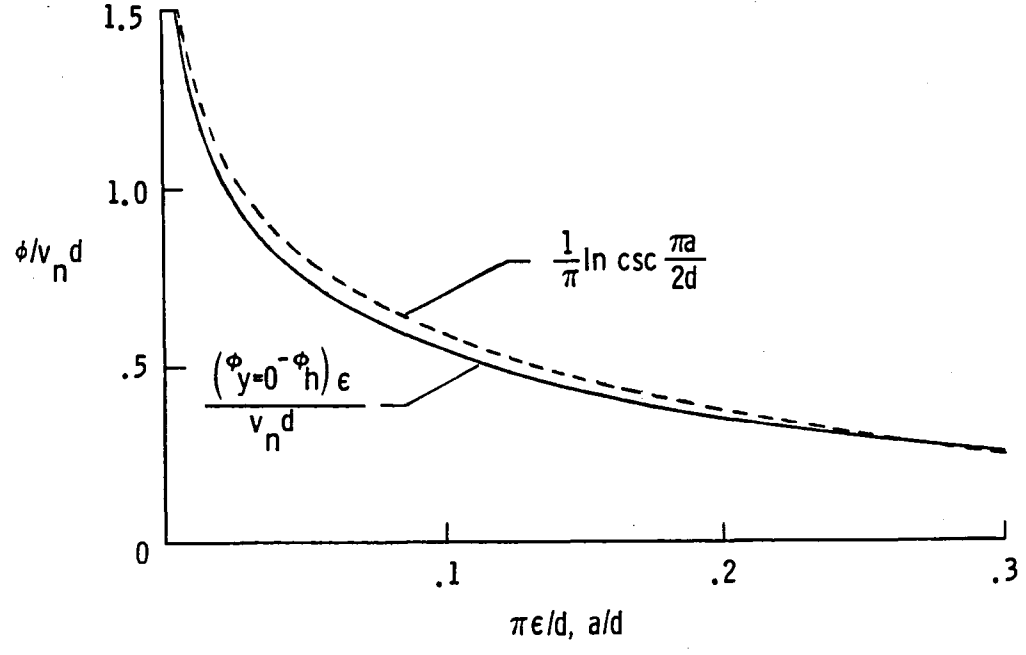

(b) Comparison of discretization potential with theoretical homogeneous wall boundary condition parameter.

Figure 3. - Characteristics of the discrete slot simulation with a uniform crossflow.

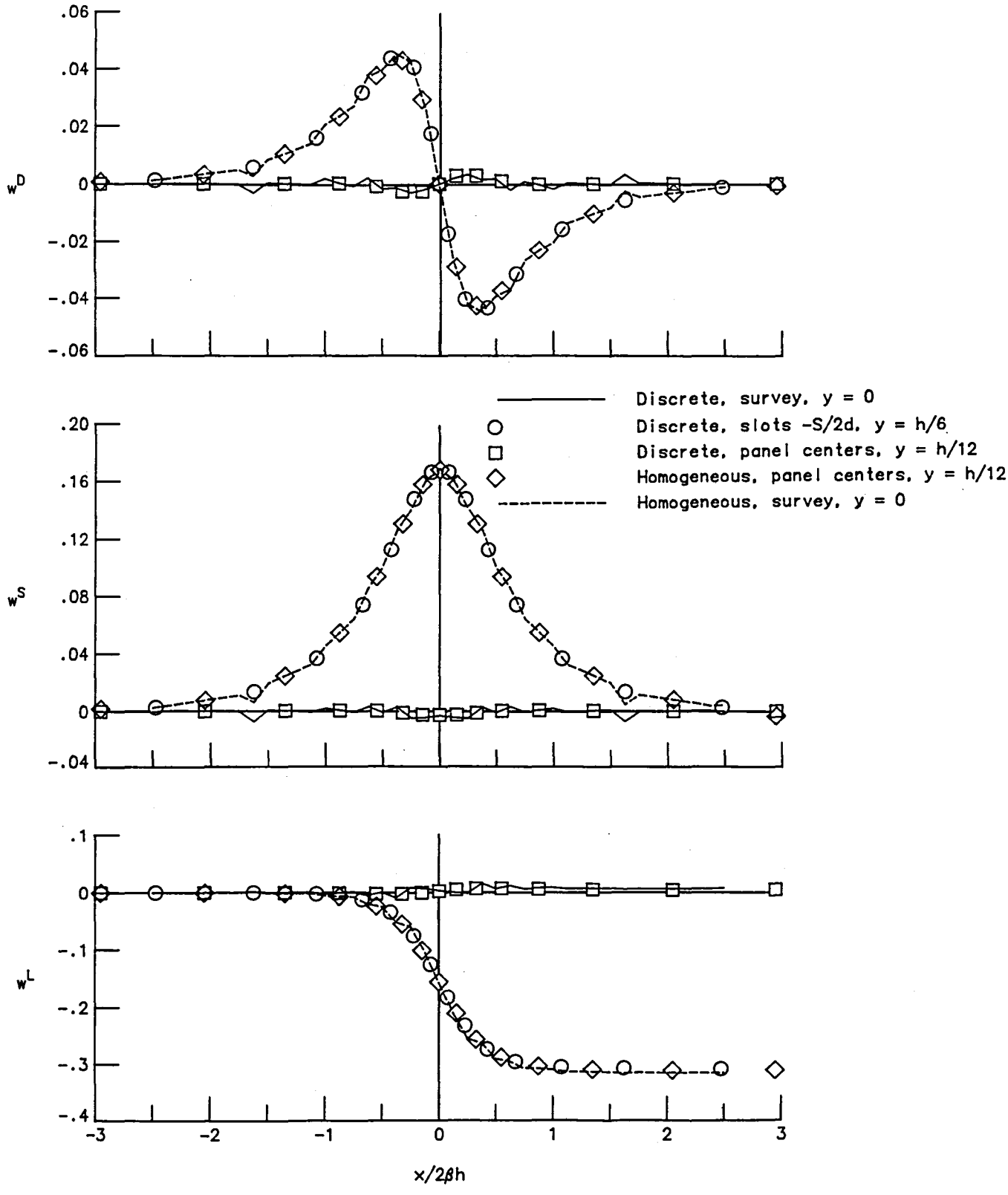

(a) Longitudinal distributions at top wall.

Figure 4. - Discrete slot effects on vertical velocity at walls in baseline tunnel with full length slots.

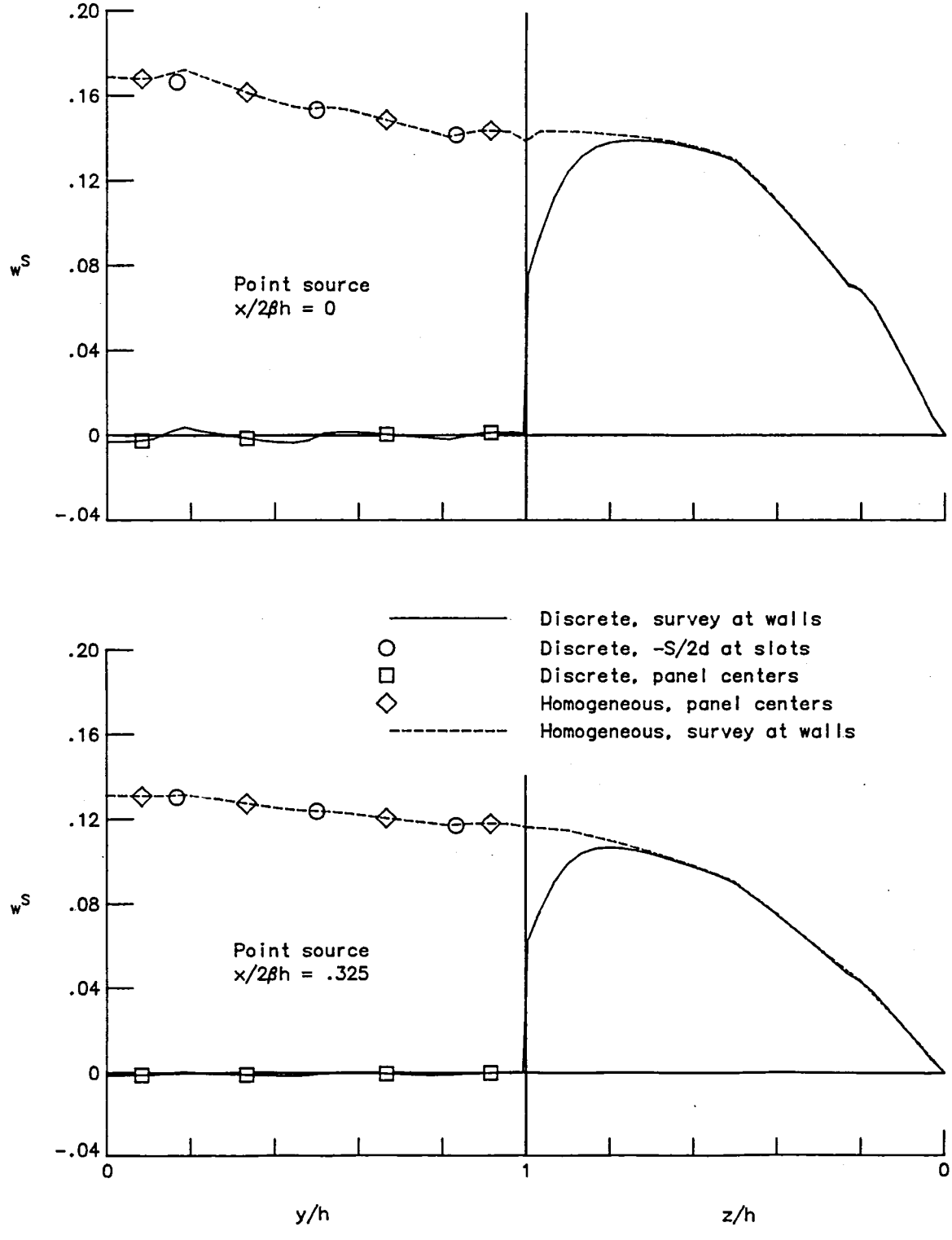

(b) Lateral and vertical distributions with point source disturbance.

Figure 4. - Continued.

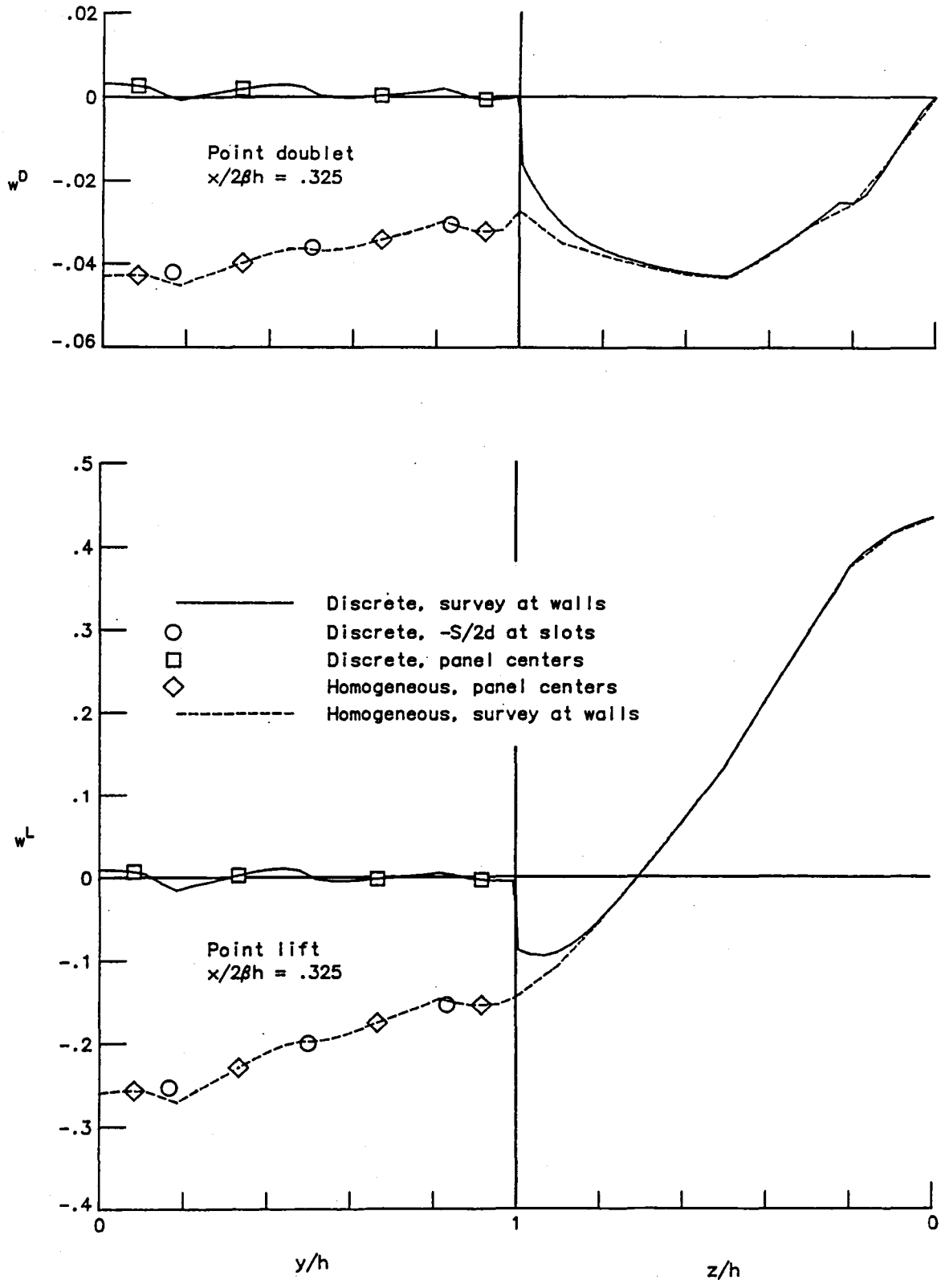

(c) Lateral and vertical distributions with point doublet and lift disturbances.

Figure 4. - Concluded.

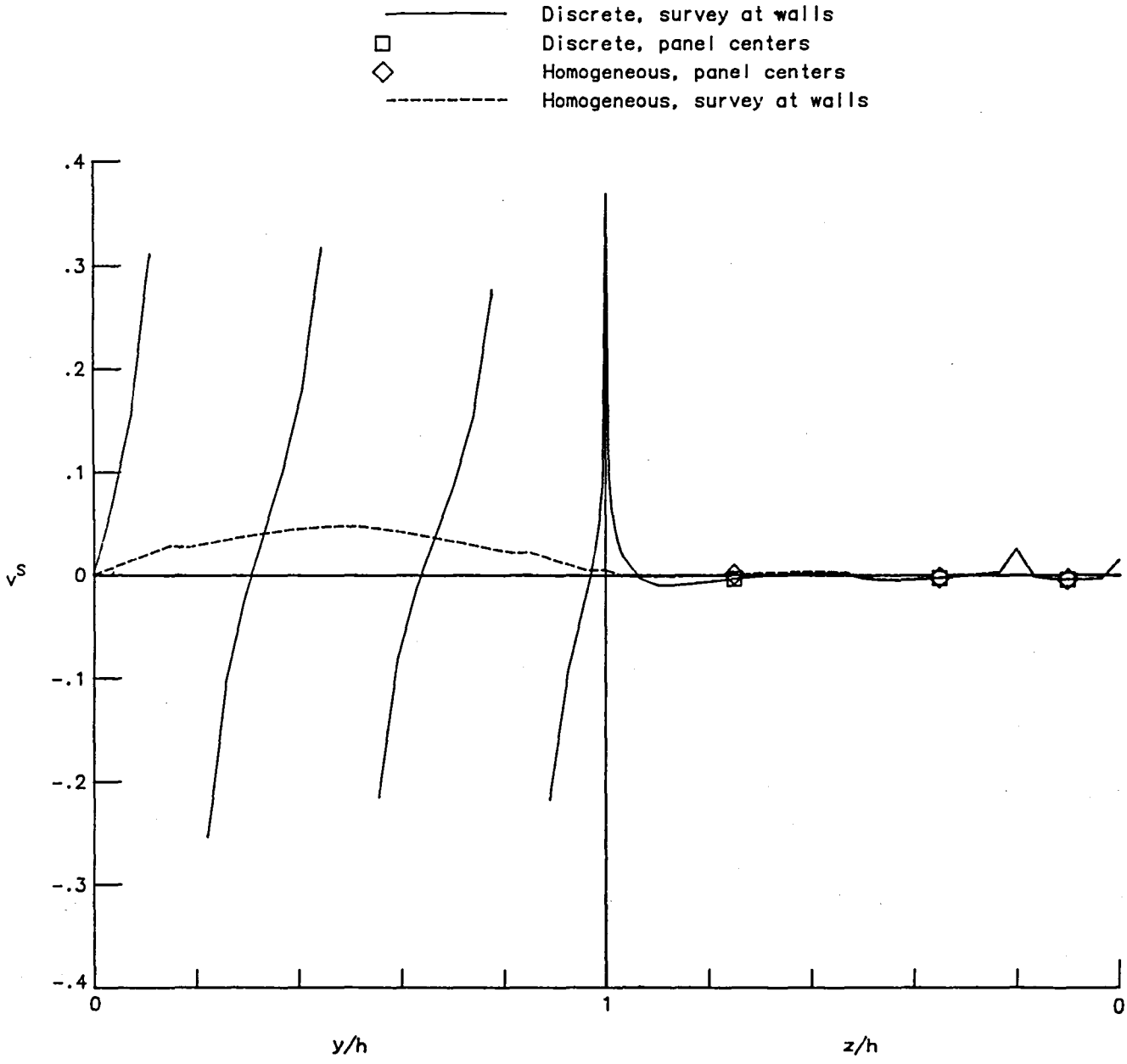

Figure 5. - Discrete slot effects on lateral velocity distribution across top and side walls with point source disturbance, $x/2\beta h = 0$.

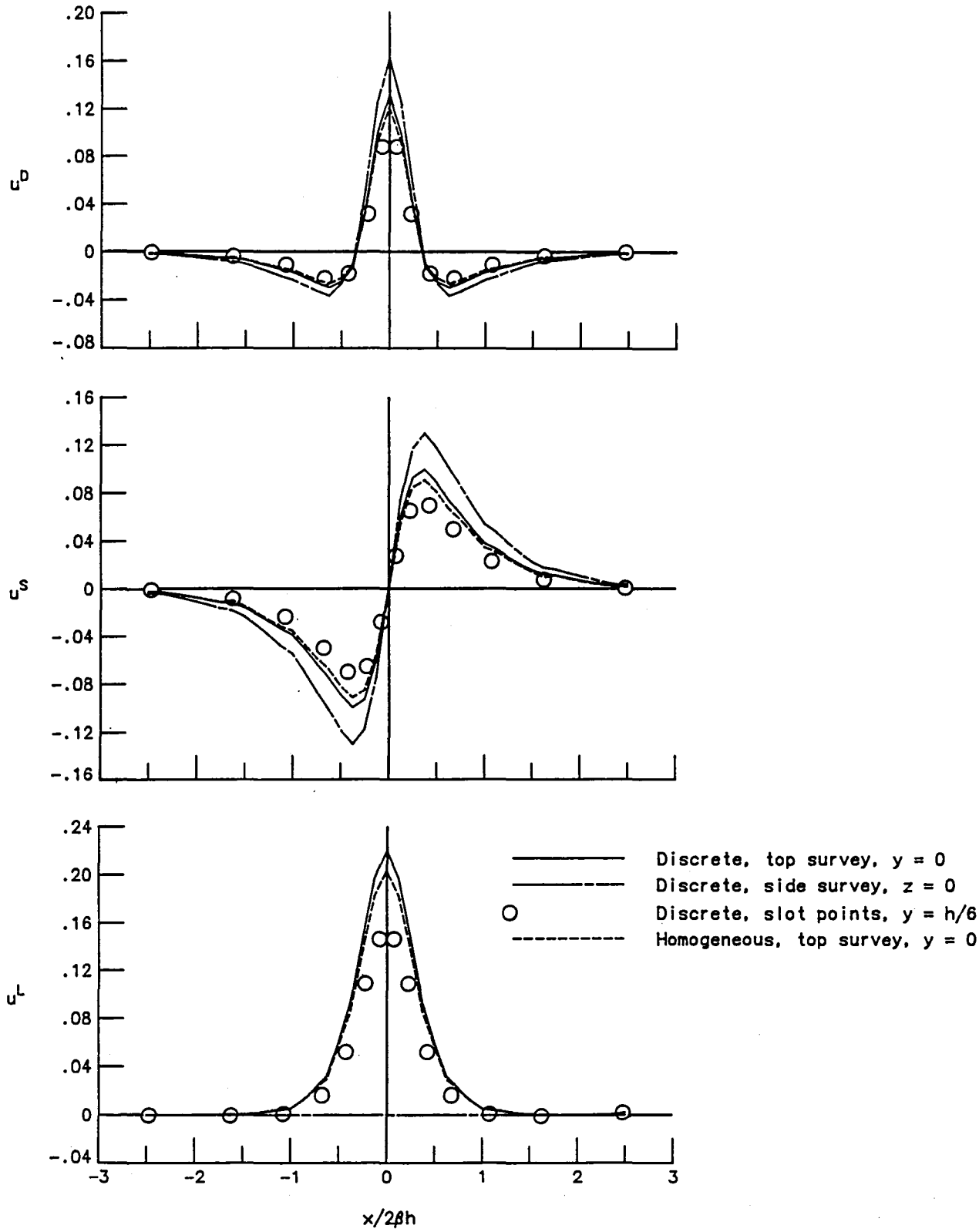

(a) Longitudinal distributions at top wall.

Figure 6. - Discrete slot effects on longitudinal velocity at walls in baseline tunnel with full length slots.

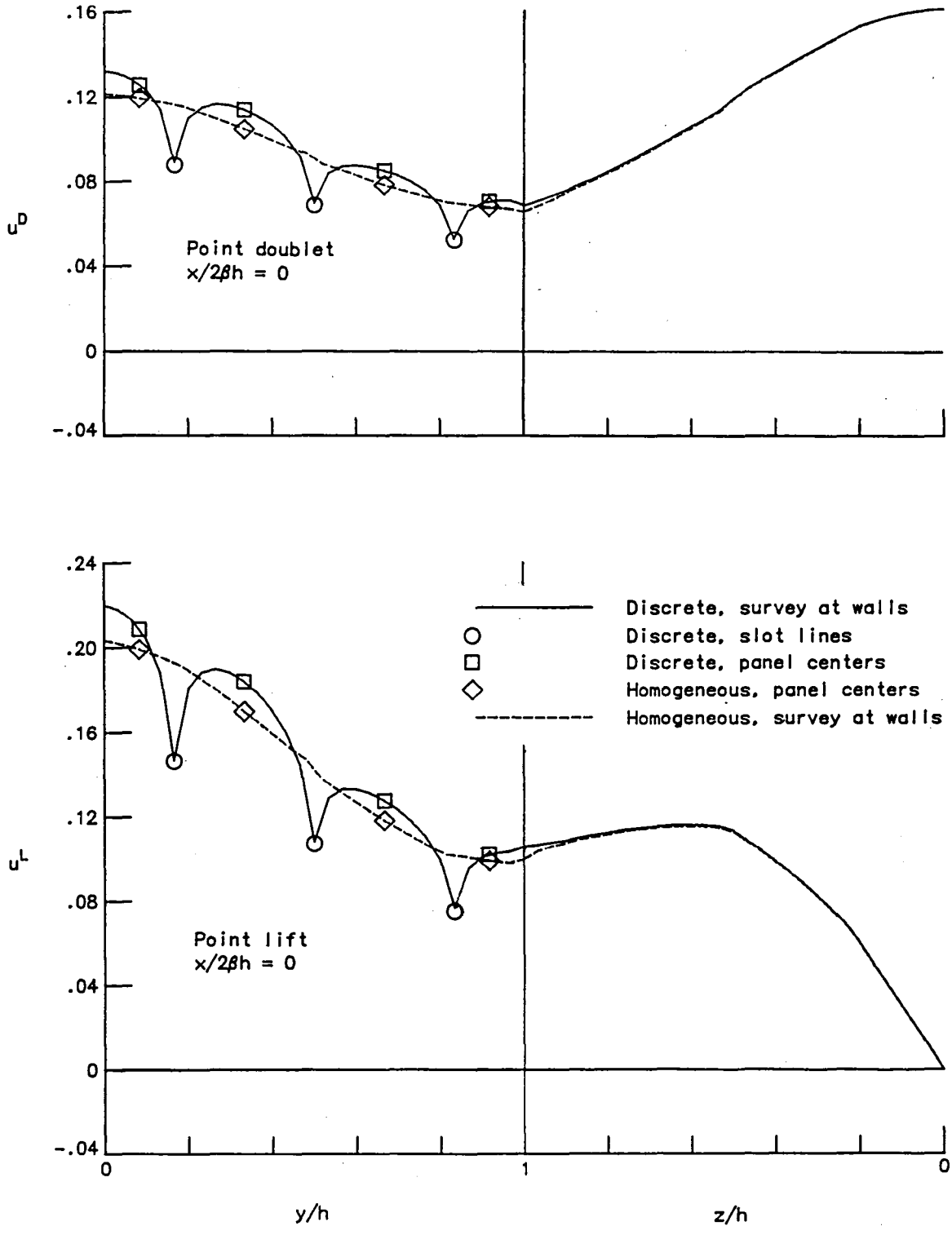

(b) Lateral and vertical distributions with point doublet and lift disturbances.

Figure 6. - Continued.

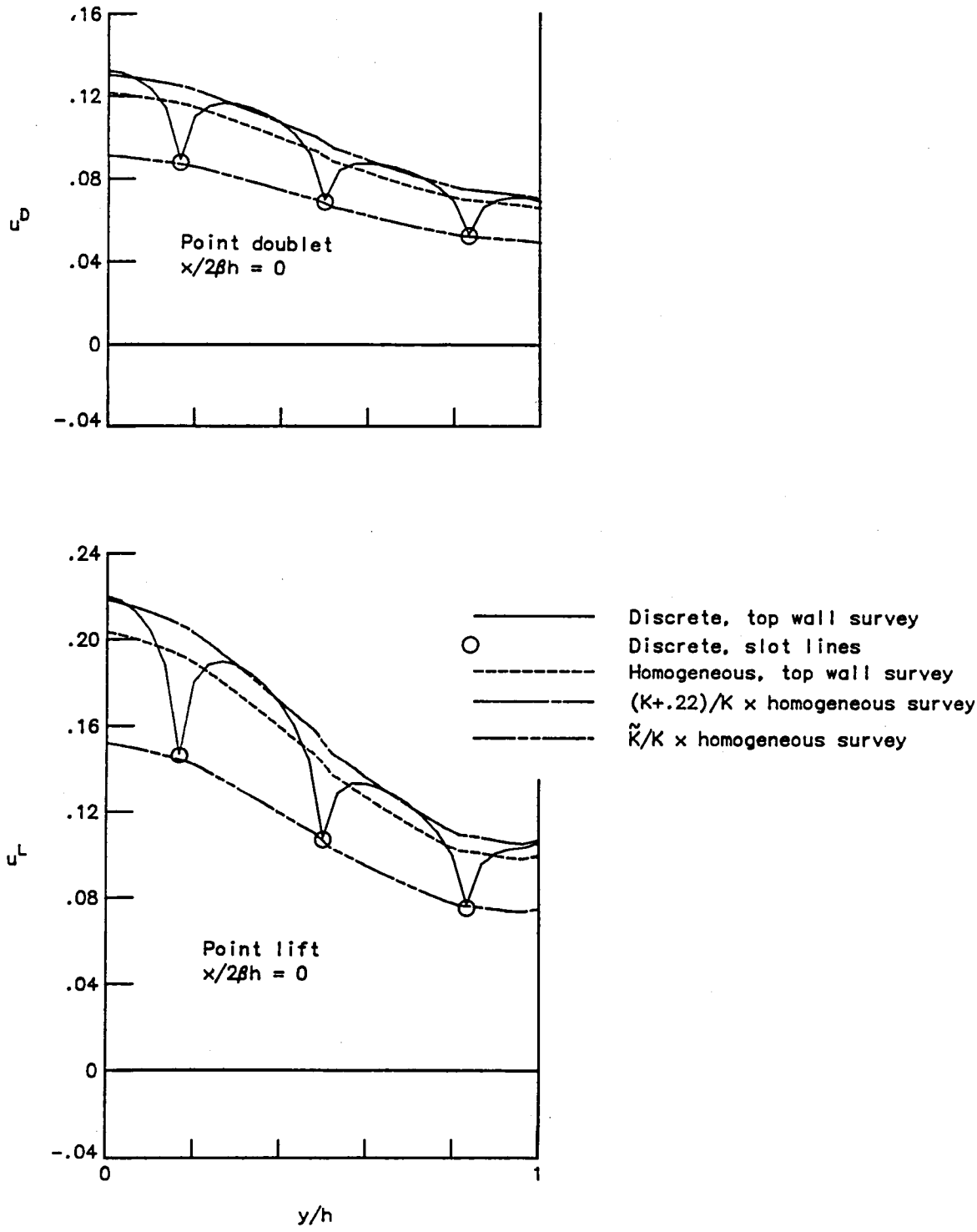

(c) Prediction of cyclic amplitude across discrete slots by use of homogeneous slotted wall parameter K.

Figure 6. - Concluded.

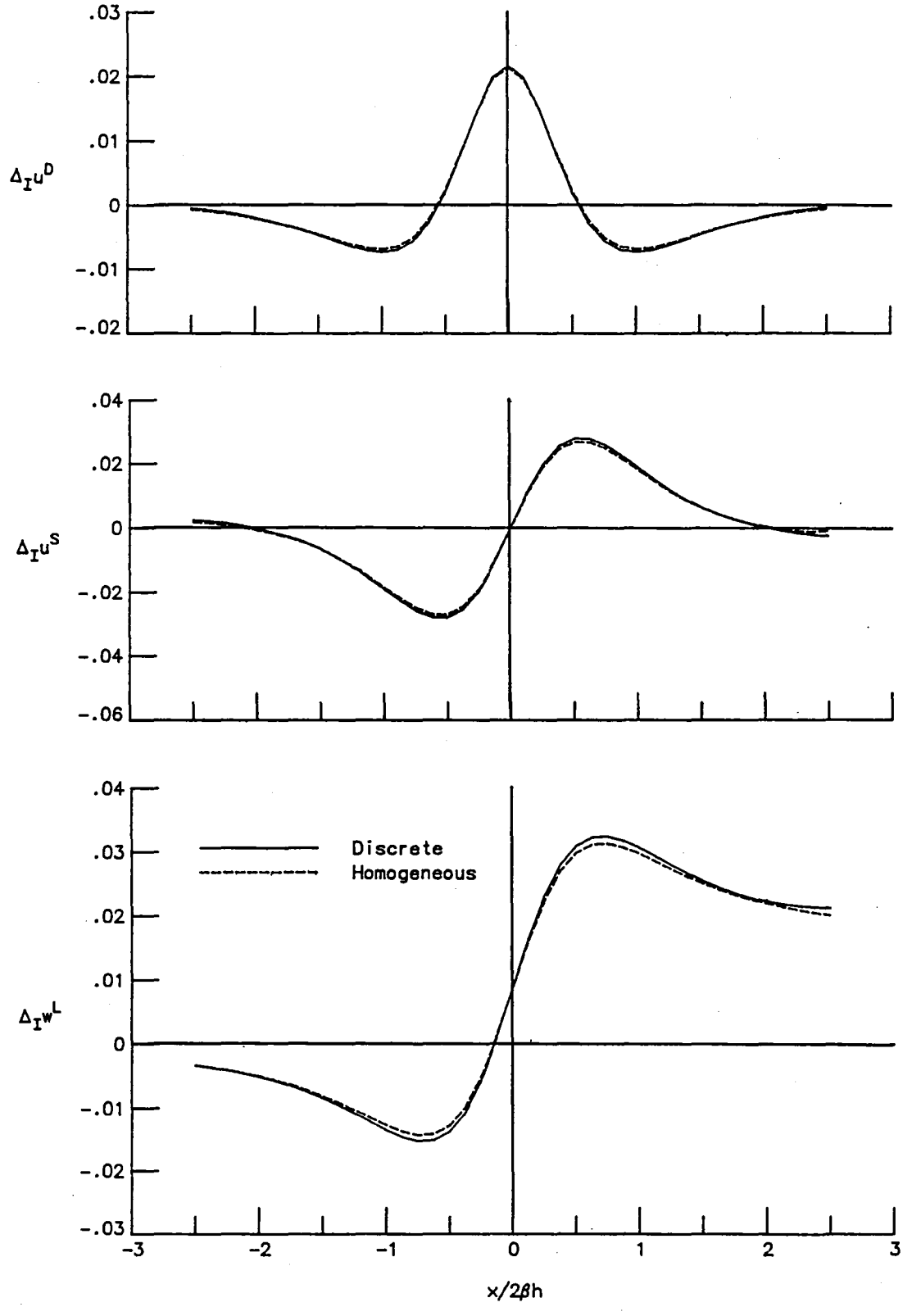

Figure 7. - Discrete slot effects on wall interference velocities at axis of baseline tunnel with full length slots.

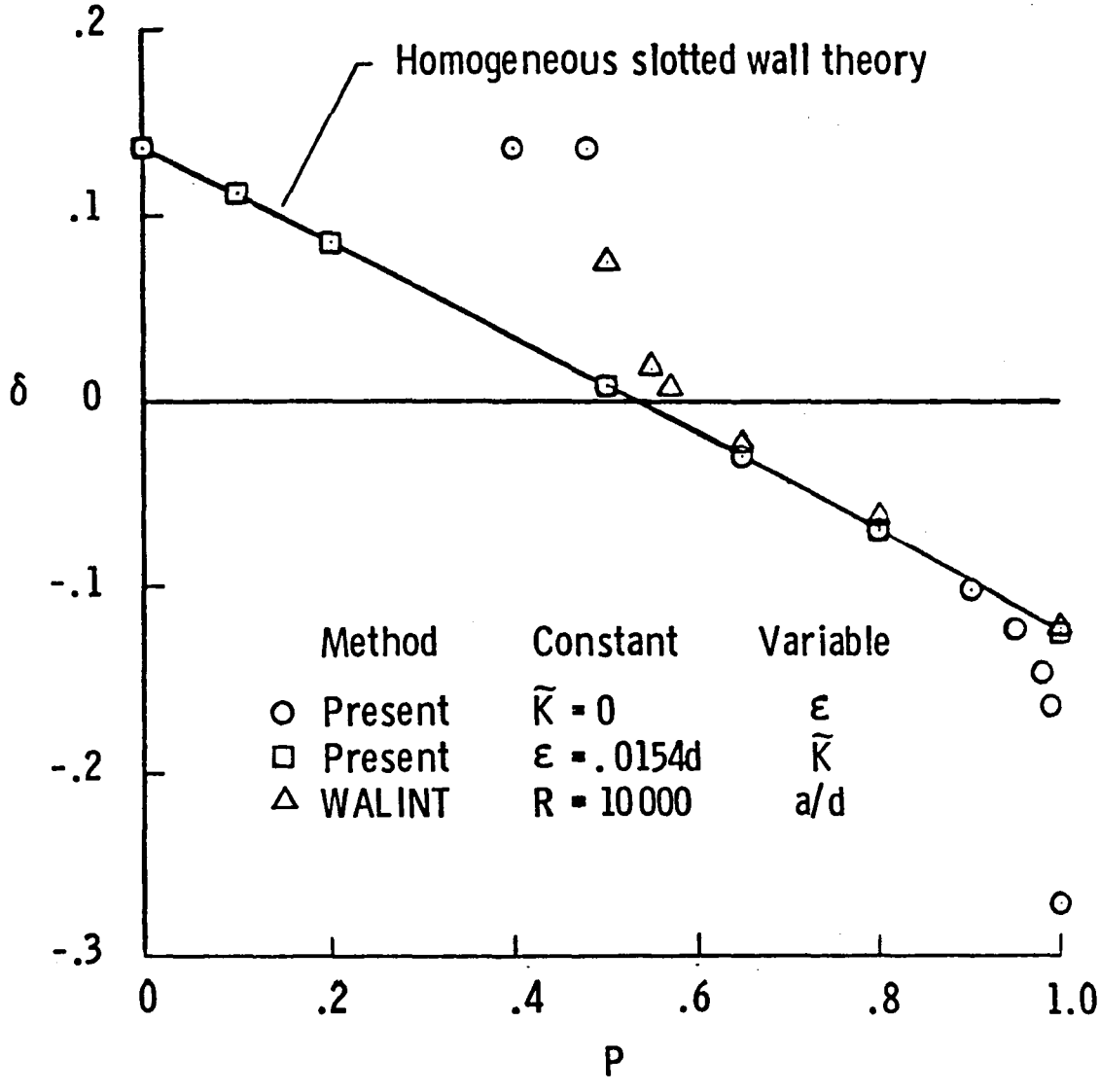

Figure 8. - Comparison of lift interference at model from discrete slot methods with that from homogeneous slotted wall theory for baseline tunnel with full length slots.

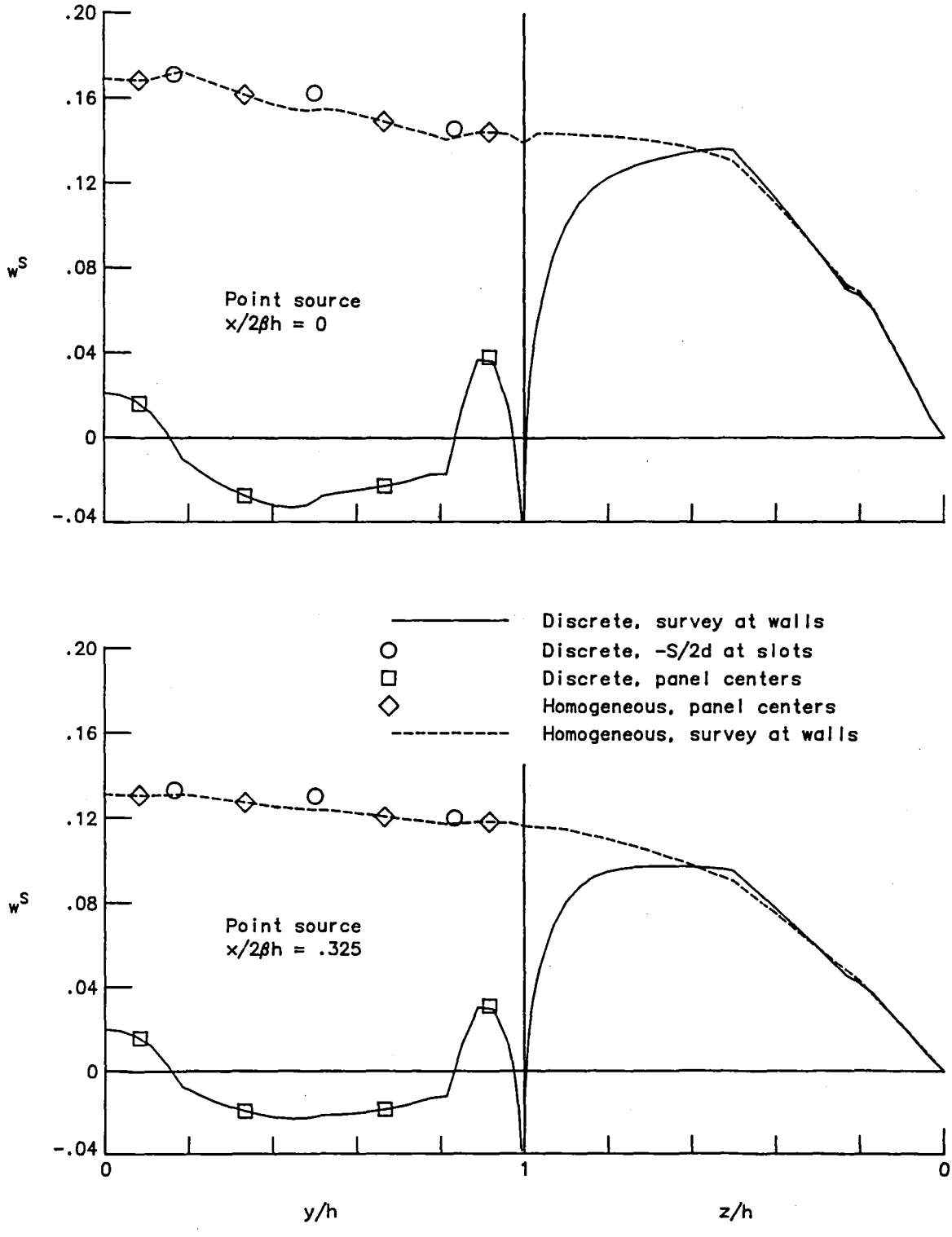

(a) Lateral and vertical distribution of vertical velocity at walls

Figure 9. - Selected discrete slot effects using alternative discrete slot boundary condition in baseline tunnel simulation.

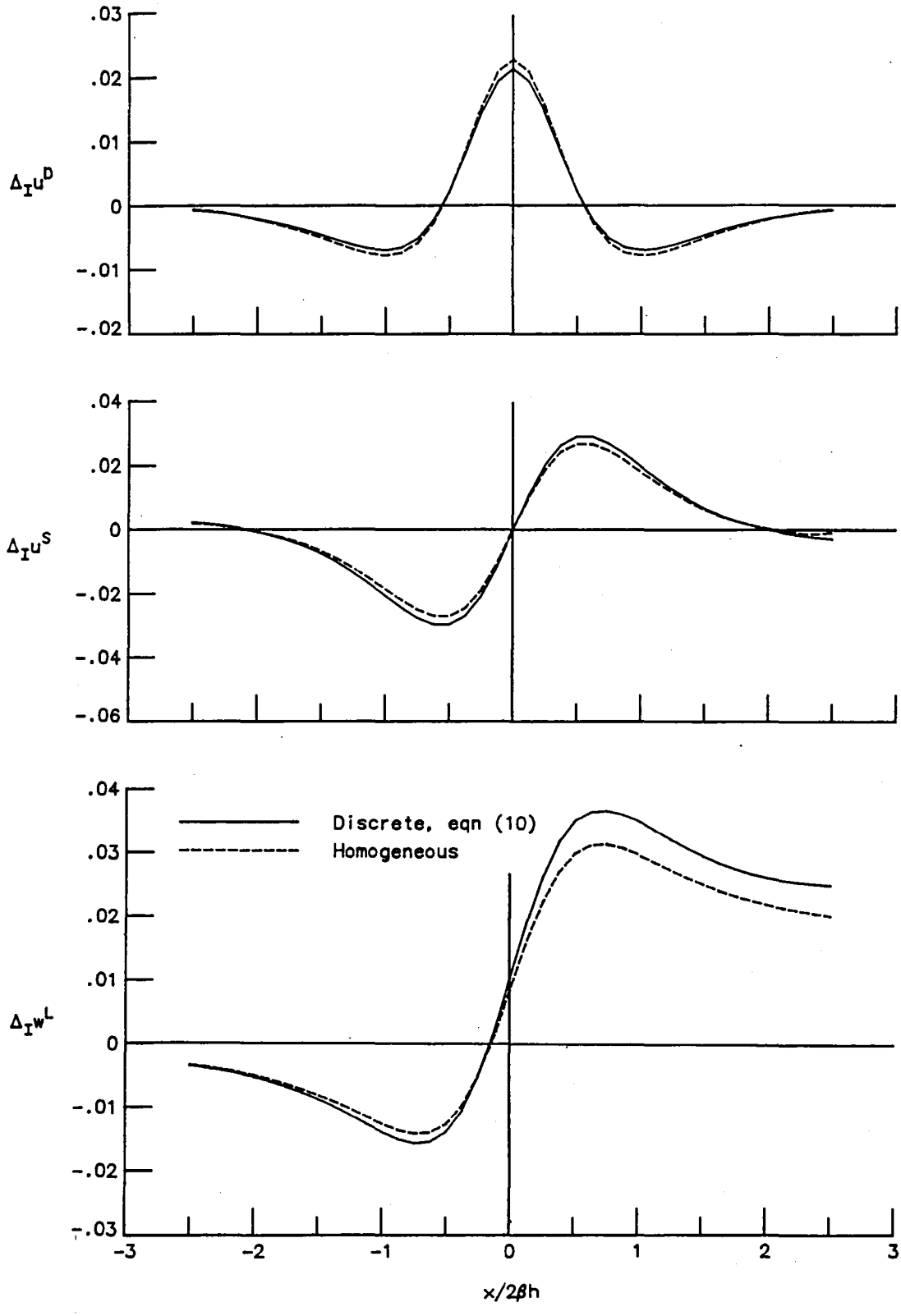

(b) Interference velocities at tunnel axis.

Figure 9. - Concluded.

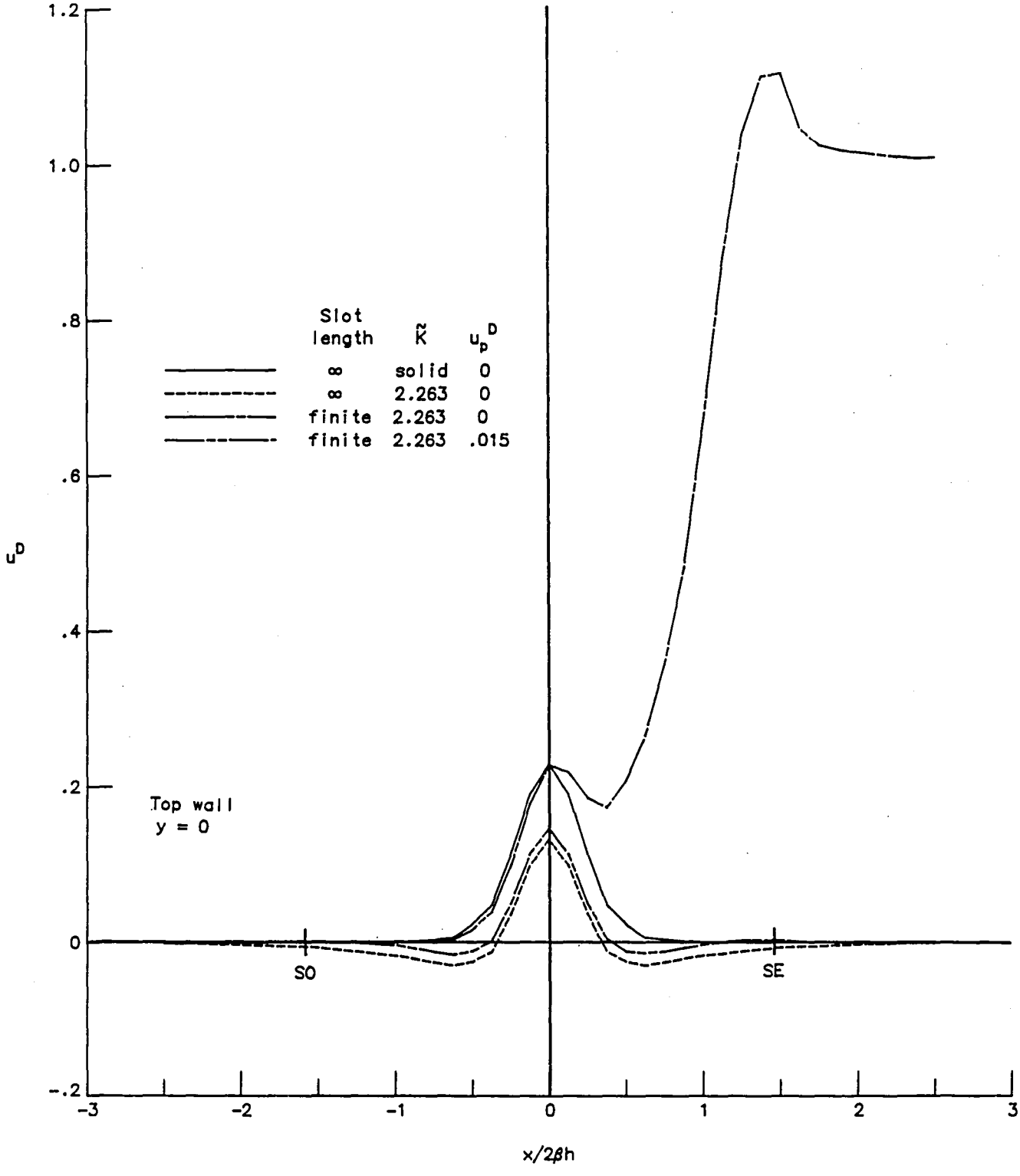

Figure 10. - Effect of finite slot length on longitudinal velocity at top wall centerline with point doublet disturbance, illustrating plenum pressure effect.

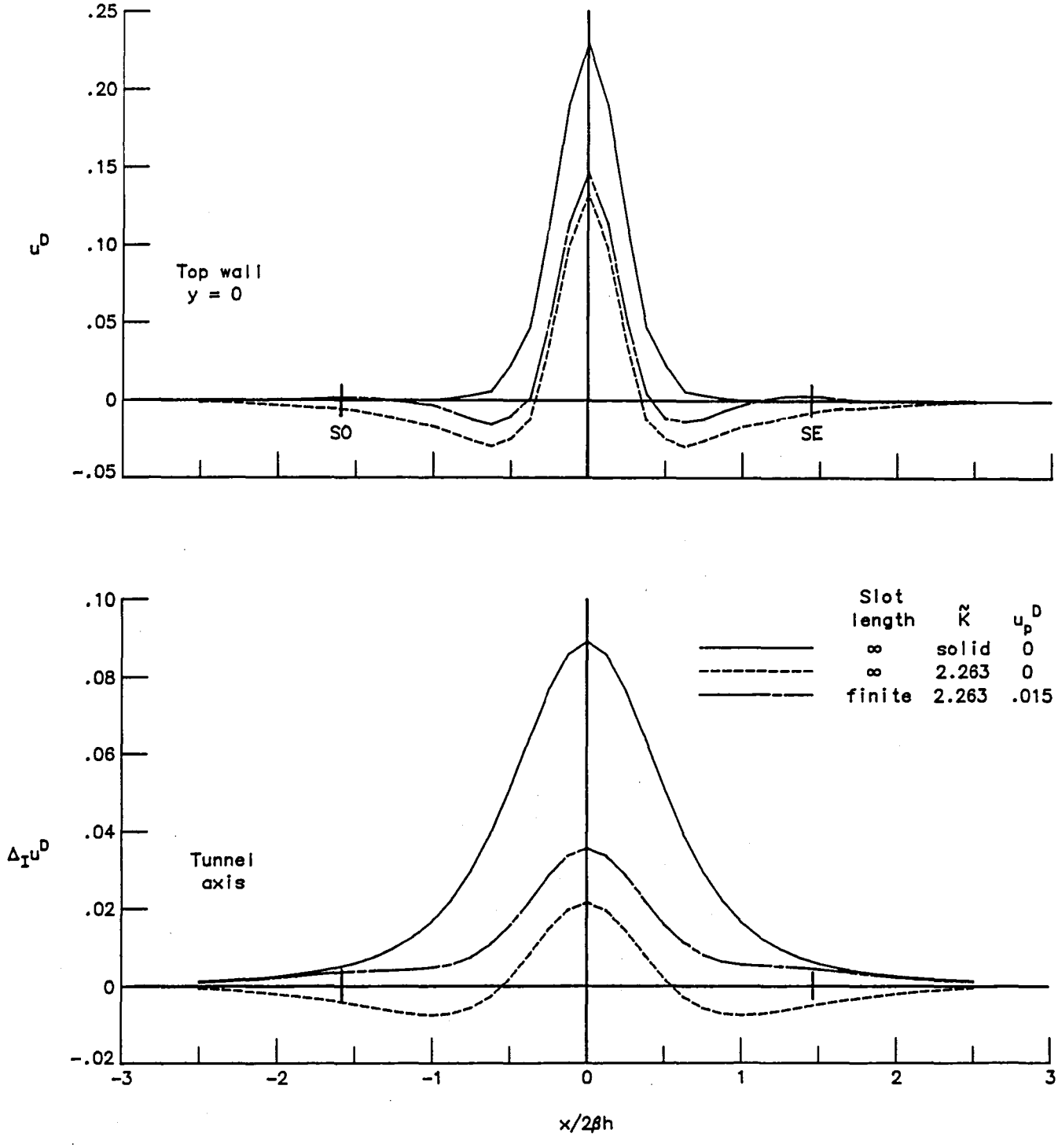

(a) Point doublet disturbance.

Figure 11. - Effect of finite slot length on longitudinal velocity at top wall centerline and interference velocity at tunnel axis.

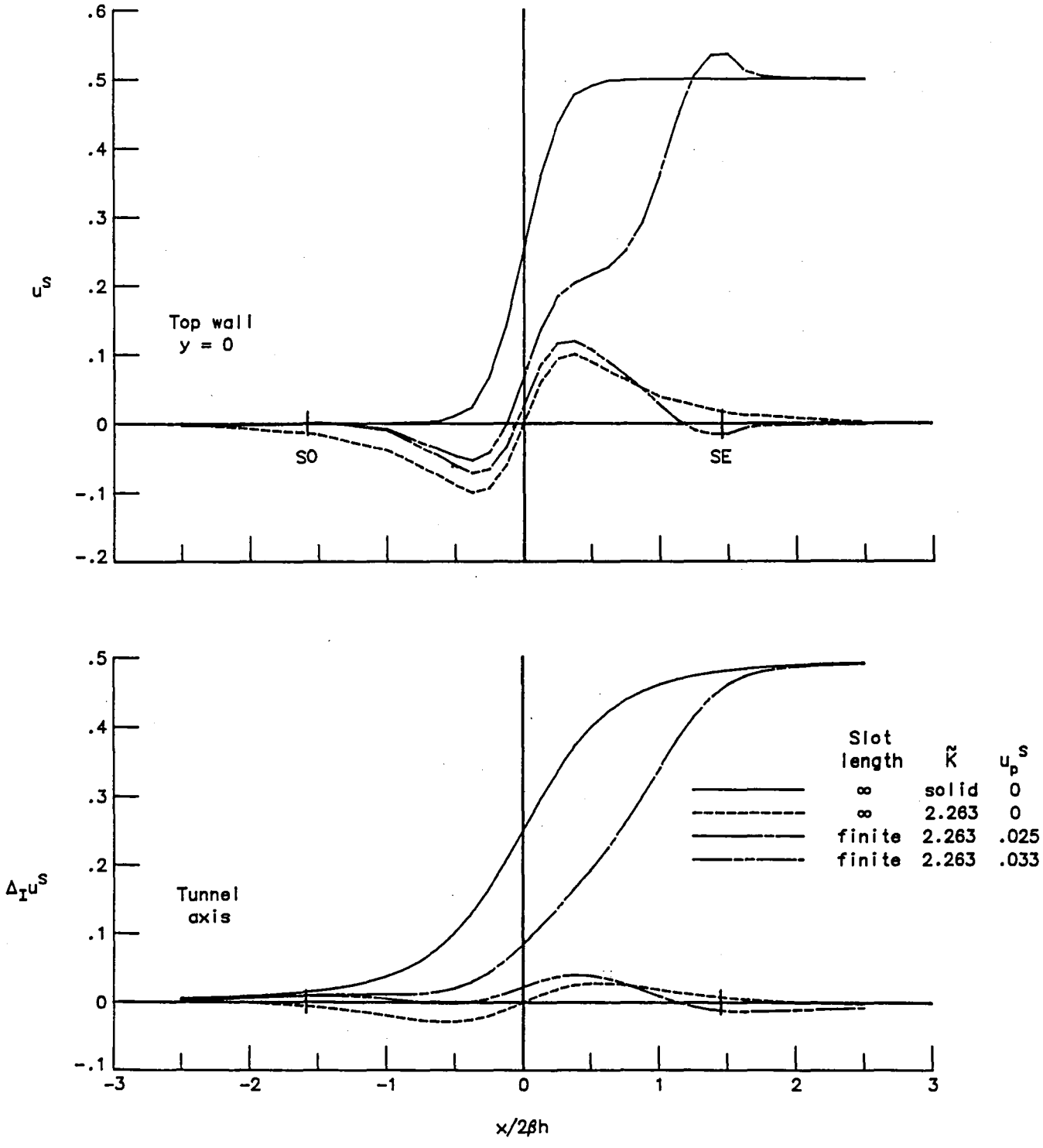

(b) Point source disturbance.

Figure 11. - Continued.

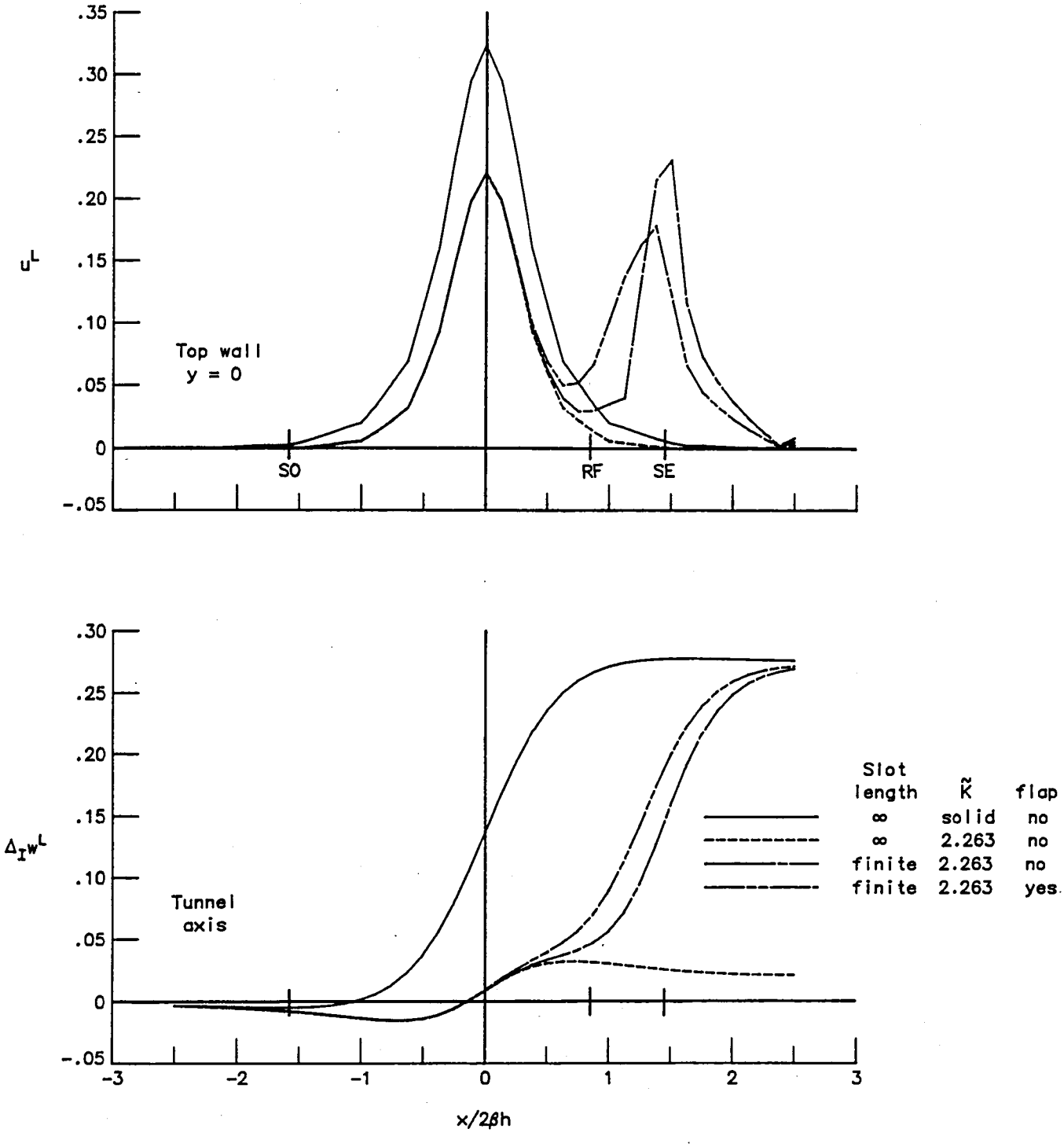

(c) Point lift disturbance.

Figure 11. - Concluded.

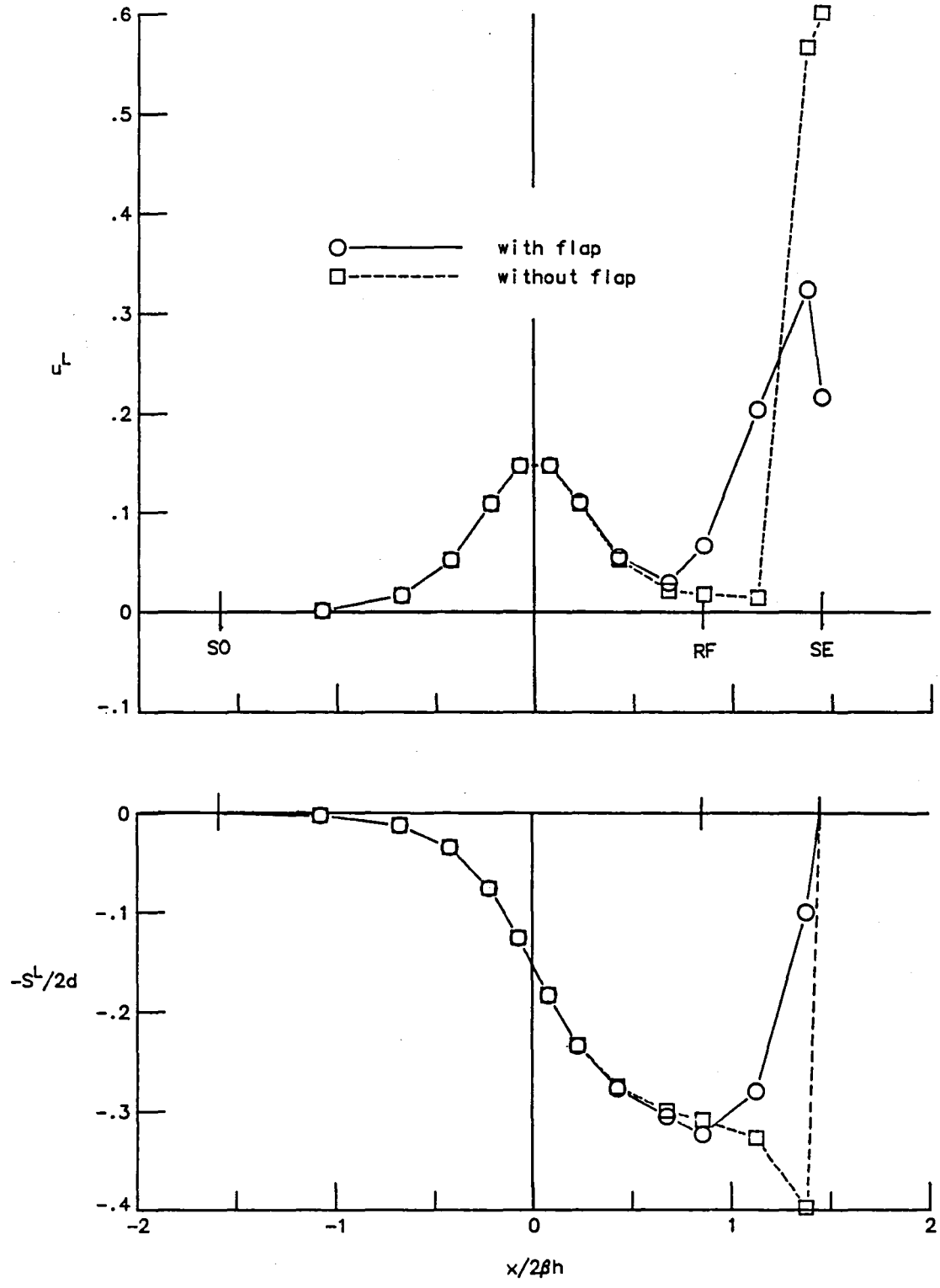

Figure 12. - Effect of simulated reentry flap on longitudinal velocity and slot flux at slot control points, point lift disturbance, top wall, y=h/6.

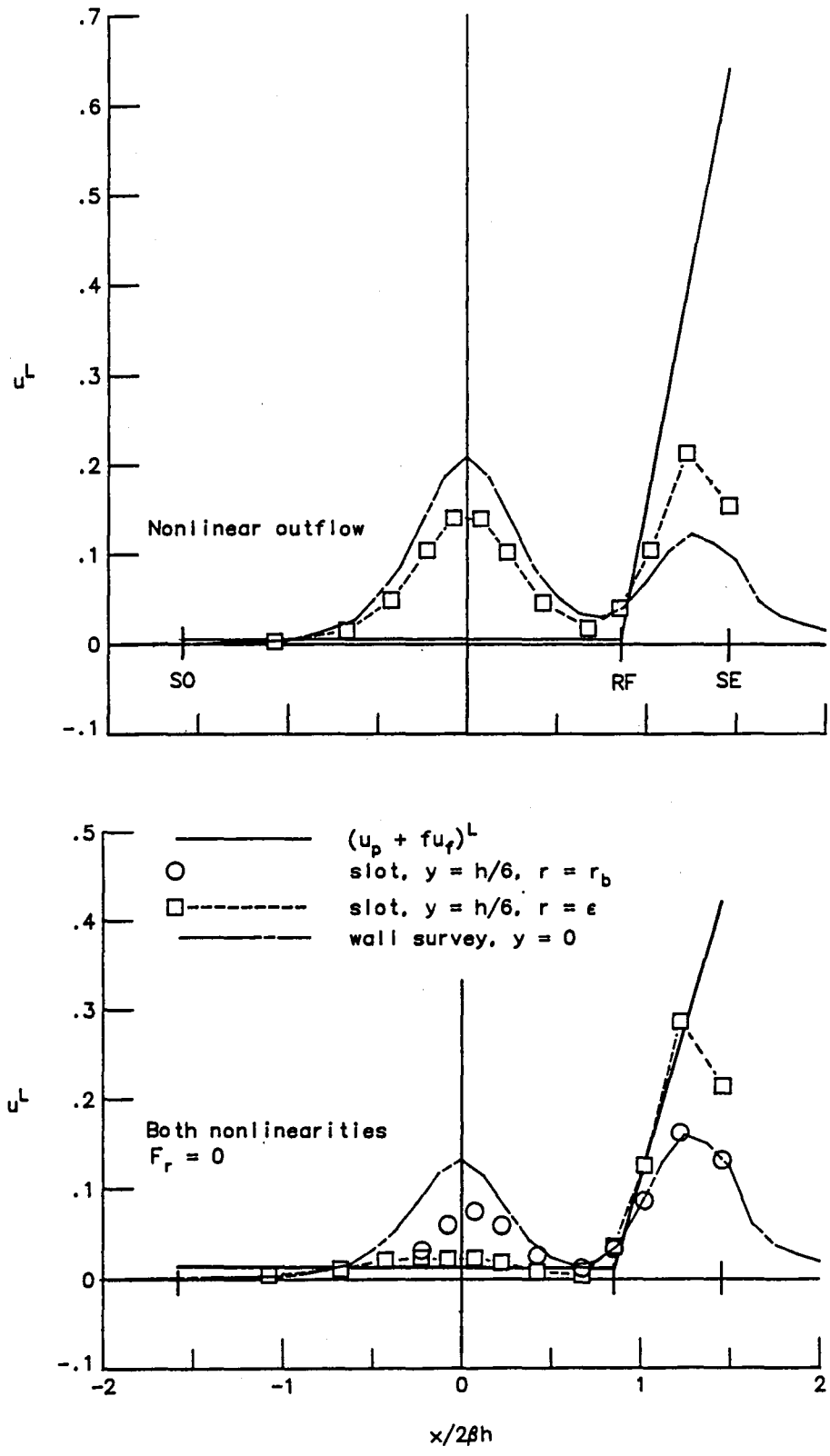

Figure 13. - Effect of slot inflow nonlinearity modeling on longitudinal velocity perturbations in vicinity of top wall centerline with point lift disturbance.

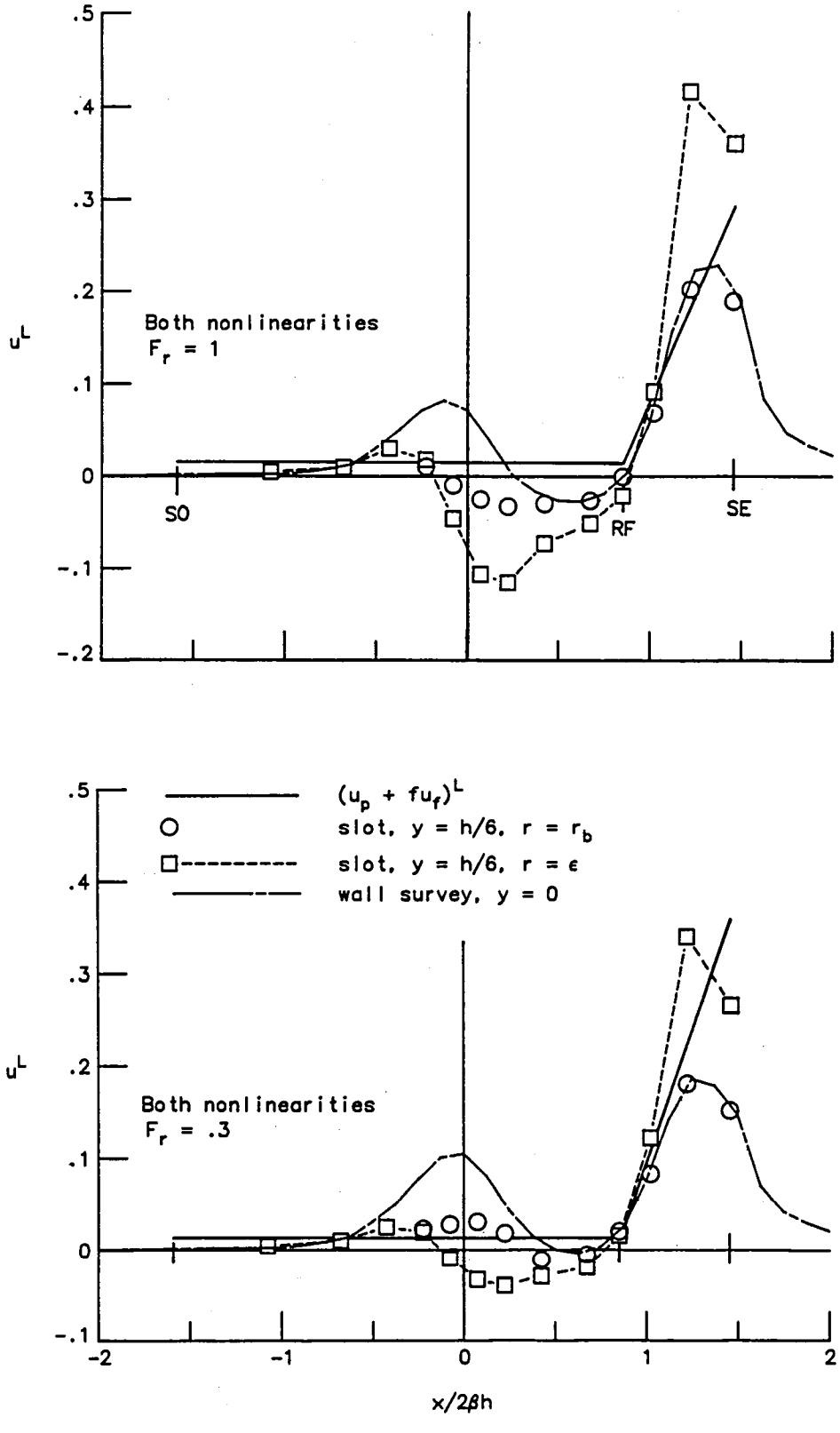

Figure 13. - Concluded.

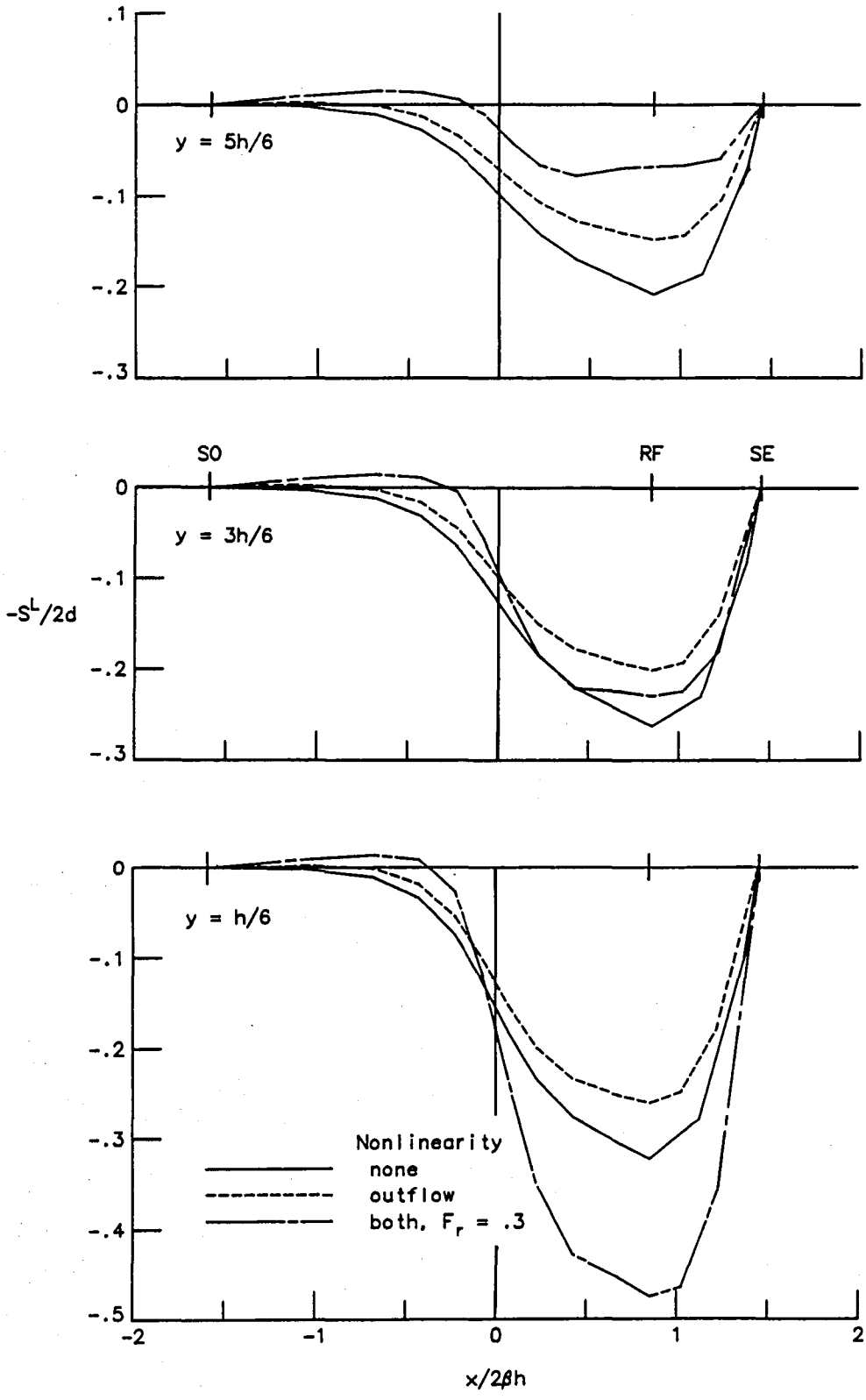

(a) Top wall slot flux distributions.

Figure 14. - Effect of slot boundary condition nonlinearities on tunnel flow properties with point lift disturbance.

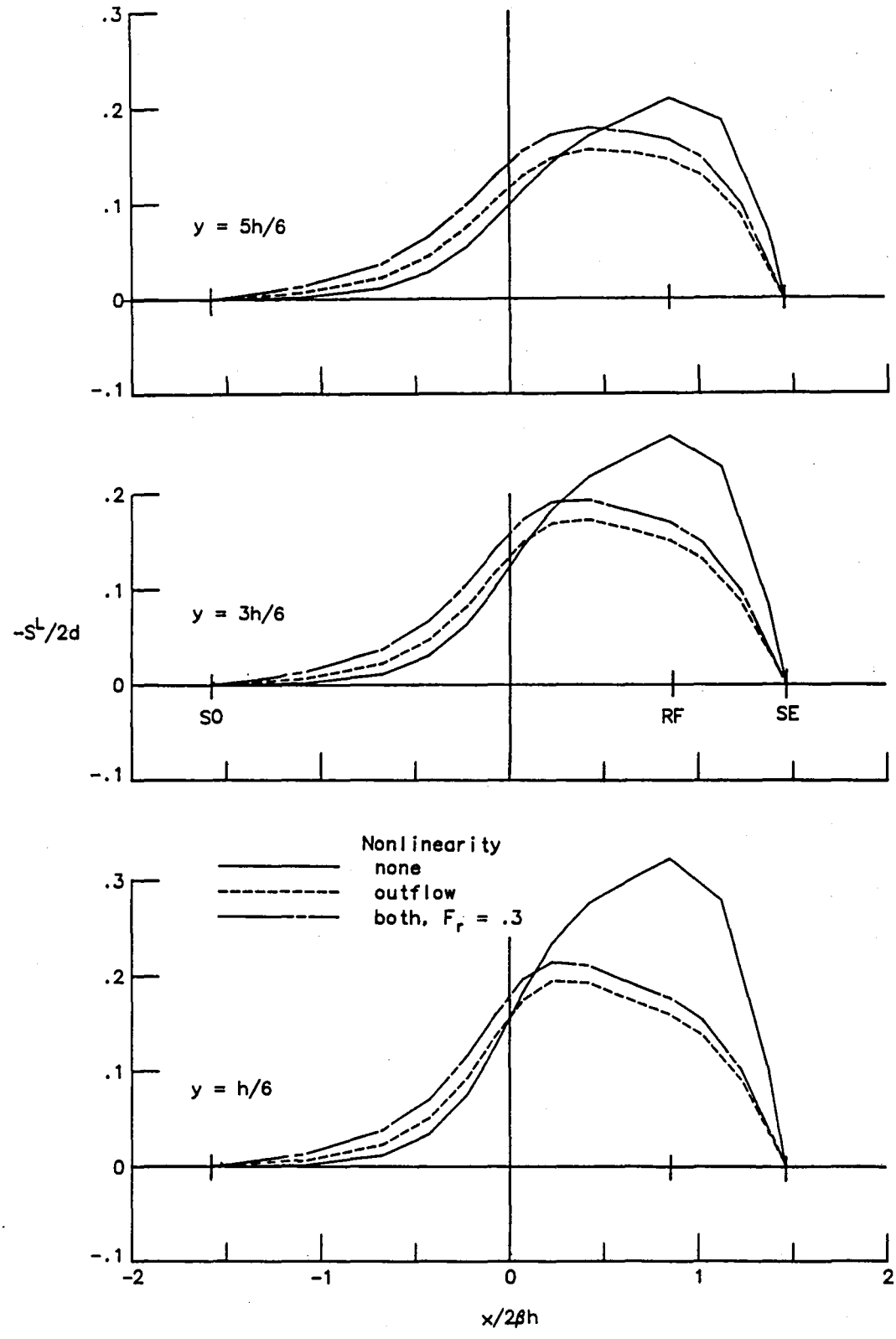

(b) Bottom wall slot flux distributions

Figure 14. - Continued.

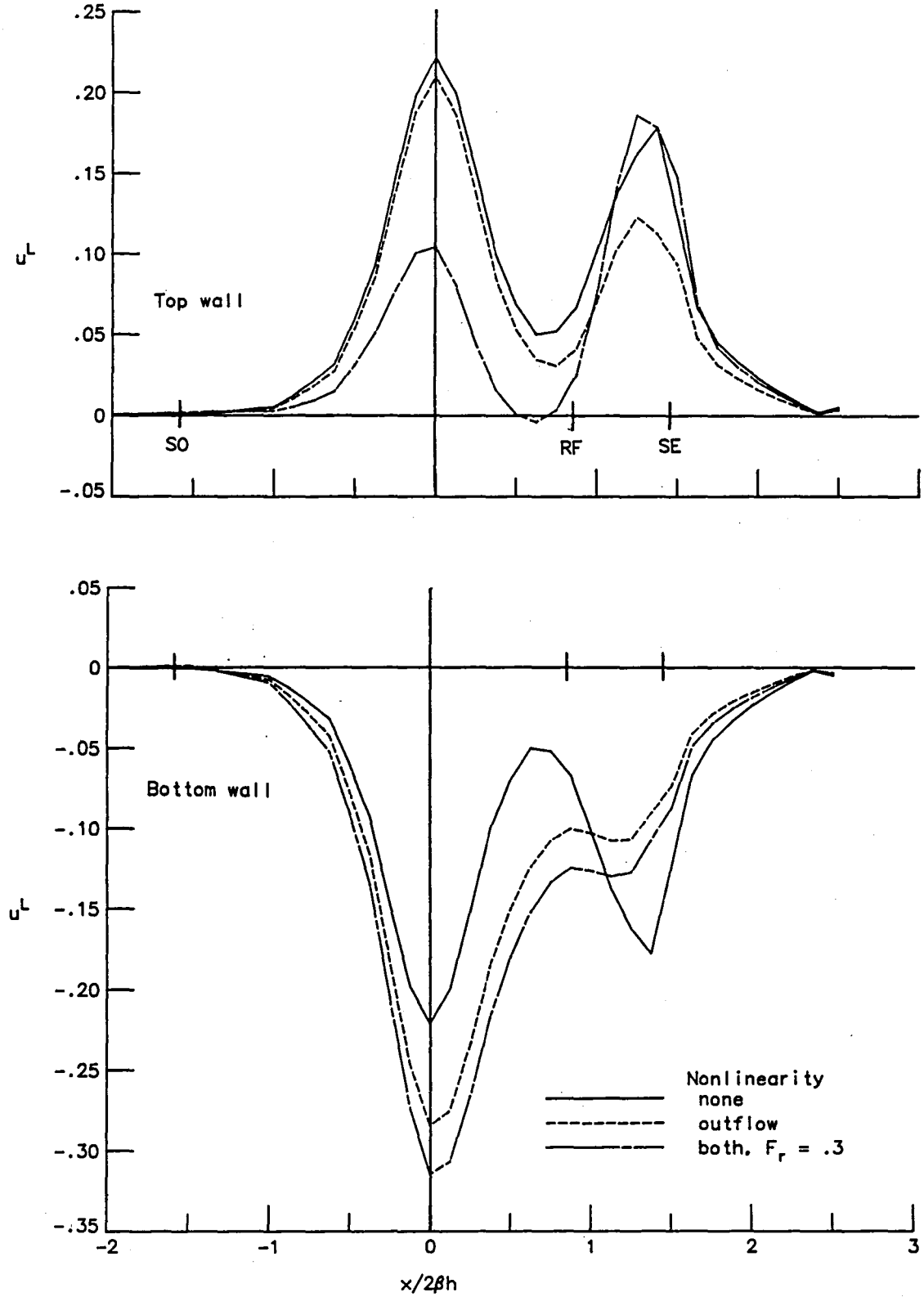

(c) Longitudinal velocity perturbation at top and bottom wall centerlines.

Figure 14. - Continued.

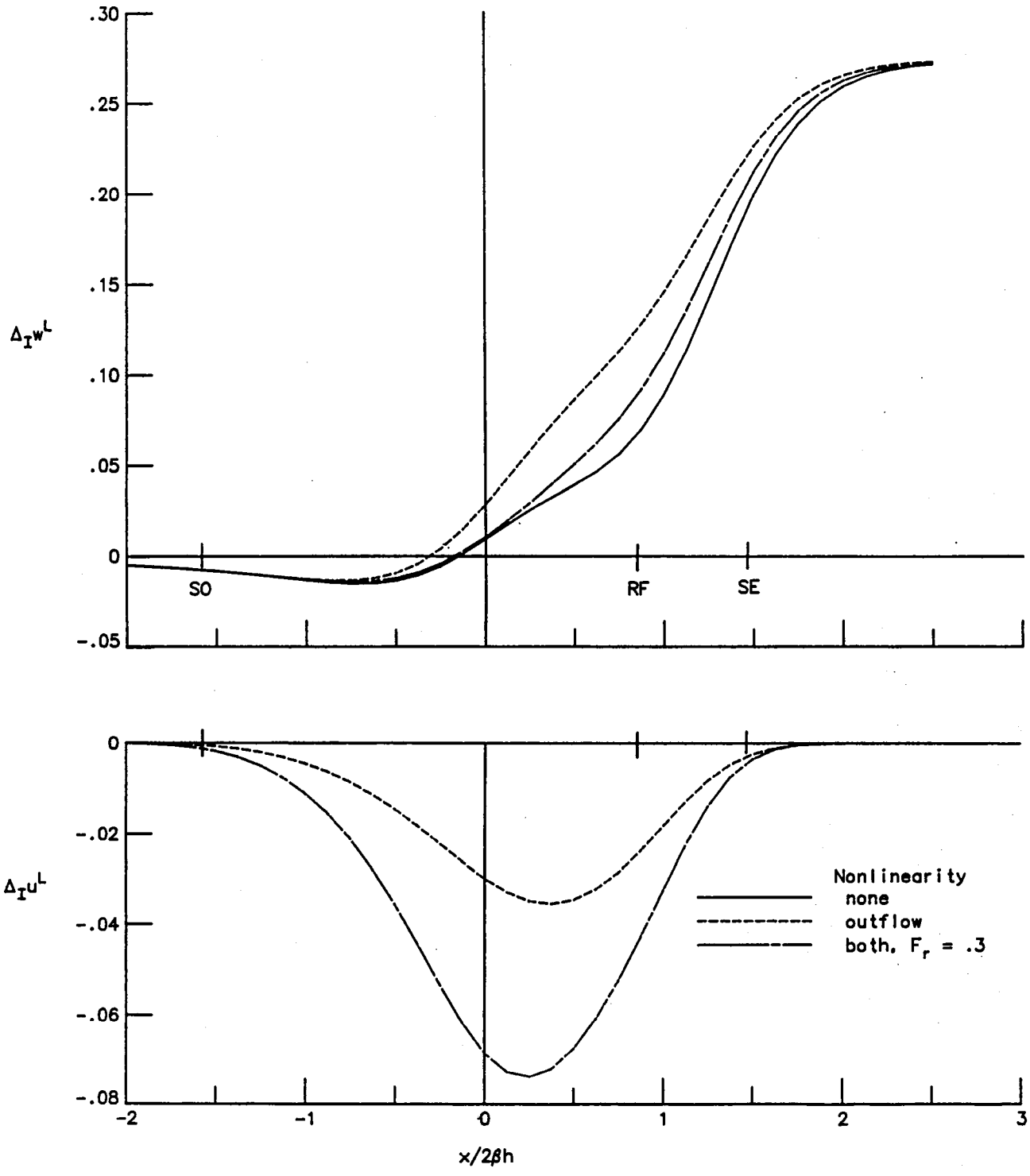

(d) Interference velocity at tunnel axis.

Figure 14. - Concluded.

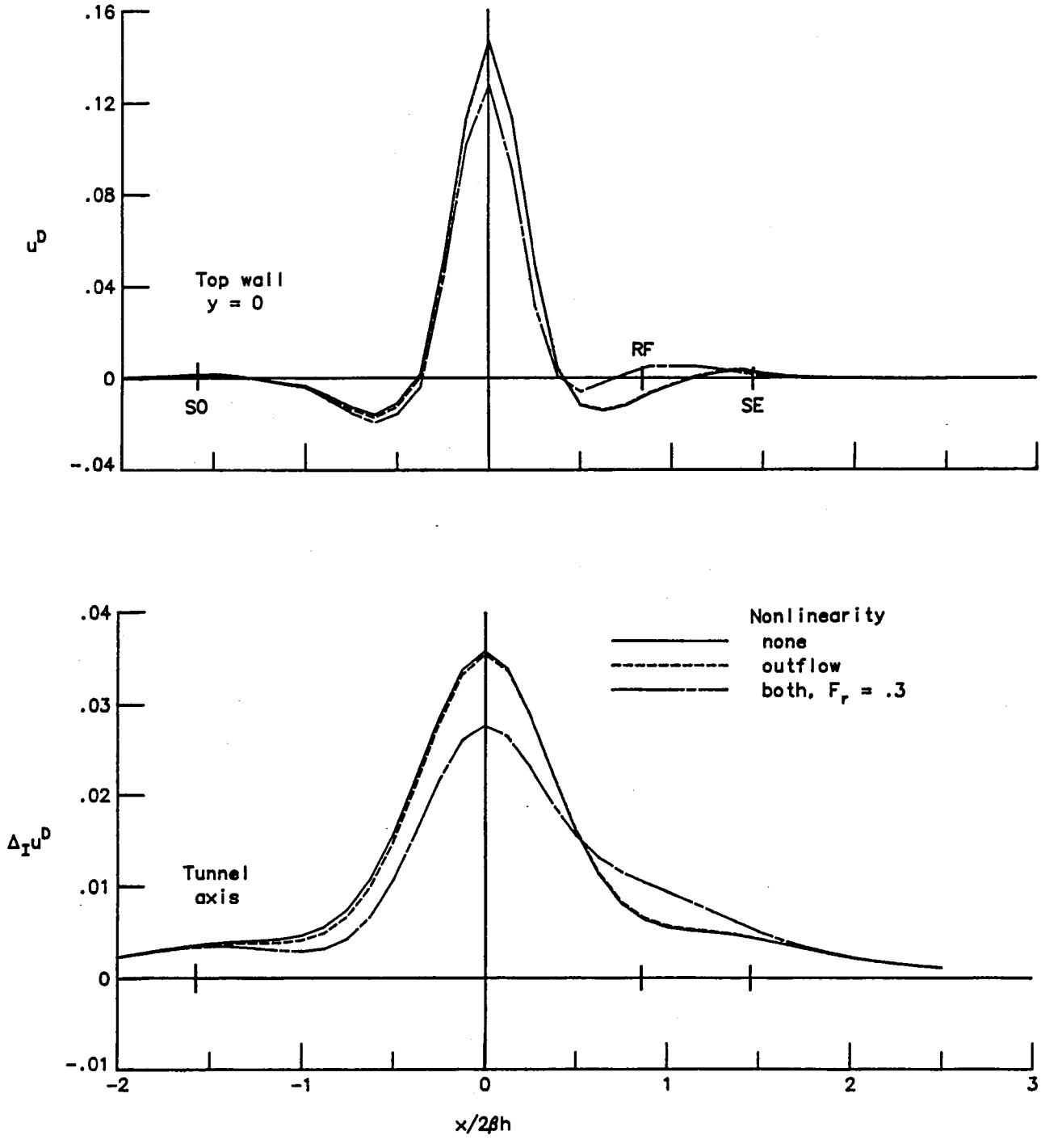

(a) Point doublet disturbance.

Figure 15. - Effect of slot boundary condition nonlinearities on longitudinal velocity at top wall centerline and interference velocity at tunnel axis.

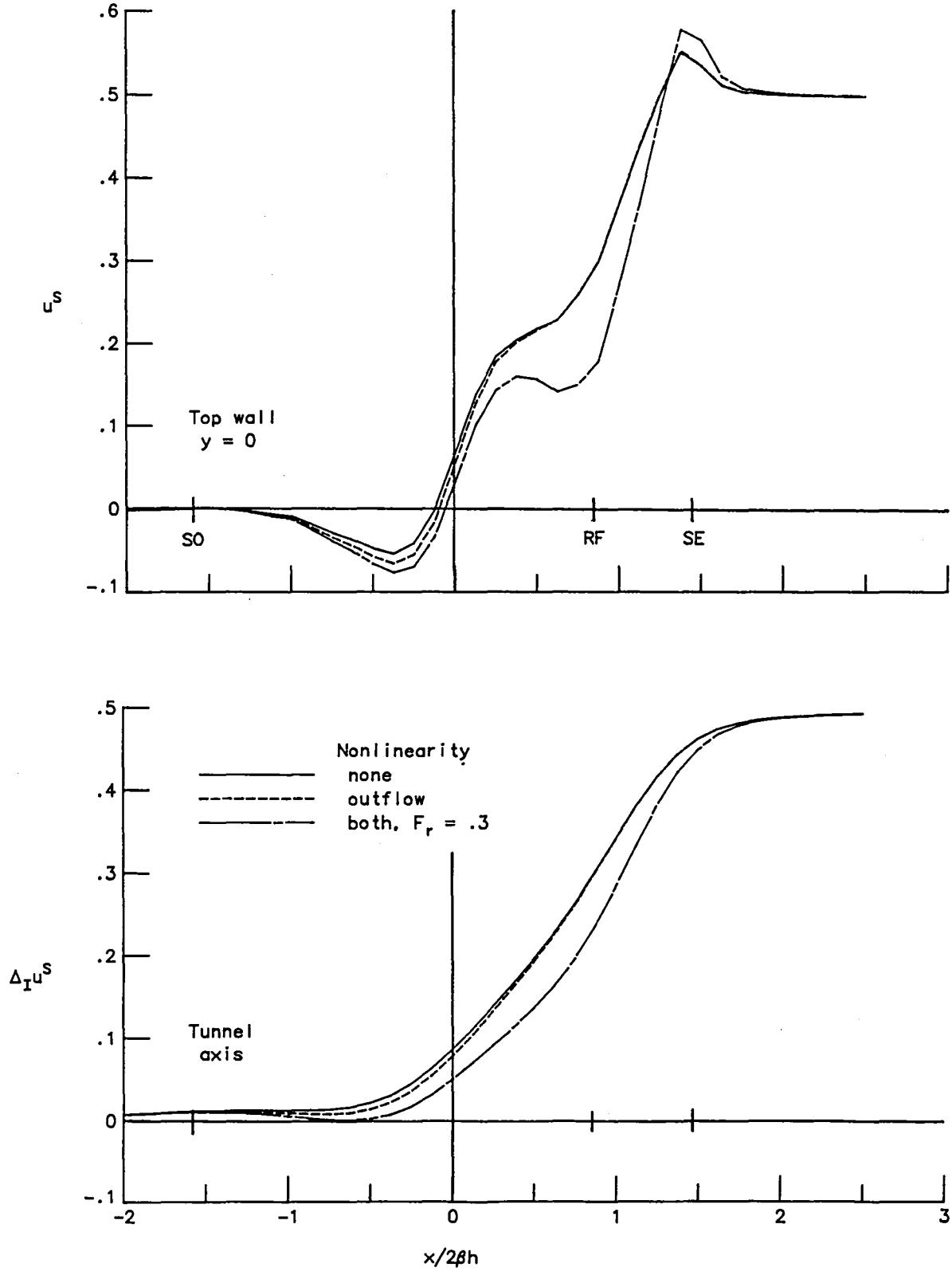

(b) Point source disturbance.

Figure 15. - Concluded.

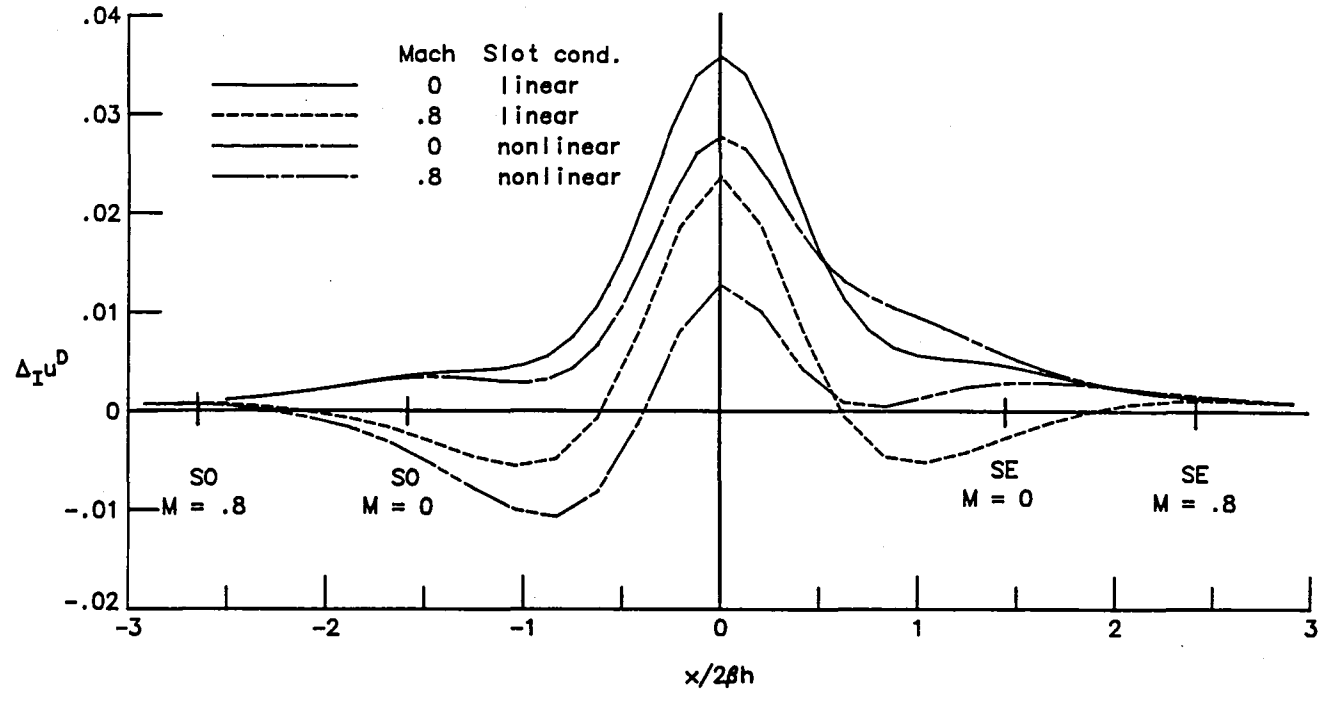

(a) Point doublet disturbance.

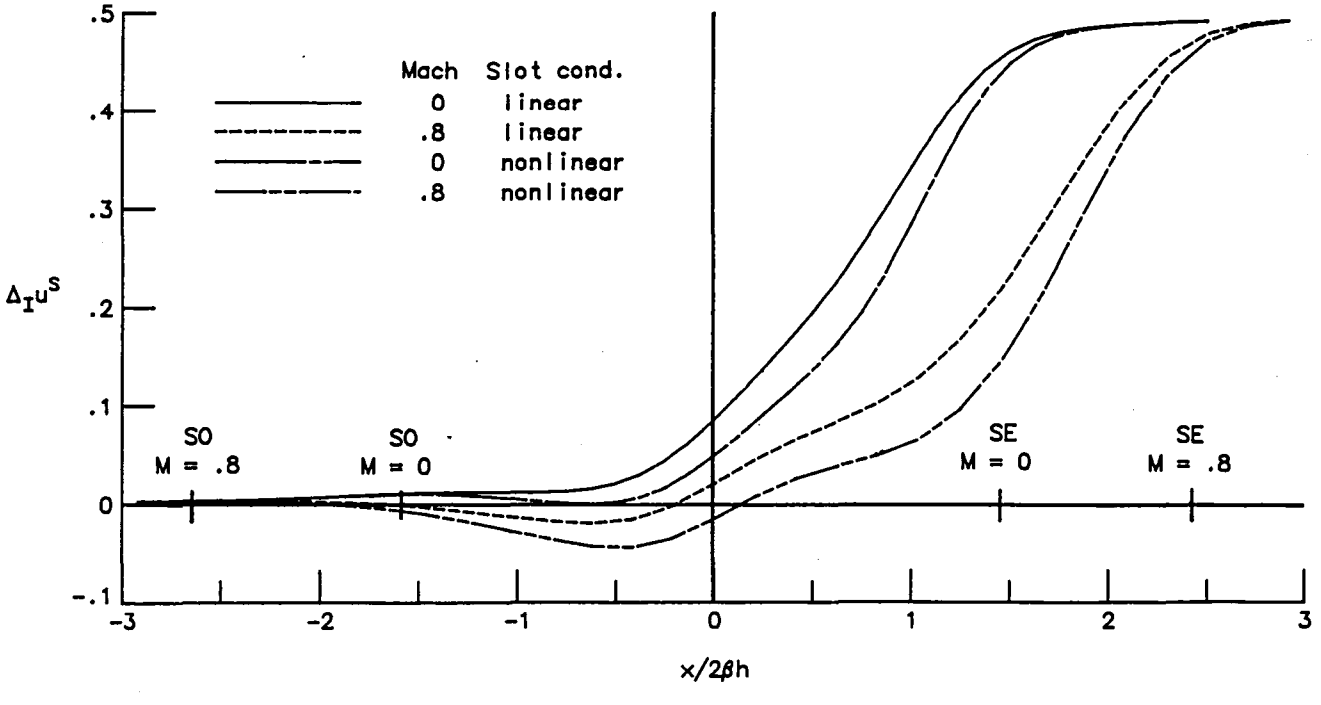

(b) Point source disturbance.

Figure 16. - Effect of Mach number on interference velocity distribution at tunnel axis with linear and nonlinear slot boundary conditions.

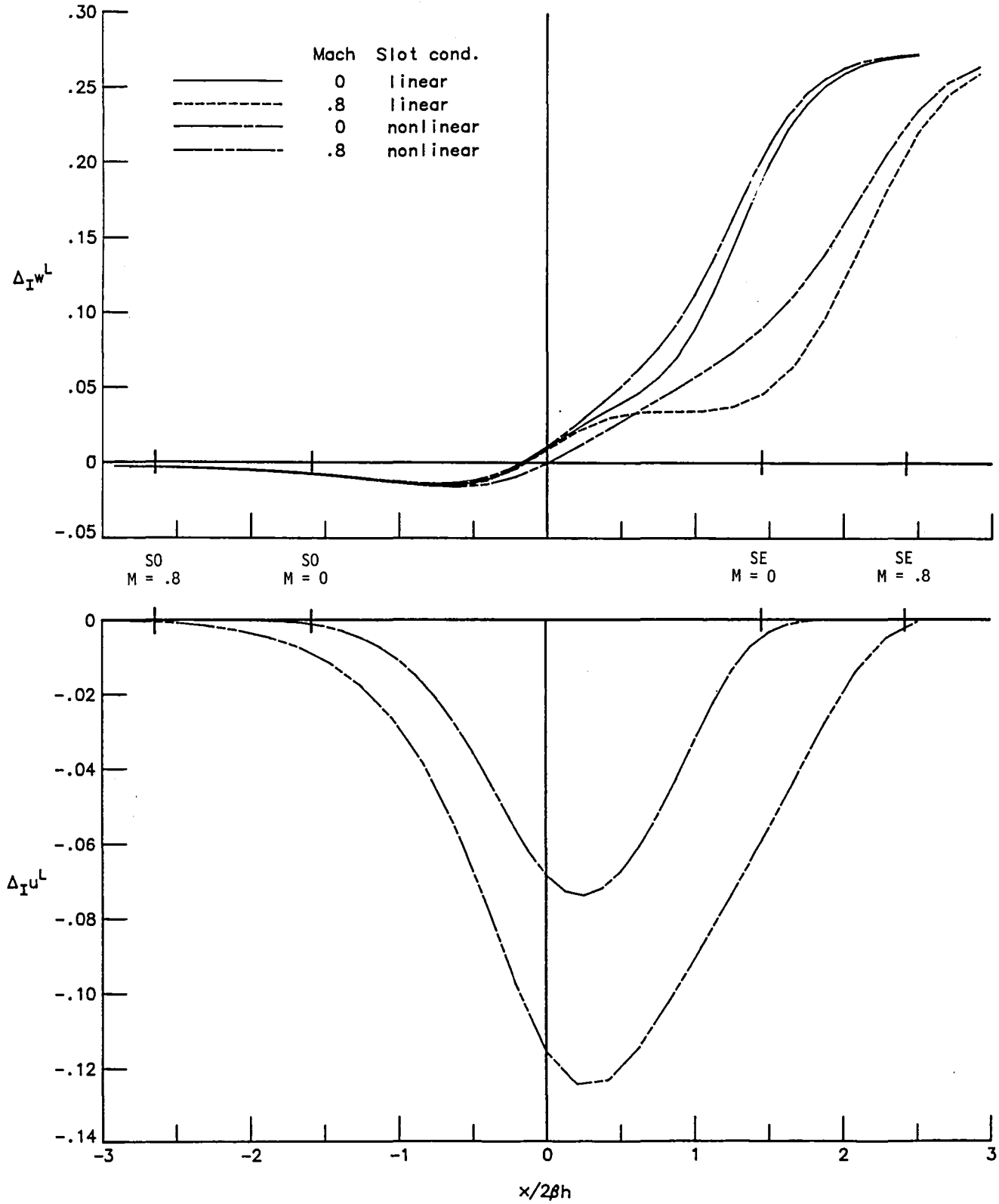

(c) Point lift disturbance.

Figure 16. - Concluded.

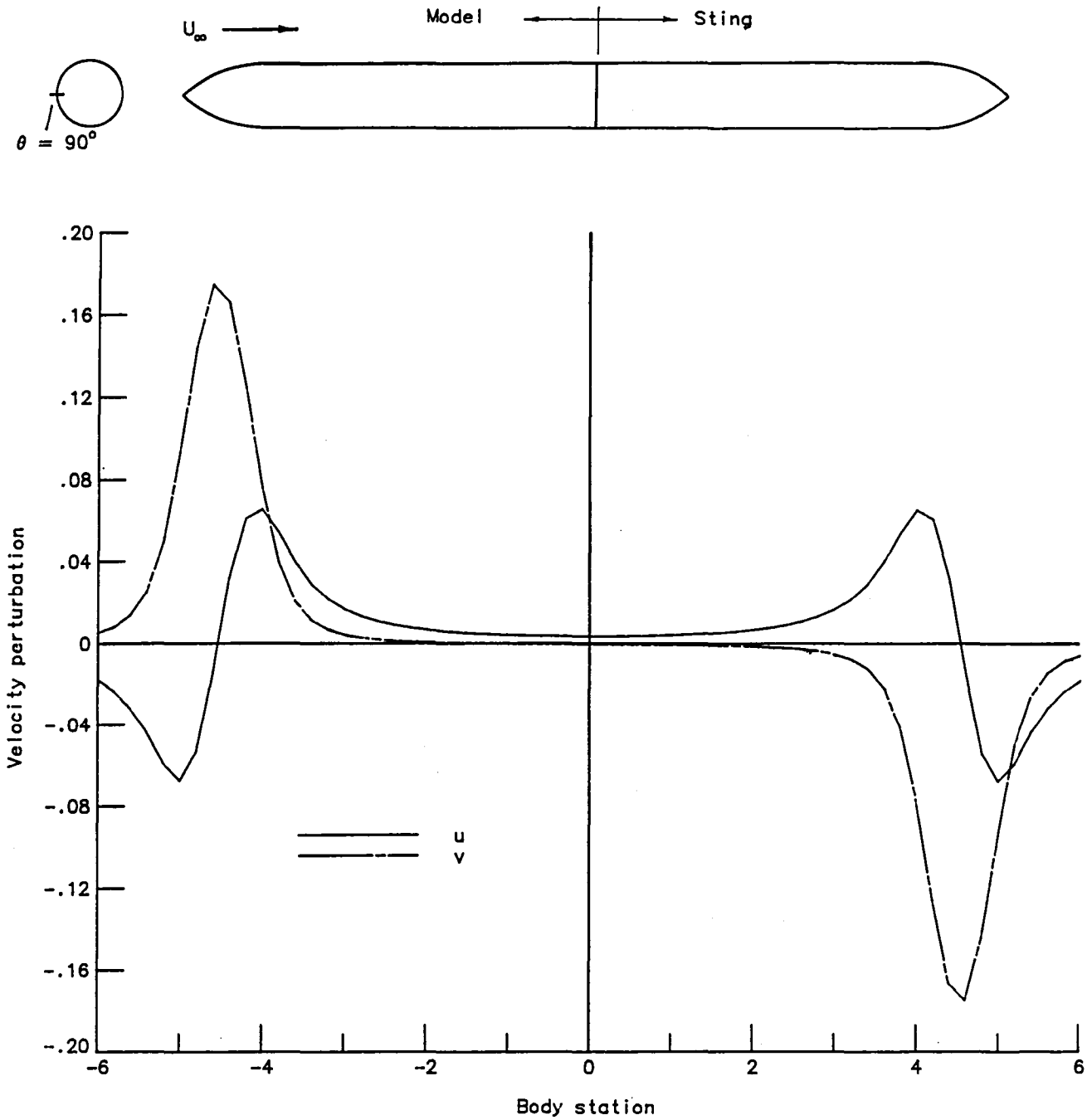

(a) Angle of attack = 0°.

Figure 17. - Velocity perturbations induced by isolated ogive-cylinder model and cylinder-ogive sting on survey lines at cylinder surface.

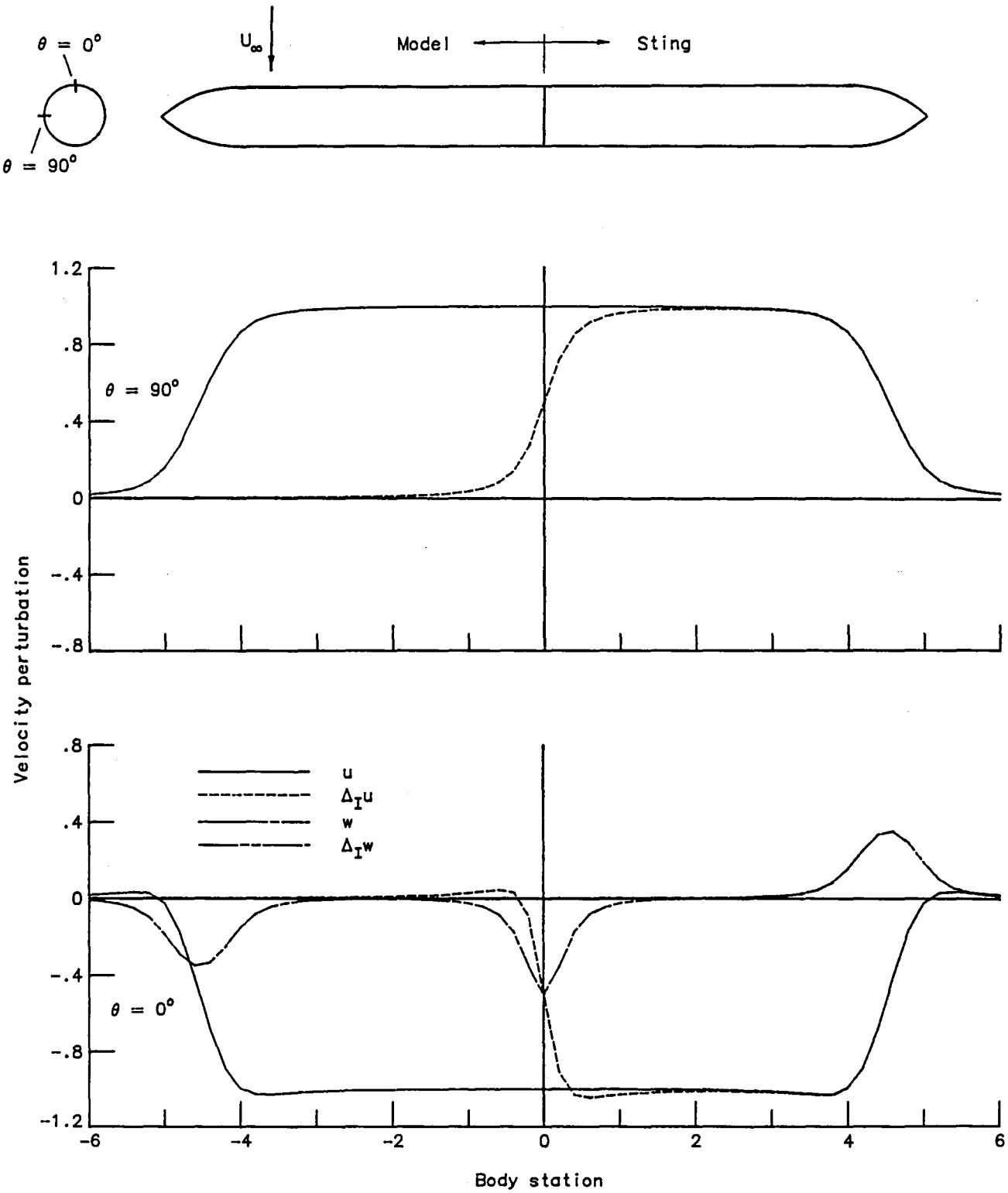

(b) Angle of attack = -90°.

Figure 17. - Continued.

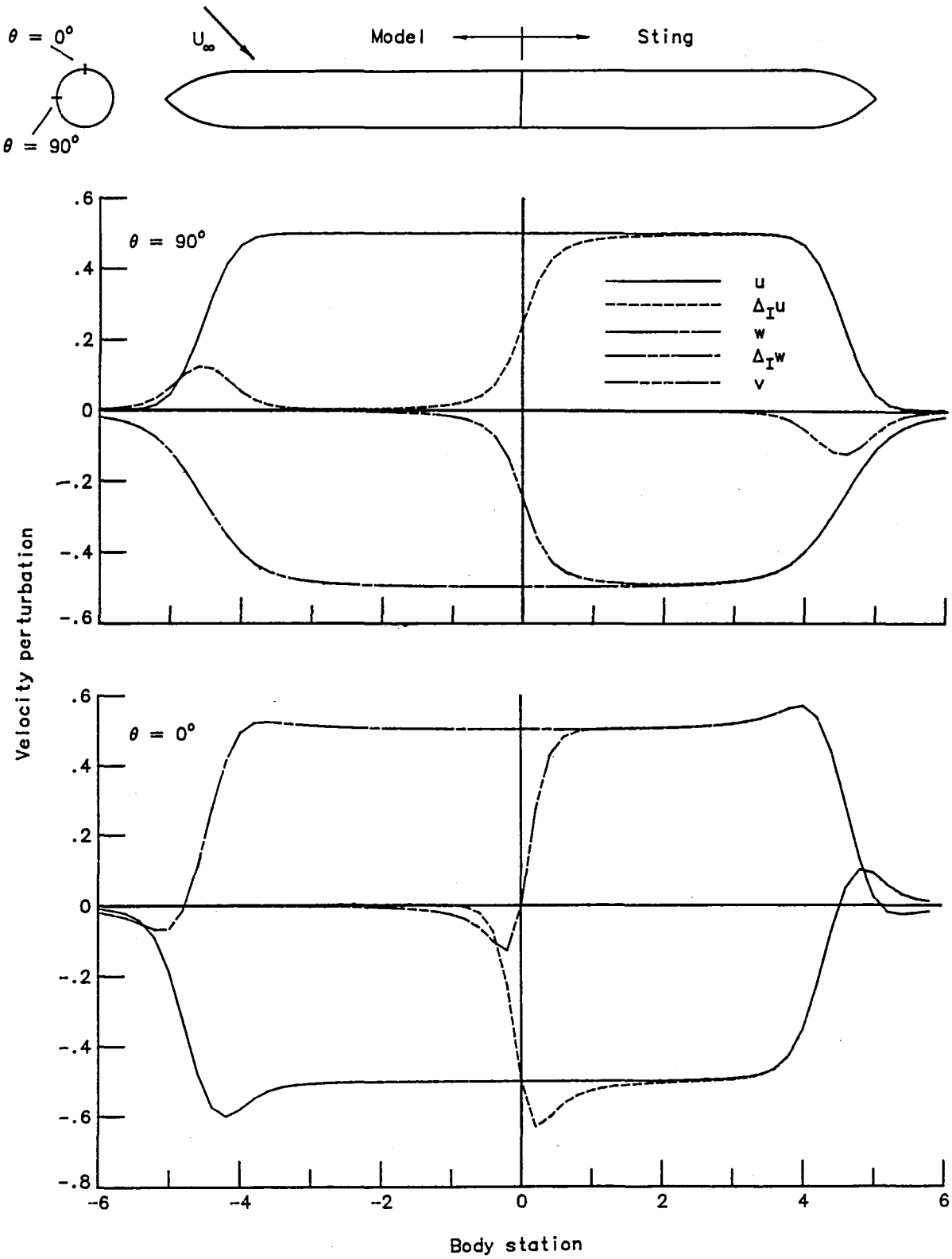

(c) Angle of attack = -45°.

Figure 17. - Concluded.

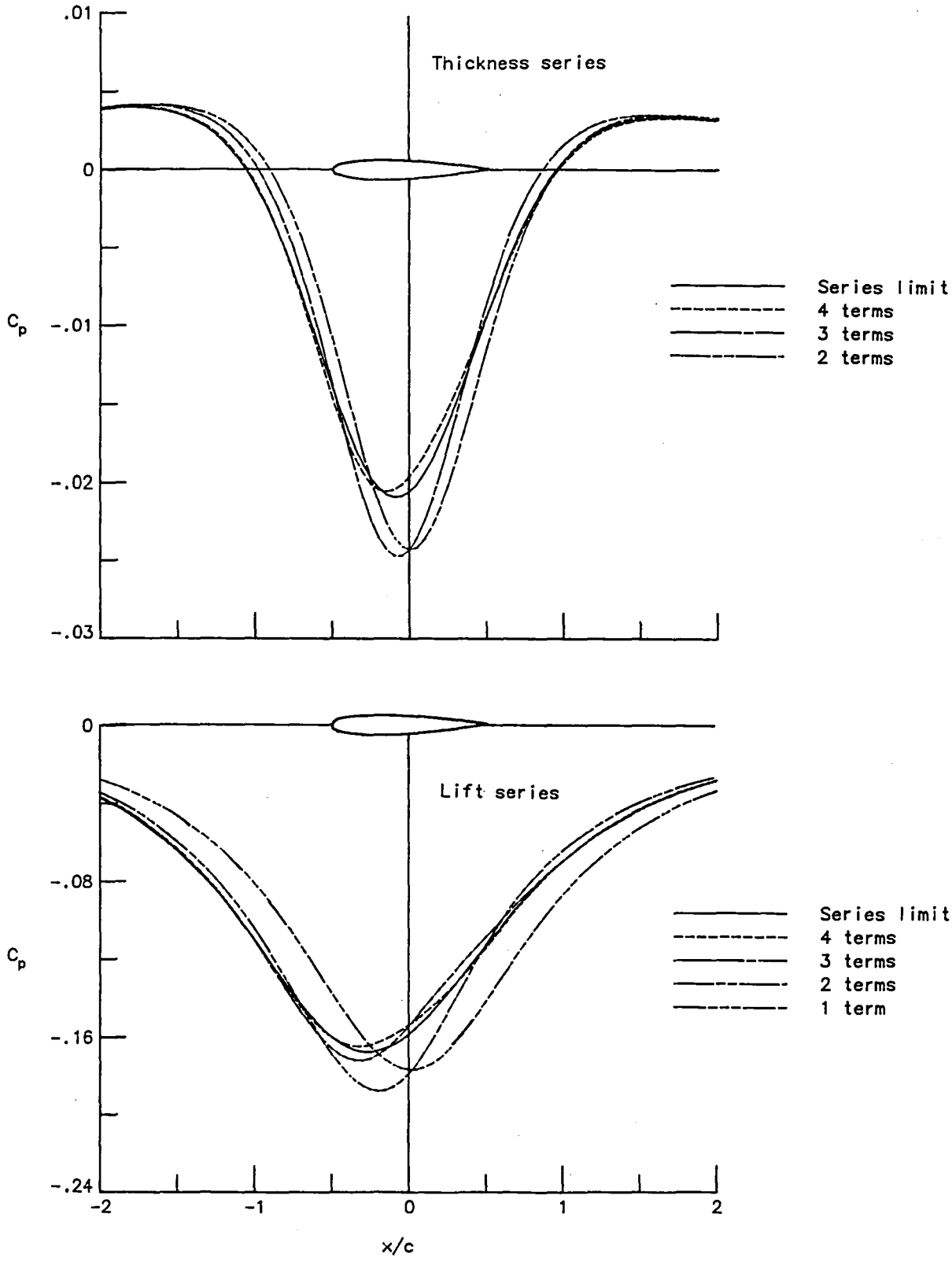

Figure 18. - Pressure coefficients induced by series representation of thickness and lift distributions of an isolated, aspect ratio 6, rectangular wing with NACA 0012 airfoil section at unit lift coefficient. Survey at $y = 0$, $z = c$.

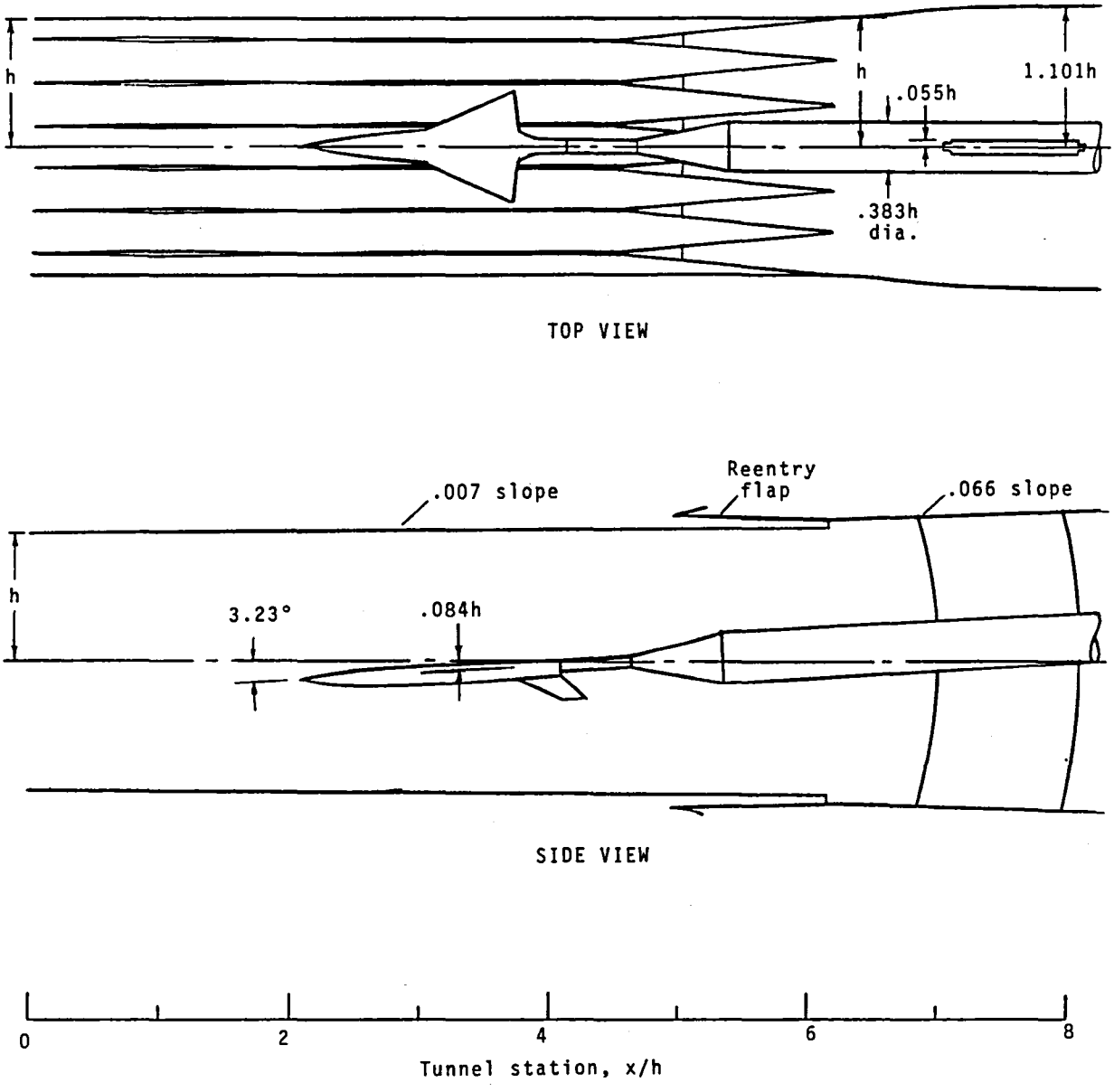

Figure 19. - Sketch of test section of Diffuser Flow Apparatus (DFA) with model installed for wall pressure investigation of ref. 21. Model inverted with $\alpha = 3.23^{\circ}$.

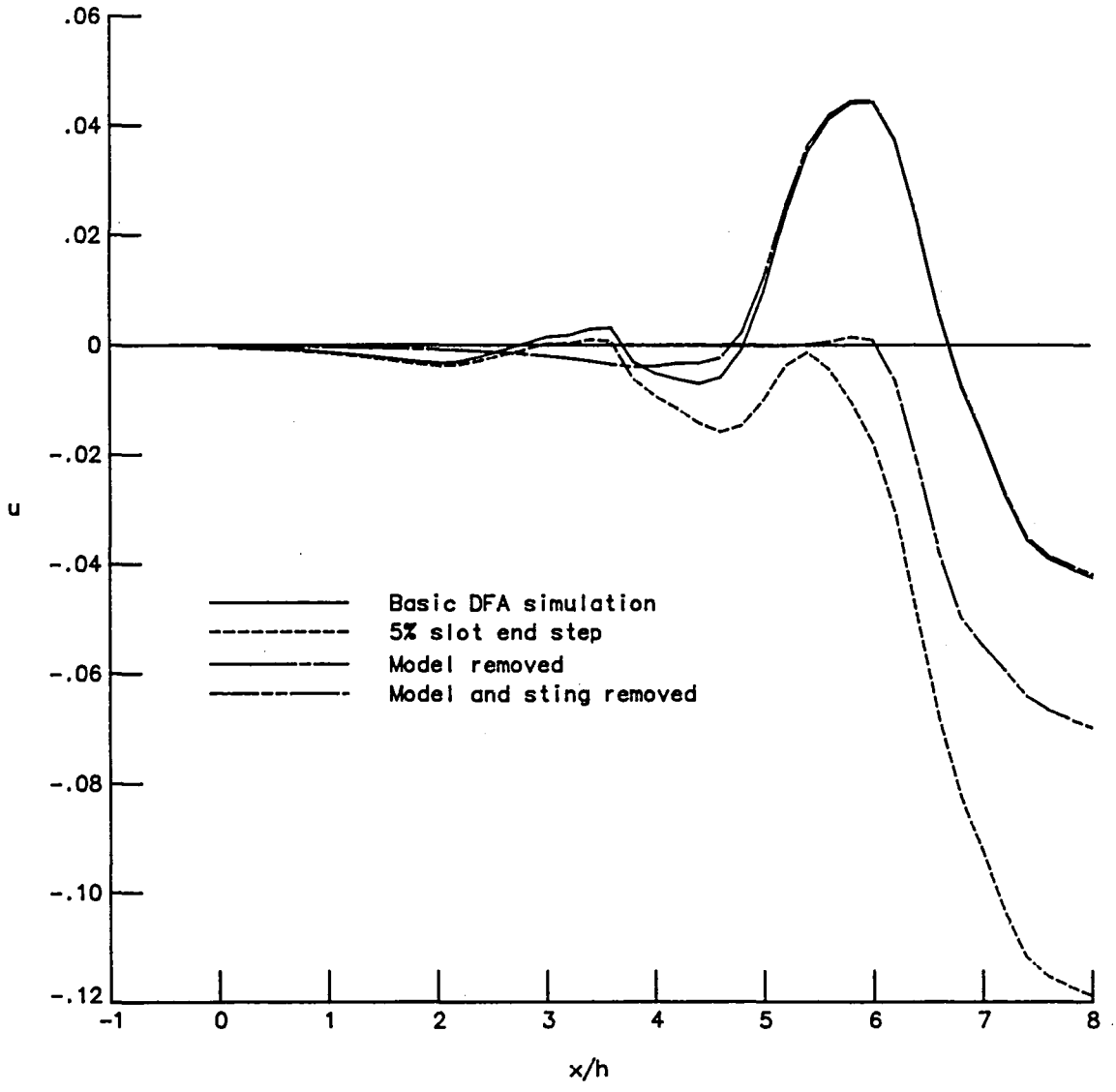

Figure 20. - Effect of some geometric features on longitudinal velocity distributions in a simulation of a sample case in the DFA wall pressure investigation. Survey line at $y = 0.6h$, $z = -.084h$.

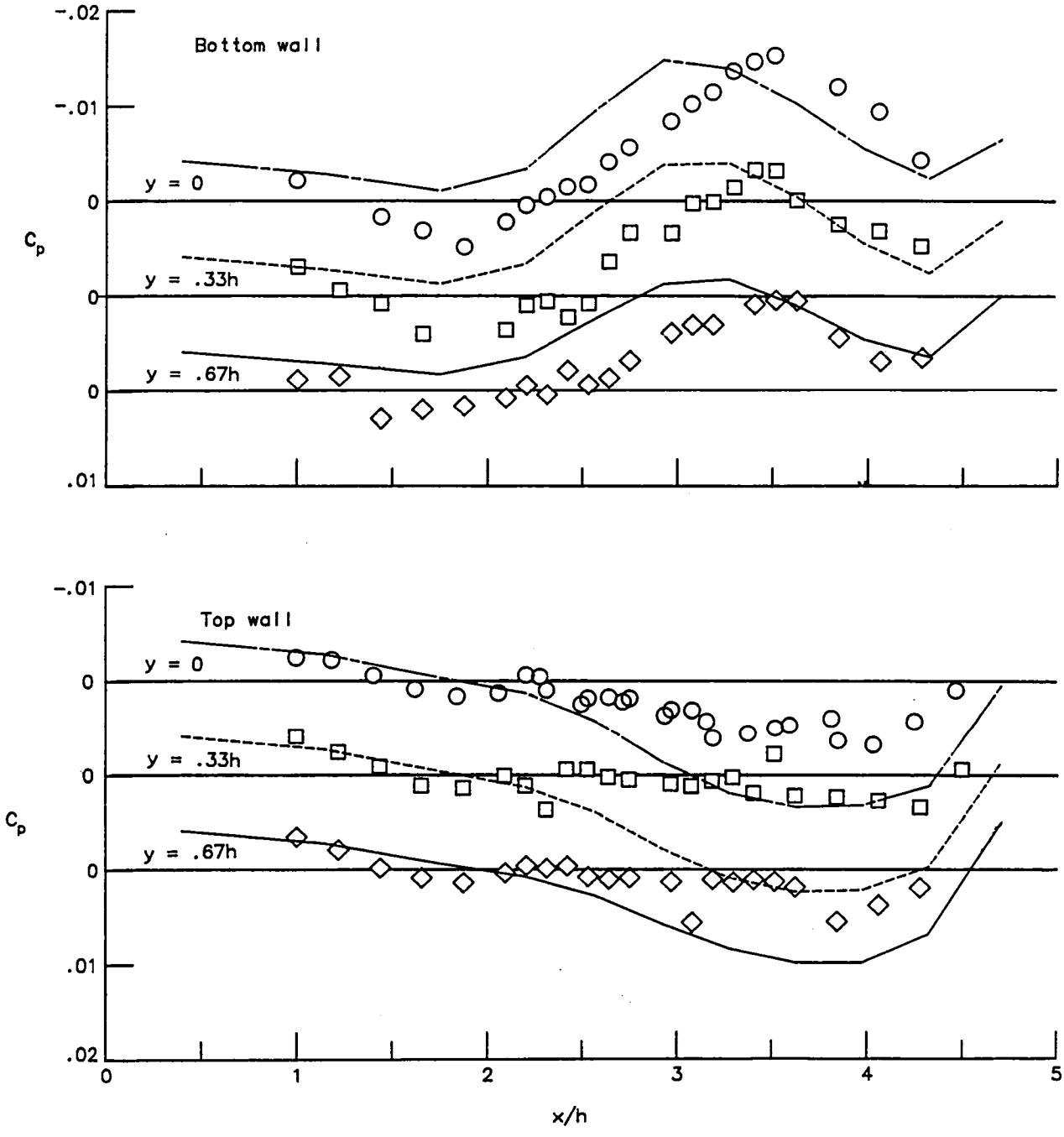

(a) Top and bottom wall pressures.

Figure 21. - Comparison of measured and simulated wall pressures in the DFA wall pressure investigation sample case. Simulated tunnel velocity adjusted to match sidewall centerline pressure at x = 0.36h.

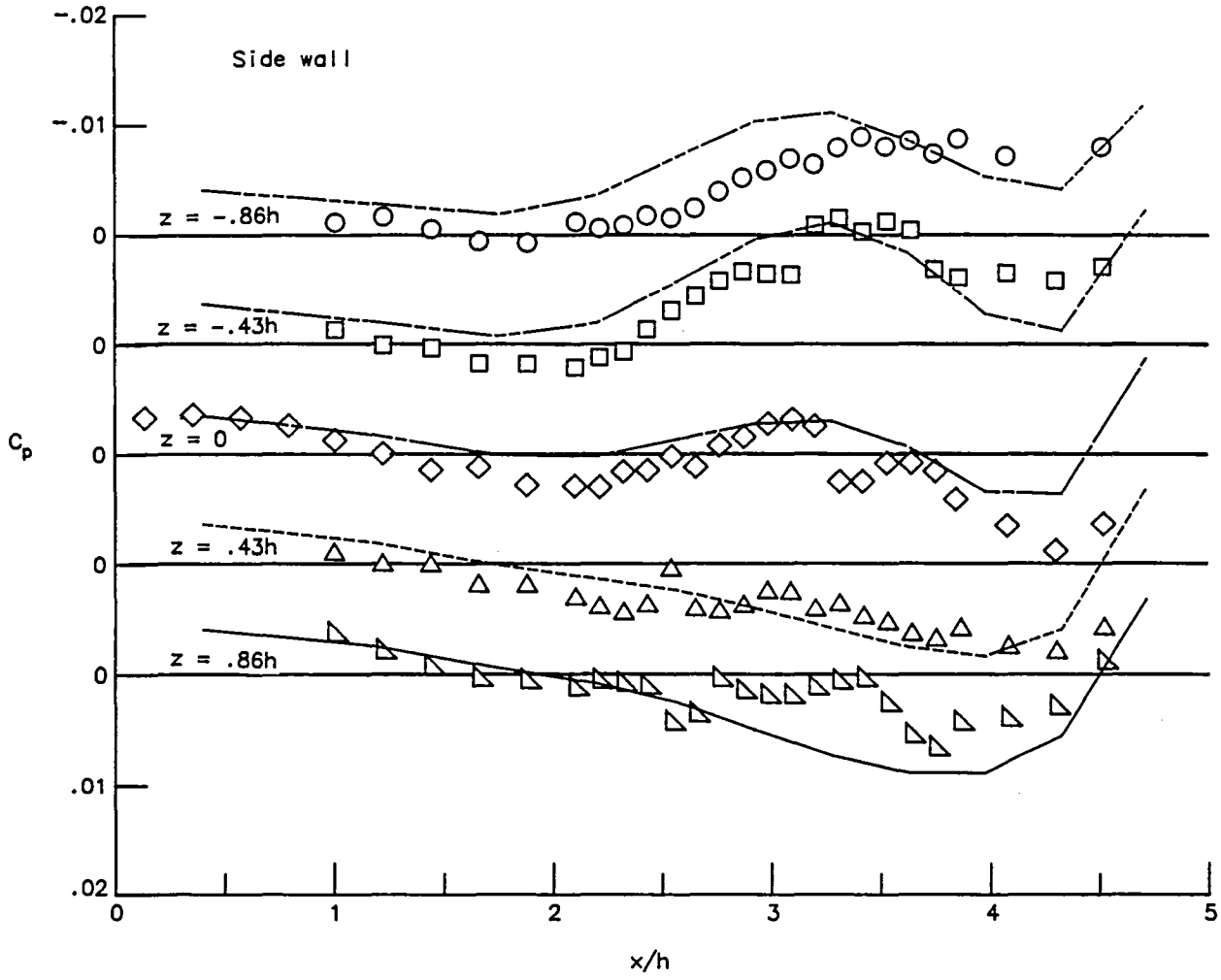

(b) Side wall pressures.

Figure 21. - Concluded.

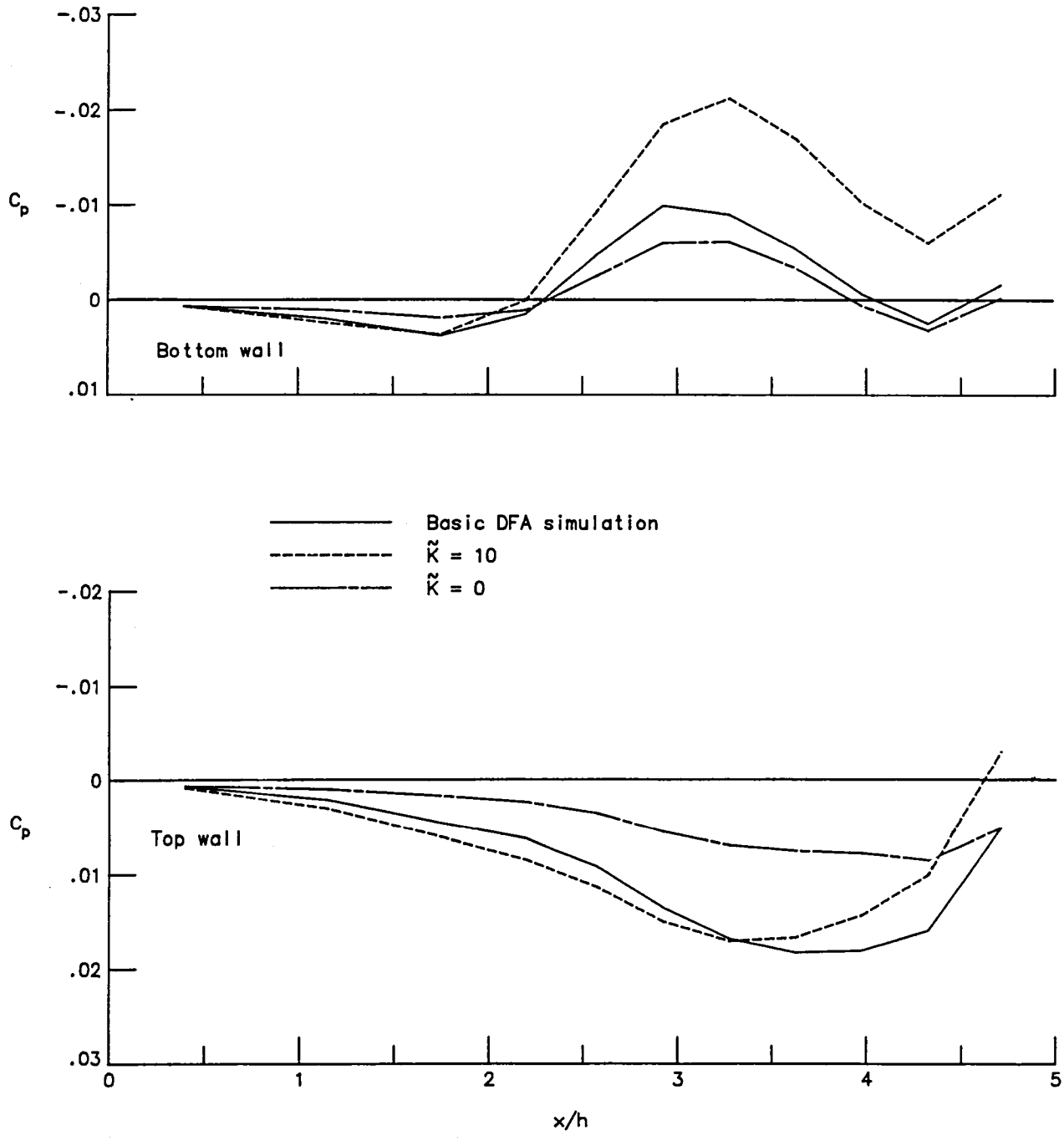

(a) Top and bottom wall pressures at y = 0.083h.

Figure 22. - Effect of slot parameter $\tilde{K}$ on simulation results for the DFA wall pressure investigation sample case.

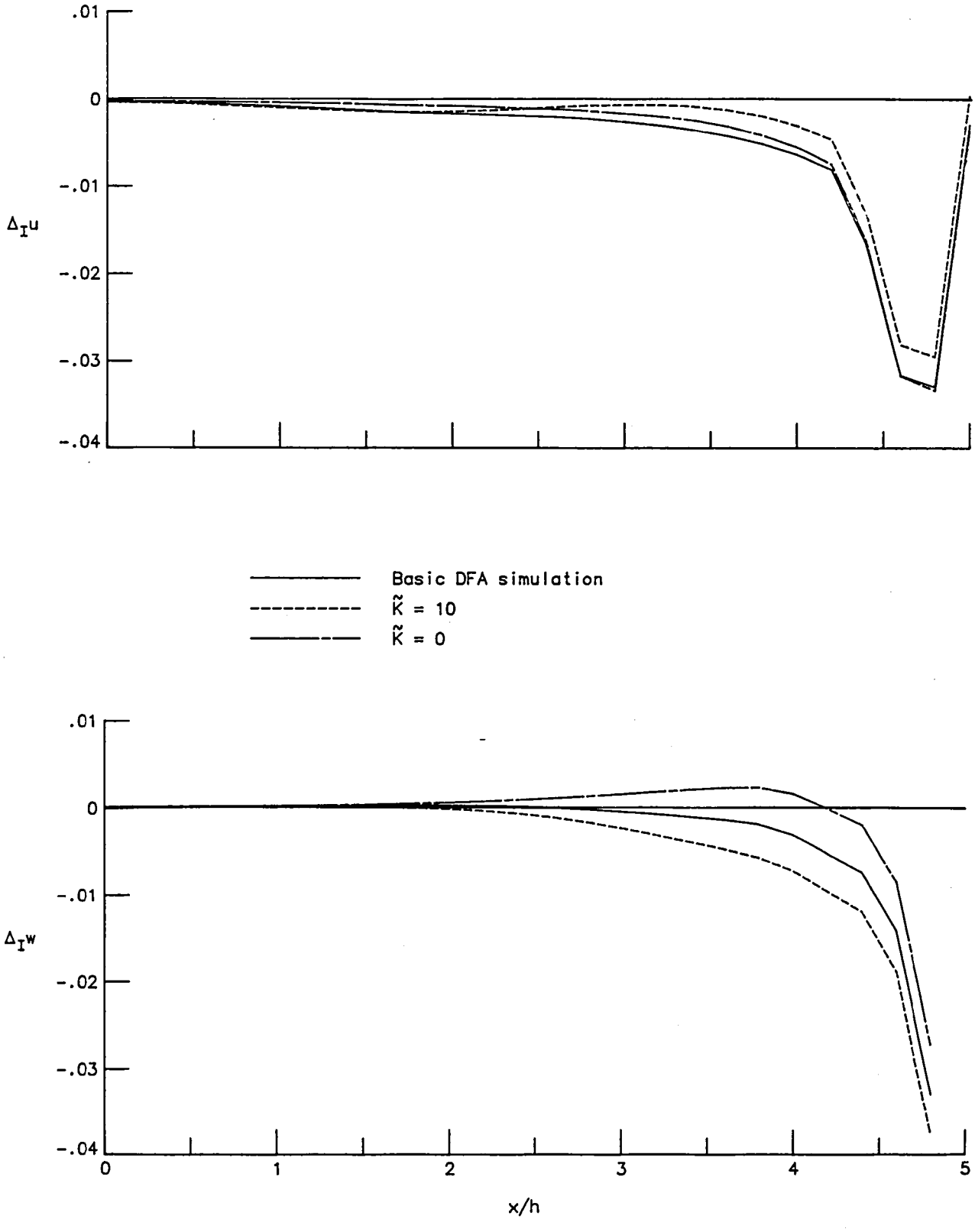

(b) Tunnel interference velocities at y = 0.2h, z = -0.084h.

Figure 22. - Concluded.

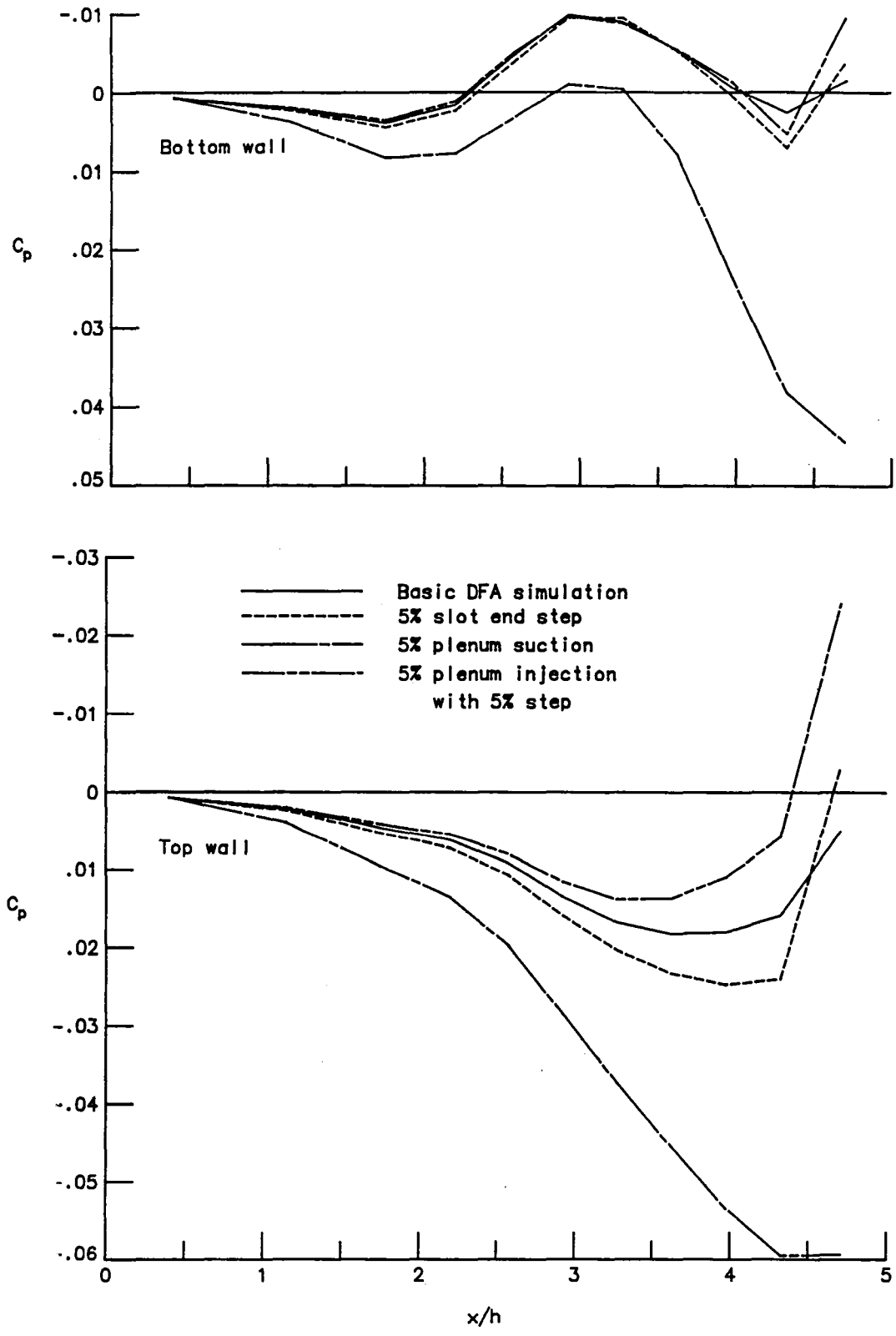

(a) Top and bottom wall pressures at y = 0.083h.

Figure 23. - Effect of plenum pumping and slot end step on simulation results for the DFA wall pressure investigation sample case.

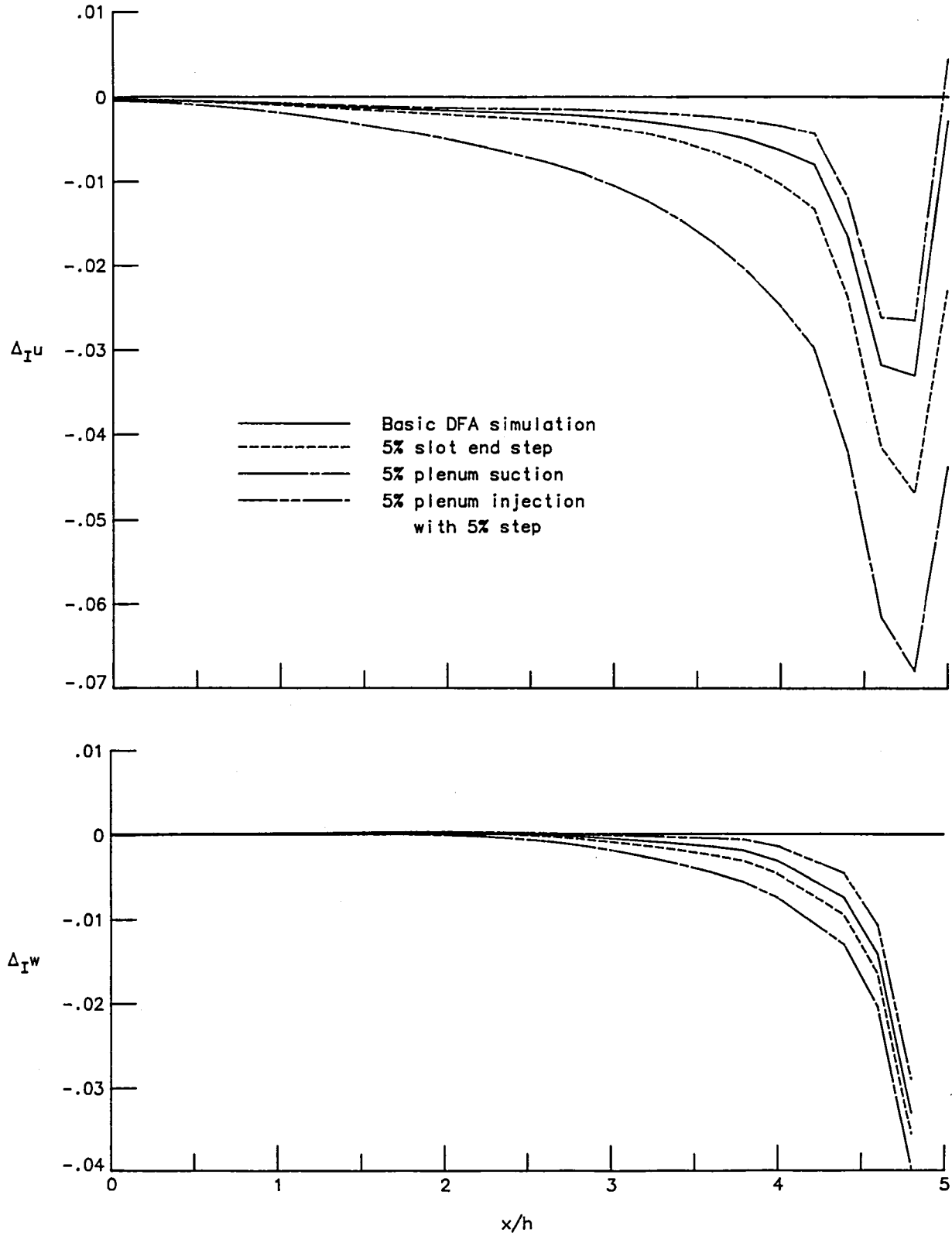

(b) Tunnel interference velocities at y = 0.2h, z = -0.084h.

Figure 23. - Concluded.

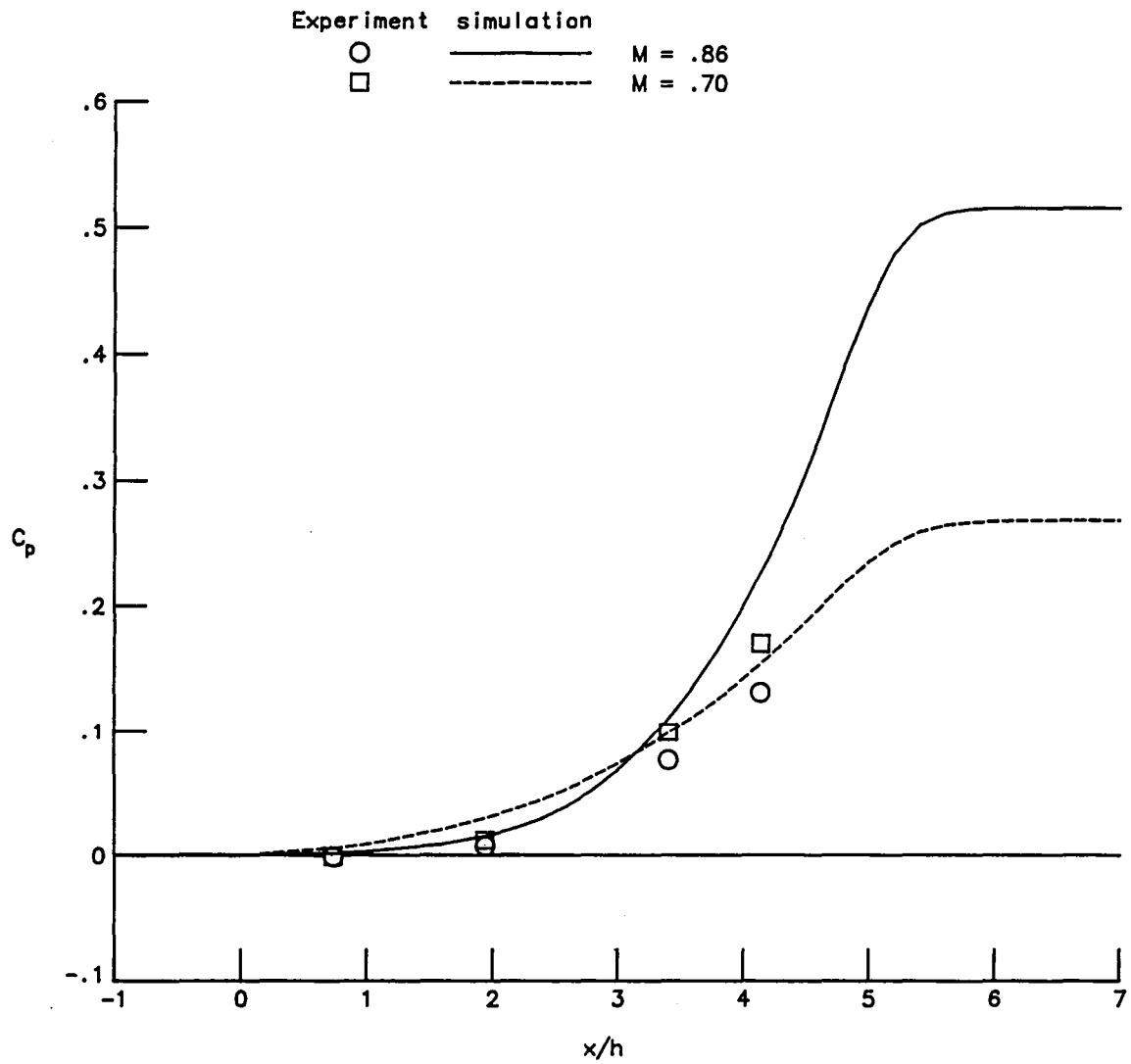

Figure 24. - Comparison of peak sidewall centerline pressures during rapid slow-down of NTF with quasi-steady simulations.

1. Report No.	2. Government Accession No.	3. Recipient's Catalog No.
NASA CR-3948		

4. Title and Subtitle	5. Report Date
COMPUTER SIMULATION OF A WIND TUNNEL TEST SECTION WITH DISCRETE FINITE-LENGTH WALL SLOTS	April 1986
	6. Performing Organization Code
7. Author(s)	8. Performing Organization Report No.
William B. Kemp, Jr.	
	10. Work Unit No.
9. Performing Organization Name and Address	11. Contract or Grant No.
The College of William and Mary Williamsburg, Virginia 23185	Cooperative Agreement NCC1-69
	13. Type of Report and Period Covered
12. Sponsoring Agency Name and Address	Contractor Report
National Aeronautics and Space Administration Washington, DC 20546	14. Sponsoring Agency Code 505-60-21-02

15. Supplementary Notes

Langley Technical Monitor: Jerry B. Adcock

16. Abstract

A computer simulation of a slotted wind tunnel test section which includes a discrete, finite-length wall slot representation with plenum chamber constraints and accounts for the nonlinear effects of the dynamic pressure of the slot outflow jet and of the low energy of slot inflow air has been developed. The simulation features were selected to be those appropriate for the intended subsequent use of the simulation in a wall interference assessment procedure using sparsely located wall pressure measurements. Simulation results demonstrate that accounting for slot discreteness is important in interpreting wall pressure measured between slots, and that accounting for nonlinear slot flow effects produces significant changes in tunnel-induced velocity distributions and, in particular, produces a longitudinal component of tunnel-induced velocity due to model lift. A characteristic mode of tunnel flow interaction with constraints imposed by the plenum chamber and diffuser entrance is apparent in simulation results and is derived analytically through a simplified analysis.

17. Key Words (Suggested by Author(s))	18. Distribution Statement
Slotted walls Wall interference Interference assessment Wind tunnel corrections	Unclassified - Unlimited Subject Category 09

19. Security Classif. (of this report)	20. Security Classif. (of this page)	21. No. of Pages	22. Price
Unclassified	Unclassified	96	A05

For sale by the National Technical Information Service, Springfield, Virginia 22161

NASA-Langley, 1986

End of Document